11-5-2018

Multivariate Analysis for the Quantification of Transdermal Volatile Organic Compounds in Humans by Proton Exchange Membrane Fuel Cell System

Ahmed Hasnain Jalal
Florida International University, ajala003@fiu.edu

FLORIDA INTERNATIONAL UNIVERSITY

Miami, Florida

MULTIVARIATE ANALYSIS FOR THE QUANTIFICATION OF TRANSDERMAL VOLATILE ORGANIC COMPOUNDS IN HUMANS BY PROTON EXCHANGE MEMBRANE FUEL CELL SYSTEM

A dissertation submitted in partial fulfillment of

the requirements for the degree of

DOCTOR OF PHILOSOPHY

in

ELECTRICAL ENGINEERING

by

Ahmed Hasnain Jalal

2018

To: Dean John L. Volakis
College of Engineering and Computing

This dissertation, written by Ahmed Hasnain Jalal, and entitled Multivariate Analysis for the Quantification of Transdermal Volatile Organic Compounds (VOCs) in Humans by Proton Exchange Membrane Fuel Cell System, having been approved in respect to style and intellectual content, is referred to you for judgment.

We have read this dissertation and recommend that it be approved.

_____
Ernesto A. Pretto, Jr.

_____
James N. Hall

_____
Kang K. Yen

_____
Nezih Pala

_____
Kingsley Lau

_____
Bilal El-Zahab

_____
Shekhar Bhansali, Major Professor

Date of Defense: November 5, 2018

The dissertation of Ahmed Hasnain Jalal is approved.

_____
Dean John L. Volakis
College of Engineering and Computing

_____
Andrés G. Gil
Vice President for Research and Economics Development
and Dean of the University Graduate School

Florida International University, 2018

DEDICATION

I dedicate this dissertation to my parents, Zainab Begum and Sheikh Muhammad Ibrahim, law-parents Shamsun Nahar and Badiul Alam, and my wife Fahmida Alam for their unconditional love and support.

ACKNOWLEDGMENT

First and foremost, I would like to express my reverential gratitude to my supervisor Dr. Shekhar Bhansali, Alcatel-Lucent Professor and Chair, Department of Electrical and Computer Engineering, Florida International University, for his extraordinary, invaluable suggestions, and continuous encouragement in the preparation of this dissertation. Without his guidance and persistent support, this research would have not been possible to complete.

My profound and heartfelt thanks to my mentor Dr. Yogeswaran Umasankar, Research Assistant Professor, Biomolecular Sciences Institute, Florida International University for his patience, meticulous care, continuous inspiration, valuable advice, and dynamic guidance all of which molded this research into a reality. I would also like to thank all my committee members, Dr. Ernesto A. Pretto, Jr., Dr. Nezih Pala, and Dr. Kingsley Lau, Dr. Bilal El-Zahab, Dr. James N. Hall, and Dr. Kang K. Yen for their interest in my research. I sincerely appreciate their invaluable time for reading the dissertation and providing comments and suggestions to improve it. I consider myself fortunate enough to collaborate with Dr. Pretto and Dr. Pala which allowed me to explore new domains of research. I am also thankful to Dr. Lau and Dr. Bilal for their valuable advice to understand my research problems and their solutions.

I am grateful to all my friends and colleagues at Bio-MEMS and Microsystems Laboratory of FIU. I would like to express appreciation to my friends Mustahsin, Randy, Kevin, Sohini, Aparajita, Khalid, Pandiaraj, Lamer, Michelle, Patrick, Apurva, and Pulak for their cordial support. I also thank all other friends and colleagues at FIU who helped me make this memorable journey. I would like to thanks to Ashfaq, Masud, Raju, Amit,

Farjana, Parvez, Atiq, Nafis, Monir, Helal, Ata, Rajib, Asif, Tarek, and many others for their cordial support during this journey. I passed a wonderful time with them all these years. I would like to acknowledge University Graduate School (UGS) of FIU for providing the “DEA Fellowship” during my tenure at FIU. I would also like to acknowledge the “Advanced Materials Engineering Research Institute (AMERI)” at FIU for the support of my research. I am thankful to ASSIST NSF ERC (Award Number: EEC-1160483), NSF Innovation Corps (Award Number: 1616196) and NSF PFI-TT (Award number: 1827682) for their support in my research.

And last but not least, I am heartily grateful to Dr. Niaz Latif and Dr. George Nnanna who always supported and motivated me during my MS for pursuing my Ph.D. And finally, I am forever indebted to my parents, my law-parents, my wife, my siblings, my uncles and aunts, and grandparents who endured this long process with me, always offering affectionate support, patience, caring assistance, and inspiration.

ABSTRACT OF THE DISSERTATION

MULTIVARIATE ANALYSIS FOR THE QUANTIFICATION OF TRANSDERMAL VOLATILE ORGANIC COMPOUNDS IN HUMANS BY PROTON EXCHANGE MEMBRANE FUEL CELL SYSTEM

by

Ahmed Hasnain Jalal

Florida International University, 2018

Miami, Florida

Professor Shekhar Bhansali, Major Professor

In this research, a proton exchange membrane fuel cell (PEMFC) sensor was investigated for specific detection of volatile organic compounds (VOCs) for point-of-care (POC) diagnosis of the physiological conditions of humans. A PEMFC is an electrochemical transducer that converts chemical energy into electrical energy. A Redox reaction takes place at its electrodes whereas the volatile biomolecules (e.g. ethanol) are oxidized at the anode and ambient oxygen is reduced at the cathode. The compounds which were the focus of this investigation were ethanol (C_2H_5OH) and isoflurane ($C_3H_2ClF_5O$), but theoretically, the sensor is not limited to only those VOCs given proper calibration.

Detection in biosensing, which needs to be carried out in a controlled system, becomes complex in a multivariate environment. Major limitations of all types of biosensors would include poor selectivity, drifting, overlapping, and degradation of signals. Specific detection of VOCs in multi-dimensional environments is also a challenge in fuel cell sensing. Humidity, temperature, and the presence of other analytes interfere

with the functionality of the fuel cell and provide false readings. Hence, accurate and precise quantification of VOC(s) and calibration are the major challenges when using PEMFC biosensor.

To resolve this problem, a statistical model was derived for the calibration of PEMFC employing multivariate analysis, such as the “Principal Component Regression (PCR)” method for the sensing of VOC(s). PCR can correlate larger data sets and provides an accurate fitting between a known and an unknown data set. PCR improves calibration for multivariate conditions as compared to the overlapping signals obtained when using linear (univariate) regression models.

Results show that this biosensor investigated has a 75% accuracy improvement over the commercial alcohol breathalyzer used in this study when detecting ethanol. When detecting isoflurane, this sensor has an average deviation in the steady-state response of ~14.29% from the gold-standard infrared spectroscopy system used in hospital operating theaters.

The significance of this research lies in its versatility in dealing with the existing challenge of the accuracy and precision of the calibration of the PEMFC sensor. Also, this research may improve the diagnosis of several diseases through the detection of concerned biomarkers.

TABLE OF CONTENTS

LIST OF TABLES

LIST OF FIGURES

FIGURE PAGE

LIST OF ACRONYMS

ADH: Aldehyde dehydrogenase

ADC: Analog-to-digital converter

ANNs: Artificial neural networksCDA: Canonic discriminant analysis

BAC: Blood alcohol content

BLE: Bluetooth low energy

COPD: Chronic obstructive pulmonary disease

CSF: Cerebrospinal fluid

CYP2E1: Cytochrome P450 2E1

CV: Cyclic voltammogram

DFA: Discrete factorial analysis

DKA: Diabetic ketoacidosis

DUI: Drinking under the influence

EDX: Energy-dispersive X-ray

EOD: Electro-osmotic drag

FK: Fasting ketosis

FID: Flame-ionization detectors

GC: Gas chromatography

HCA: Hierarchical cluster analysis

IUPAC: International Union of Pure and Applied Chemistry

ISFs: Interstitial fluids

ICA: Independent component analysis

LoD: Limits of detection

MEA: Membrane electrode assembly

MPM: Malignant pleural mesothelioma

MS: Mass spectroscopy

NK: Nutritional ketosis

OCP: Open circuit potential

PAH: Polycyclic aromatic hydrocarbon

PCF: Pericardial fluid

PCA: Principal component analysis

PCR: Principal component regression

PEMFC: Proton exchange membrane fuel cell

PID: Portable photoionization detectors

PLS: Partial least squares analysis

PLD: Pulsed laser deposition

POC: Point-of-care

PTFE: Poly-tetrafluoro-ethylene

ROS: Reactive oxygen species

SAW: Surface acoustic wave

SEM: Scanning electron microscope

SF: Synovial fluid

SVM: Support vector machine

TCO: Temperature-cycled operation

TD: Thermal desorption

VOC: Volatile Organic Compound

VSC: Volatile sulfur compound

XRD: X-ray diffraction

CHAPTER I
INTRODUCTION

1.1 Background

Detection of volatile organic compounds (VOCs) as biomarkers of different diseases and disorders allows diagnosis and therapy of several ailments in real-time, non-invasively [1]. The levels of VOCs provide an understanding of one's physiological and pathophysiological condition. These VOCs are specific to certain diseases and can be employed as olfactory biomarkers of metabolic, genetic, infectious, cancerous, and other kinds of diseases [2]. Through their easy accessibility in different clinical bio-matrices, reliable and continuous monitoring of such conditions is made possible for management of wellness in real time. Non-invasive sensing techniques promote diagnostic management as and when necessary.

Biological fluids, the source of hundreds of VOCs in the human body reflect the metabolic condition of an individual [2]. VOCs based on alkyl and chlorinated hydrocarbons, ketones, aldehydes, alcohols, aromatic compounds, furans, and esters are found in different biofluids of humans [3]. The metabolism and kinetics of these VOCs elucidate a window for therapeutic approaches to diagnose diseases noninvasively. Several physiological routes are involved in their distribution through the human body [3 4]. Many VOCs are generated by the disintegration of bio-compounds in the body [3 5]. Contrarily, many of them enter through inhalation from environmental or industrial exposures, fuels, insecticides, aerosol, air fresheners, cleansers, drugs, and food ingestion [6]. The metabolism and excretion rates of VOCs vary by disease and depend on the ambient

atmosphere as well as the physiological and pathophysiological pathways of individuals [7 8]. Classification of this variation spectrum of VOCs in any biofluid from the normal standard can be a potential diagnostic tool for diseases, drug delivery, and detection of a toxic substance in the human body. Therefore, the close monitoring of VOCs has been in demand in diverse fields such as personal healthcare or safety, therapeutic monitoring, occupational health, rehabilitation center and law enforcement agencies [9 10 11].

Various noninvasive approaches for disease diagnostics by monitoring VOCs have garnered significant attention in the past. Early in the "Age of Pericles" (460 – 370 BC) Hippocrates was the first to investigate the odor of volatilome in living organisms to diagnose diseases [12]. Many years later, Wilhelm Peters (1815 -1883) discovered acetone in breath and urine to find an "unusual apple aroma" in diabetic patients and postulated acetone as a possible biomarker for its management [12]. The first drunkometer for breath analysis and alcohol measurement to assess drunkenness in clinical application was invented in mid 1900s by Rolla Harger [13]. Later, Borkenstein discovered a breathalyzer for breath alcohol testing [14]. Until the mid-20th century, classical analytical methods involving wet chemistry, micro-diffusion and breath analysis were popular for detecting excreted VOCs. Gas chromatography-mass spectrometry (GC-MS) have been popular most among others for accurate measurement of VOCs in breath analysis [15]. Most analytical devices are not only expensive and require additional vacuum for their operation, but lack portability and continuous measurement function. Portable photoionization detectors (PID), flame-ionization detectors (FID) have been used for the detection of VOCs either as the handheld device or along with a gas chromatography-mass spectrometry (GC-MS) system [16]. Cross-selectivity is a major disadvantage with PID or FID, however, their

wide detection limits make these devices viable in many applications of sensing nonspecific VOCs.

Delayed diagnosis of several diseases and exposure of hazardous VOCs for prolonged periods of time can be fatal [11 17]. A cost effective, user-friendly, minimally invasive, continuous, and real-time sensing techniques to diagnose diseases can greatly improve healthcare and personal safety management. Wearable sensors or sensor arrays (e-noses), through precise calibration, play an alternate role in easy-to-use, fast, precise, and continuous monitoring of specific diseases. According to the International Union of Pure and Applied Chemistry (IUPAC), "biosensors are considered as devices that transform biochemical information into an analytically useful signal." [5] For timely evaluation of one's concerned health condition, the biosensors need [5]: i. accurate measurement, ii. rapid assessment, and iii. selective detection. These properties of the sensor enable a physician to accurately diagnose the specific disease and initiate required therapy to prevent further aggravation of the disease. The phenotypic characteristics of their excretion can be analyzed through the observation of their real-time VOC data [18]. Besides biosensing techniques, various analytical methods are used to accurately measure VOCs in breath. However, they are not only expensive but also lack portability and continuous assessment [19 20 21 22 23].

Biosensing techniques have prominent prospects in VOC detection on a wearable platform. There are different sensing techniques which have been employed for the detection of numerous VOCs, such as electrochemical, chemi-resistive, optical, piezoelectric, and surface acoustic wave (SAW) sensors [24 25 26 27 28]. The detail classification according to IUPAC is depicted in Figure 1-1. These sensors have been

miniaturized by advancements in micromachining and nanotechnology [29]. Incorporation of nanomaterials are known to influence their sensing performance and assists in a multi-sensing arrays platform [29 30]. The use and combination of different kinds of nanomaterial is therefore gaining interest in the design of clinical and diagnostic tools, due to their advantages of higher surface-to-volume ratios. Their specific forms provide faster response and recovery times, in addition to support specific detection through suitable alterations of their physical and chemical properties. Assisting in very-large-scale integration manufacturing and miniaturization to enable portability, they allow integration in point-of-care (POC) devices [31].

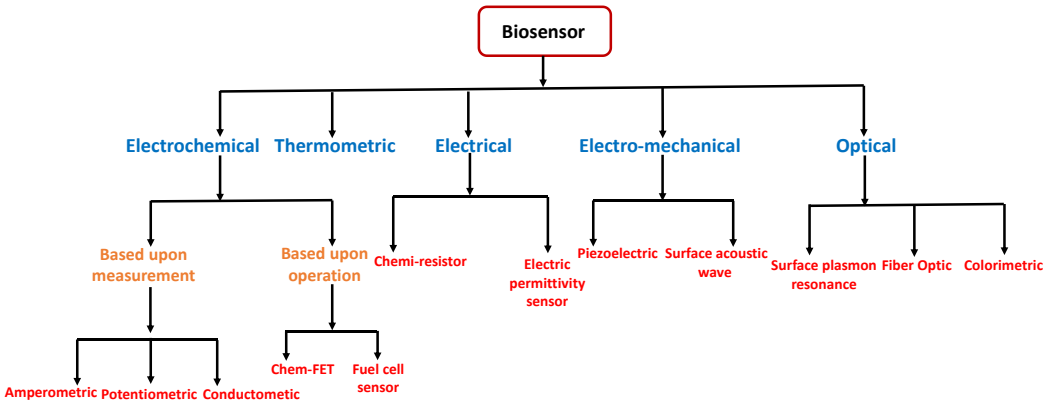

Figure 1-1: Classification of biosensors

Current VOC sensors in the market use mostly four measurement techniques [24 25 26 27 28]: optical, electrochemical, chemi-resistive sensors and SAW sensors. Most of these sensors suffer from instability, non-linearity, cross-selectivity, inaccuracy at low concentrations, and some of them are not portable [5]. Electrochemical alcohol sensors have typically been found to be most suitable for long term sensing. Among them, fuel

cell sensors offer simplicity, relatively high accuracy, sensitivity, long working lifetime, scalability and portability, hence they find use in breathalyzers.

The challenge of selective detection is yet to be overcome in existing VOC sensing approaches. This is due to the complex composition of the sampling matrices. Different intrinsic (e.g. hysteresis, fouling effect) and extrinsic ambient parameters (e.g. humidity, temperature) can also interfere with precise detection in a multivariate environment, coupled with signal degradation over time [32 33 34]. Detection using multiple sensors on the same platform improves the response through elimination of mentioned interfering variables [34]. More detailed information on one's physiological condition can be obtained through integration of e-noses on a multimodal sensing (e.g. skin temperature, gyroscope, etc.) platform [35]. Such sensing modalities provide a better understanding of one's physiological condition enabling accurate detection in real-time [36].

The use of sensor arrays (e-noses) and techniques entailing different pattern recognition (unsupervised) and classification (supervised) approaches target specific VOC detection from a multivariate environment [37]. Different pattern recognition and machine learning approaches, such as principal component analysis (PCA), discrete factorial analysis (DFA), and partial least squares analysis (PLS), assist in reducing the redundancy of acquired data, aiming toward improved selectivity, specificity, and stability [38 39]. Once data are collected by multi-sensor arrays or e-noses, it goes through transformation, a filtering process, and is fed to a genetic algorithm for searching. Further, a pre-defined prediction model and regression method promote precise calibration in a multivariate environment [40 41]. Such methods provide a pattern in diagnosis, through cross-validation in different population sectors.

In summary, this research focuses on providing a pragmatic solution for improving the calibration of the biosensor (e.g. PEMFC sensor), in a multivariate environment, using a multivariate analysis method.

1.2 Problem statement

Like other biosensors, fuel cell sensors are incapable of specific detection of a single VOC in a multi-dimensional environment. This is mainly due to the proton exchange membranes' dependency on humidity and temperature which interfere with its functionality. Furthermore, the presence of other analytes can well interfere providing false readings, hindering calibration of the system in precise quantification of any volatile compound. A minimal drift or overlap of the signals, even in the nano-Ampere range, can cause substantial interference and provide false readings in the physiological range of any VOC(s). Employing multivariate analysis method, such as PCA; this research improves the calibration through reducing the redundancy and drifting and eliminates overlaps of the signals of the fuel cell sensor. However, the limitation of this classification approach is that it can only predict the unknown concentration based upon test data. During calibration, it is impractical to figure out the test data for each concentration within its physiological range.

Therefore, principal component regression (PCR) method has been employed in this work, which estimates the specific current for any concentration of VOC. This method can correlate larger data sets and provides an accurate fitting between a known and an unknown data set. If the number of variables is closer to or larger than the sample size, the accuracy of estimation is impacted. PCR establishes a relationship between the response

variables (the concentration of VOC) and the predictor variables (current signals) to estimate the response variables. It is a three-step calibration process: i. redundancy is eliminated through PCA, ii. the measured variable is converted into latent variables, and iii. multiple linear regression steps are executed between the scores of the covariates obtained in PCA. Furthermore, this model has been employed for the determination of unknown concentrations of specific VOCs from human subjects and has been validated by a theoretical model and gold-standard commercial devices. The significance of this approach lies in its versatility dealing with the existing challenge of calibration of sub-ppm level measurement of VOCs (e.g. ethanol and isoflurane) by PEMFC sensor.

1.3 Research goal and objectives

The goal of this research is to provide a complete framework to identify an unknown concentration of VOC from human subjects with accuracy and precision. Considering the above-mentioned issues, the specific objectives are:

1. To determine the suitable model for accurate determination of VOC in ppm/ppb level for PEMFC sensor;
2. To quantify the unknown concentrations by fitting the predictor variables (current signals) in the developed model;
3. To explore the scope of this model for the measurement of VOC(s) from human subjects in real time, continuously; and
4. To validate the results of the PEMFC sensor by comparing with the commercial/gold standard devices.

1.4 Dissertation organization

This dissertation is comprised of six chapters. Figure 1-2 summarizes the contents of the next five chapters followed by this chapter (Chapter I: Introduction).

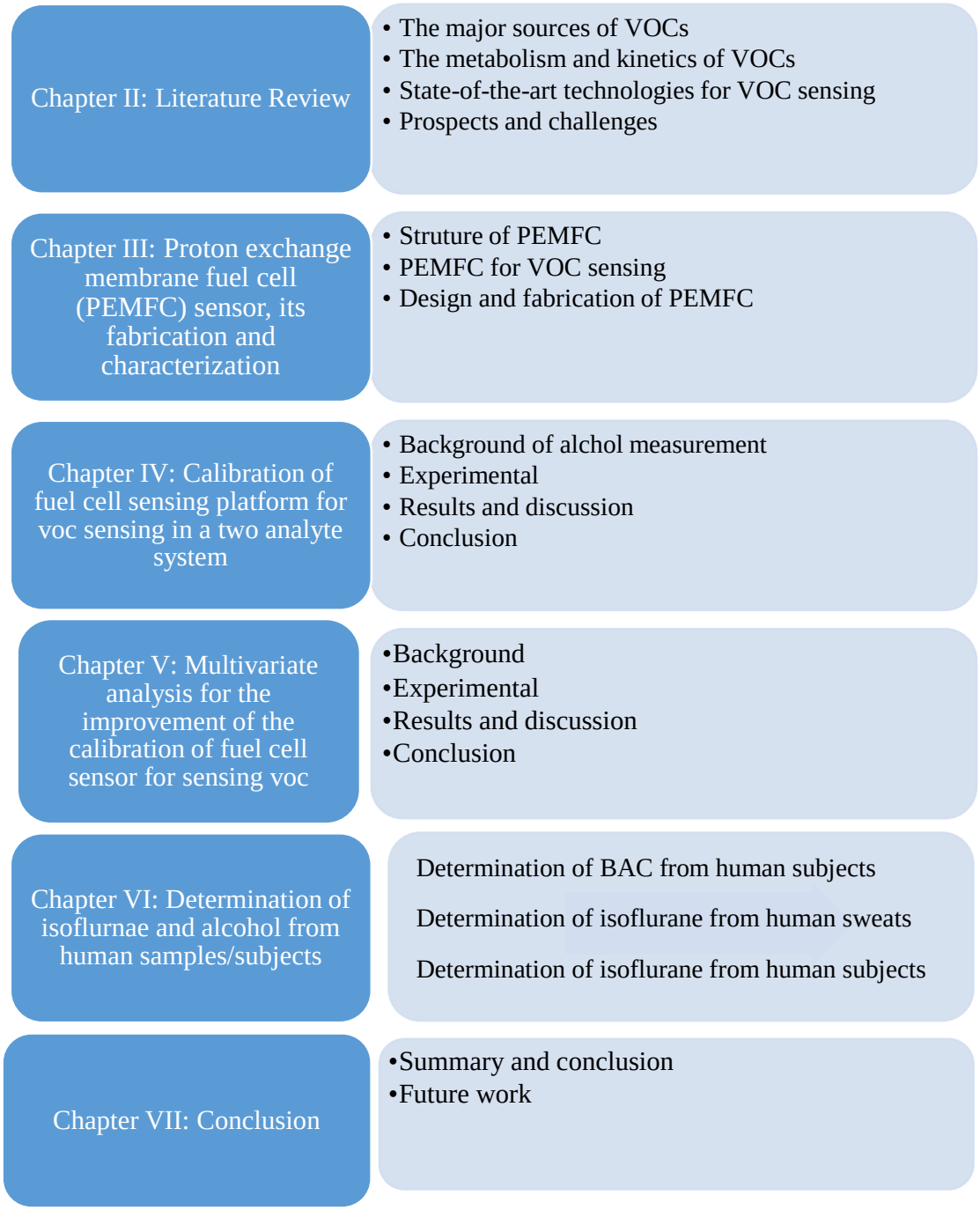

Figure 1-2: Dissertation Organization

CHAPTER II
LITERATURE REVIEW

This chapter provides a comprehensive literature review on the following topics: (a) different sources of VOCs; (b) Kinetics and metabolism of VOCs in the human body; (c) different sensing techniques of VOCs in humans; and (d) prospects and challenges of sensing VOCs in humans. Section 2.1 discusses the sources of VOCs. Section 2.2 focuses on the metabolism and kinetics of VOCs in humans. Section 2.3 delineates different sensing techniques. Finally, the challenges of VOC sensing in humans in real-time and their possible solutions have been presented in Section 2.4.

2.1 Biofluids as the source of VOCs

Recent research suggests that 1,849 VOCs have been found in different biofluids [42]. Such biofluids include blood, interstitial fluids, breath, sweat, saliva, urine, serum, breast- milk, tear, and feces (Figure 2-1a). Figure 2-1b shows that breath and skin are the

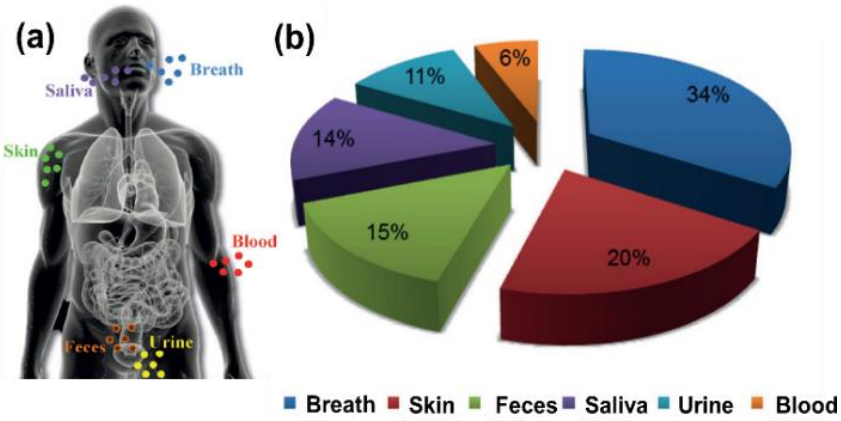

Figure 2-1: a. Different biofluids of VOCs in the human body [43], b. VOC percentages in different biofluids following the data of a healthy human. [43]

potential sources of VOCs (54% of total amount), with 15%, 14%, 11%, and 6% of them being present in feces, saliva, urine, and blood, respectively [43]. These sources are feasible for either invasive or noninvasive detection of VOCs for diagnosis of diseases.

2.1.1 Sources for invasive detection

2.1.1.1 Blood and plasma

Blood has been considered as a reliable matrix to characterize the physiological condition of an individual. There are 154 different VOCs that have been discovered in blood [3]. These VOCs are the biomarkers of many diseases and reflect the internal status of the human body pertaining to nutritional, metabolic, and immune conditions [43]. Blood contains different volatile compounds: typically, acetonitrile, ammonia, ethers, alkanes, alcohols, benzyl, and phenyl hydrocarbons [3]. The metabolic and immune status of humans can be determined by analyzing VOCs from the blood. For example, benzene and toluene levels in blood increase due to smoking, while tri-halo-methane levels in blood are high in swimmers with elevated levels of chloroform [44 45]. Levels above the normal for any of these exogenous compounds can be detrimental to human health. High doses of chloroform could lead to liver toxicity, providing a pathway for other fatal diseases with reduced red blood cells, causing anemia and DNA breakage. Horvath et al. suggests specific aroma(s) in blood is a suitable tool for screening different kinds of cancer or internal disorders, like ovarian carcinoma, lung cancer, hepatic encephalopathy, etc. [46]. Plasma derived endogenous VOCs in blood have attracted researchers for early cancer detection (e.g. gynecological, lung, etc.). Selyanchyn et al. introduced an analytical method to assess VOCs in blood for cancer detection [47]. In their work, VOCs of blood plasma

have differentiated between carcinogenic and benign controls precisely. Although blood tests are more consistent than detection from other biofluids, obtaining blood samples is arduous, inefficient, invasive and inapplicable for instantaneous POC applications.

2.1.1.2 Interstitial fluids (ISFs)

Different ISFs such as cerebrospinal fluid (CSF), peritoneal fluid, pleural fluid, biliary fluid, synovial fluid (SF), or pericardial fluid (PCF) are also analyzed to diagnose different diseases. The presence and analyses of VOCs in such biofluids are limited in the literature. Liu et al. explored 76 different pleural samples and found three major groups: ketones, alcohols and benzene derivatives dominating for cancer malignancy. Among 76 VOCs, nine of them including dichloromethane, ethyl acetate, n-heptane, ethyl-benzene, xylene, cyclo-hexanol, cyclo-hexanone, 2-ethyl-1-hexanol, and tetra-methyl benzene are potential compounds for screening lung cancer to differentiate malignant from benign pleural effusions. Conditions such as tuberculosis, pneumonia, congestive heart failure and cirrhosis are the cause of benign effusions, where 30% of malignant effusion is associated with lung cancer [48]. VOC analysis of biliary fluid can also distinguish malignant cholangiocarcinoma from benign biliary strictures. It can be used as a potential biomarker for pancreas cancer by classifying the concentration spectrums of tetra-methyl acetate, acetone, acetaldehyde, benzene, carbon disulfide, and pentane [49]. The presence of inflammation and oxidative stress modulate the release of VOCs from SF which cause osteoarthritis and rheumatoid arthritis. Tominaga et al. sightseen toxicological analysis for serial forensic autopsy cases and compared PCF with peripheral blood to reassess the postmortem distribution of ethanol and to examine the dispersal of other VOCs [50].

However, the invasive nature of the detection mechanism from ISFs is always laborious, expensive and inefficient for real-time detection.

2.1.2 Sources for noninvasive detection

2.1.2.1 Urinary biofluid

Urine tests are an established method to detect several diseases noninvasively. The aqueous urinary matrix contains a small percentage of VOCs [51]. Renal activities control the supply of endogenous and exogenous VOCs in urine. Endogenous VOCs comprise ketones, alcohols, heterocyclic compounds, different hydrocarbons, amines, aldehydes and organic acids [51]. Ketones are the most common VOCs that can be produced through breakdown of fatty acid due to oxidation. Ketone levels can rise from normal due to starvation (fasting ketosis, FK), consumption of low carb-high fat diet (nutritional ketosis, NK) and alcohol; and prolong exercise. The raising state of NK provides energy to the brain of epileptic patients [52]. The elevated level of ketones in urine is also a biomarker of hyperglycemia or diabetic ketoacidosis (DKA). Inadequate ketogenesis causes hypoglycemia whereas excessive presence of ketones leads to ketoacidosis. However, DKA is a severe case with increasing to more than twice of ketone levels, as compared to other states of ketosis [11]. As ketone levels depend on multiple physiological parameters (e.g. energy stability, diet composition, physical activities and diseases), accurate diagnosis of one's ketone profile is critical to identify an actual physiological condition [52]. Like ketones, other VOCs in urine are also possible biomarkers of many diseases and can provide a certain profile for the VOC depending on dehydration, diet, liquid and drug intake. Elevated levels of acetonitrile in urine confirms whether someone is a smoker or

not [53]. Urinary metabolomics studies have been employed to different cancer studies, such as breast, colorectal, esophageal cancer, pancreatic ductal adenocarcinoma, prostate and liver cancers [54]. Analyzing four different VOCs (2, 6-dimethyl-7-octen-2-ol, pentanal, 3-octanone, and 2-octanone), Khalid et al. demonstrated the detection of prostate cancer [55]. Matsumura et al. demonstrated ex-vivo analysis of urinary VOCs as biomarkers for lung cancer [56]. Arasaradnam et al. differentiated coeliac disease from irritable bowel syndrome (IBS) and Banday et al. demonstrated a tuberculosis diagnosis by using GC-MS [57 58]. Testing of urine in a noninvasive form of detection is reliable though sample collections, handling, and preservation. Also, urinary analysis is cumbersome complication. Hence, diagnosis of VOC biomarkers is technically complex from the urinary sample, and this biofluid is not suitable for continuous monitoring.

2.1.2.2 Saliva

Saliva is known to contain 360 different kinds of exogenous and endogenous VOCs [43]. Like breath, different food debris, drugs, xenobiotics and environmental pollutants can affect various exogenous compounds in detecting VOCs from saliva. Active and passive diffusion of VOCs from blood and ultrafiltration techniques are among the most common approaches used for VOC detection in saliva [59]. 300 different bacterial species have been explored as sources of VOCs in saliva. Major VOCs in saliva include acetic acid, ester, acetonitrile, mercaptan, methyl sulfide, different alkanes, diene, different aromatic compounds (e.g. benzene, toluene, xylene), polycyclic hydrocarbons (carane, copaene, etc.), alcohols (ethanol, propanol, butanol, etc.), and aldehydes (acetaldehyde, propanal, etc.) [3 42]. Recent research suggests salivary fluid can be a potential biofluid

for noninvasive, continuous, and instantaneous monitoring of different diseases. Several research groups investigated the integration of electrochemical sensors into mouth-guards for monitoring biomarkers [60]. In contrast with other biofluids, the salivary biofluid provides a significant amount of fluid for a greater functioning space for the placement of the sensing unit. With an abundance of VOCs in saliva, this is one of the promising biofluids for continuous and real-time monitoring of different diseases [60].

2.1.2.3 Skin perspiration and sweat

Human skin is the largest organ in human body and it offers long-lasting emanation of VOCs. Costello et al. mentioned 532 different VOCs are derived from skin secretion through diffusion of sweat [3]. Main VOCs from the skin of a healthy individual include ammonia, carboxylic acid, alcohols, hydrocarbons, ketenes, terrenes, aldehydes, esters, heterocyclic compounds, and volatile sulfur compounds [61]. The profiles of these VOCs differ due to heterogeneous distribution of sweat glands beneath the skin and the metabolism of symbiotic microbiota on the skin surface. The existing clusters of bacteria on the skin contribute to the odor of individuals [62]. Internal excretion of VOCs through skin, however, depends on secretion from its three major glands: i. apocrine gland, ii. eccrine gland and iii. sebaceous gland. Osmosis plays a major role in the transmission of VOCs through these glands and secretion through sweat. Secretion of VOCs can fluctuate with time and change with physiological conditions. This emission pattern, as discussed, can vary with diet, xenobiotics, drugs, psychological stress, wounds, dehydration, shock, body temperature, age, menstrual cycle and ambient parameters (e.g. temperature, relative humidity, and pressure) [63]. Boman et al. verified VOC transmission through skin with

diffusion studies on different VOCs using Franz cell diffusion method [64]. Aside from endogenous VOCs, different xenobiotics can be emitted through skin after their metabolism in the body. For example, 1% of the overall consumption of alcohol is excreted in a diffusive manner from the exocrine sweat gland of the skin following a specific partition ratio (Henry's law) [5]. Human sweat and skin perspiration are potential sources for noninvasive medical diagnostics with their simpler sample collection process. These also offer unique facilities of safety and continuous and real-time monitoring.

2.1.2.4 Breath

In 1971, Linus Pauling confirmed that human breath is a complex volatile mixture of more than 250 different VOCs. Considering endogenous and exogenous VOCs, 874 types of VOCs have been found in exhaled breath [42]. Major VOCs of human breath in healthy individuals include acetone (1.2–900 ppb), ethanol (13–1,000 ppb), methanol (160– 2,000 ppb), isoprene (12–580 ppb), ammonia, and minor components include pentane and higher chains of alcohols, aldehydes, and ketones [65]. Internal conditions, environmental exposure, diet, and lifestyle (e.g. alcohol consumption) of individuals influence the concentration ratio of VOCs in their breath, called "exposomes". Thus, the aroma of "exposomes" can vary from person to person. For example, smoking cigarettes leads to high concentrations of acetonitrile and furans. Likewise, elevated levels of isoprene are considered an indication of exertion, and enhance alveolar ventilation and cause the isoprene level to rise 3-4 fold [22]. Similarly, an acetonic smell might be associated with hysterical diabetes; or a pungent odor might indicate liver disease [66 67]. Similarly, elevated levels of ethane and pentane are symptoms of different chronic lung

diseases, such as malignant pleural mesothelioma (MPM), cystic fibrosis, asthma, or chronic obstructive pulmonary disease (COPD) [68]. Mazzatenta et al. described that the average amount of VOCs decreases in an Alzheimer patient. Comparing with healthy controls, it appeared the disease altered the brain metabolism due to the death of neurons and their pathological state [69]. Detection of specific VOC from breath is a challenge, as there is always a possibility to obtain false readings with the presence of exogenous compounds.

2.1.2.5 Other sources

Feces, tears and breast milk are other common sources of VOCs. Fecal samples currently constitute about 480 VOCs [43]. In feces, diverse exogenous elements are present due to the consumption of medication and nutrients, which generate extrinsic volatile and nonvolatile metabolites. Bacterial fermentation and microbiota are responsible for the specific odor of feces, which results from colonic fermentation of amino acids. Along with these, some putrefactive chemical compounds are also present, such as aliphatic amines, ammonia, branched-chain fatty acids, short chain fatty acids, derivatives of phenol or indole, and volatile sulfur containing compounds [43]. Different aldehydes, such as acetaldehyde, have been produced from the dietary and microbial metabolism, which have found relevance with colon and pancreas cancer [70]. Fecal VOCs, like those arising from vibrio cholera, can be potential biomarkers of different gastrointestinal diseases. Similarly, Gulber et al. recently mentioned the existence and detection mechanism of pheromone (a cocktail of VOCs) in the ocular matrix as a biomarker of emotion and mood [71]. Pellazari et al. studied the detection of VOC from maternal milk to reveal that 156 “purgeable”

compounds can be studied form it as pollutants that would affect a nursing infant [72]. GC-MS studies on its analyses have shown that among the different VOCs present in human milk, 45 are odor-active constituents, comprising groups of monocyclic aromatic amines [73], phthalate esters [74], and benzene and alkyl-benzenes [75].

2.2 Metabolism and kinetics of VOCs

The mechanism of metabolism and kinetics of VOCs in the human body is an intricate process. The profiles of different VOCs vary based on several internal and external factors. The advancement of analytical tools allows for the total number and classification of VOCs in different biofluids to be better identified in the present days [42]. These VOCs are classified into two groups: endogenous and exogenous. The generation of exogenous VOC production follows five steps [76]: liberation, absorption, distribution, metabolism, and excretion. Contrarily, metabolism and excretion are the key mechanisms for the generation of endogenous VOCs. In both the cases, however, metabolism is a vital step in production through synthesis (anabolism) or breaking down of compounds (catabolism).

2.2.1 Metabolism of VOCs

The Endogenous VOCs are produced due to regular and abnormal metabolic processes occurring in the body. The most common reason for VOC generation is the destruction of cells from direct or indirect oxidative stress and inflammation of the human body [43]. Molecular oxygen is required to protect the cellular metabolism; therefore, equilibrium of oxygen is maintained within the human body through homeostasis. As a process of energy generation in mitochondria, 1% to 5% of oxygen molecules are reduced

to water molecules by the cytochrome through catalyzed electron transport chain reactions. This inter-cell energy conversion process relies on any of the following four processes [77]: i. reactive oxygen species (ROS), ii. hydrogen peroxide formation, iii. generation of hydroxyl radical; and iv. superoxide formation. Among them, ROS has been identified as the chief contributors to many neurological, inflammatory, cardiovascular, and immunological diseases, along with progression of aging [78]. The formation and disintegration of ROS in mitochondria trends towards equilibrium, and many hydrocarbons have been bound to the oxygen species in the process of mitochondria to cytoplasm conversion. Molecular structures of the cell with proteins, DNA, RNA, and poly-saturated fatty acids get affected and disintegrate due to the presence of accumulated ROS [79]. Different hydrocarbons have been generated during this process, and they may further oxidize and produce different kinds of alcohols, aldehydes, and ketones. Different microbials and enzymes are involved in the further metabolic processes, which therefore generates many different VOCs. For example, alcohol is metabolized by alcohol dehydrogenase due to three different kinds of enzymes: aldehyde dehydrogenase (ADH), cytochrome P450 2E1 (CYP2E1) and catalase [80]; these convert the ethanol into acetaldehyde and later into nontoxic acetic acid. Likewise, ADH enzymes enhance metabolic activity and produce carboxylic acids through the disintegration of aldehydes. Different VOCs are also generated from dead cells in the human body. 1, 3-di-tert-butylbenzene, 2, 6-di-tertbutyl-1, 4-benzoquinone, and n-decane were found in dead lung cancer cells due to apoptosis and necrosis [4].

Exogenous VOCs are mainly absorbed from food and drink, which reach to the gastro-intestinal tract, metabolized mostly in the liver and kidneys. The liver is the key

organ that is actively involved in both catabolism and anabolism of many exogenous VOCs, creating a route to stream blood from the intestine. Thus, VOCs in fecal samples in the gastro-intestinal tract go through a probable transformation in the liver before being distributed to the blood, reaching the lungs and appearing in breath. As mentioned earlier, the liver is the bed for large varieties of enzymes, where ADH is actively involved in the oxidation of non-polar VOCs, converting them into conjugate compounds [80]. Likewise, it contains a large quantity of CYP2E1; and is a mixed function oxidase system, actively involved with the transformation of xenobiotics. Nonpolar hydrocarbons are transformed into polar alcohols/aldehydes, which convert to acids via the process.

2.2.2 Kinetics of VOCs

After metabolized in liver, VOCs are distributed through blood. The change in VOC over time in the liver is described by the mass balance equations as follows [81]:

$$V_{liver}\frac{dC_{liver}}{dt} = Q(C_{LBM}\text{-}\ C_{liver}) + (k_s V_{stomach} C_{stomach}) - \frac{V_{max} C_{liver}}{k_m + C_{liver}} \quad (1)$$

$$V_{LBM}\frac{dC_{LBM}}{dt} = -Q(C_{LBM}\text{-}\ C_{liver}) \quad (2)$$

where, $k_s V_{stomach} C_{stomach}$ refers to the stomach emptying rate in mole/minute. The amount of liquid compound moving out of the liver and into the lean body mass (LBM) is governed by the difference respective to the compound's concentrations (C_{LBM} and C_{liver}) at a rate controlled by the blood flow rate, Q. According to Michaelis-Menten kinetics, the present concentration limited by V_{max}, follows enzymatic reactions represented by the end segment in equation 1 [82]. Equation 2 describes the change in its concentration in the LBM based on the concentration of that in the liver at a rate governed

by the blood flow rate, Q. Apart from the liver, the kidneys and lungs play a significant role to metabolize many VOCs. The mass balance equations (equation 1 and 2) can be similarly applicable for both the kidneys and lungs, considering their own parameters [81 82]. The compound in the blood stream diffuses through the epidermis and stratum corneum. Blood boundary concentrations are driven by the body VOC concentration from the kinetic phenomenon that sets a concentration gradient through the epidermis and stratum. The total partial pressure is [83]:

$$\frac{dP_t}{dt} = D_e \frac{\delta^2 P_e}{dx^2} + D_s \frac{\delta^2 P_s}{dx^2} \quad (3)$$

where, $0 \leq x < L_e$ and $L_e \leq x < L_e + L_s$. For equations 3, D_e and D_s are the molecular diffusivity, L_e and L_s are the thickness of the epidermis and stratum conium, respectively.

The exogenous VOCs can also reach inside the human body through inhalation; and limited amounts of them are absorbed through the skin. Inhalation of VOCs occurs through regular absorption process mostly in the alveoli of lungs. The VOC molecules diffuse through the thin capillaries and alveolar type I cells in both directions and reach equilibrium thermodynamically [84]. The partition coefficient of blood and air ($\lambda_{b:a}$) governs this phenomenon, and it is one of the major determinants of the pulmonary uptake of VOCs. Rapid blood flow in the lungs creates a higher concentration gradient of uptake VOCs, which results in rapid diffusion into blood. As per classical gas exchange theory, the alveolar partial pressure of VOC, normalized to the mixed venous partial pressure, is interrelated to the blood-air partition ratio ($\lambda_{b:a}$) and the ventilation to perfusion ratio (V_A/Q) as follows [85 86]:

$$\frac{P_a}{P_V} = \frac{\lambda_{b:a}}{\lambda_{b:a} + V_A/Q} \quad (4)$$

Farhi's equation represents alveolar concentration (C_a) that is derived as follows from equation 4 [87]:

$$\frac{C_a}{C_V} = \frac{1}{\lambda_{b:a} + V_A/Q} \quad (5)$$

Here, C_V is the mixed venous concentration. Respiratory rate and the fraction of the molecules that exist at the alveolar tract are also the major factors of this transmission. The higher value of the coefficient ensures greater VOC uptake during inhalation, even in an order of 12 fold of magnitude [43]. The partition coefficient varies with respect to polarity and solubility of VOCs in the blood with the range of $10 < \lambda_{b:a} < 100$. Here, the partition coefficient is $\lambda_{b:a} < 10$ for non-polar VOCs, and the highly blood-soluble polar VOCs have the partition coefficient as $\lambda_{b:a} \geq 100$. The partition ratio of fat to blood, $\lambda_{f:b}$ is also vital in kinetics of VOCs. These two physiochemical partition coefficients govern the balance concentration of VOCs in breath, blood and fat. Poulin and Krishnan projected the value of $\lambda_{b:a}$ and $\lambda_{f:b}$ from the known partition ratios of water-air $\lambda_{w:a}$, and octanol-water ($\lambda_{o:w}$) as follows [79]:

$$\lambda_{b:a} = \lambda_{o:w} . \lambda_{w:a} . (a + 0.3b) + \lambda_{w:a} (c + 0.7b) \quad (6)$$

$$\lambda_{f:a} = \lambda_{o:w} . \lambda_{w:a} . (A + 0.3B) + \lambda_{w:a} (C + 0.7B) \quad (7)$$

where, a ≈ 0.0033 represents a portion of neutral lipids in blood, b ≈ 0.0024 represent phospholipids in blood; c ≈ 0.82 is water in blood; A ≈ 0.798 is neutral lipids in adipose tissue (fat), B ≈ 0.002 is phospholipids in adipose tissue, and C ≈ 0.15 denotes water in adipose tissue. As discussed earlier, these absorbed compounds are distributed to other organs.

2.3 Different sensing techniques for the detection of VOCs

Different analytical methods, such as GC-MS, are acclaimed for their precise and specific detection [88]. However, performance on a miniaturization scale has yet to be achieved. Such form factors for optical, chemi-resistive, and electrochemical approaches have been achieved through advances in nanotechnology involving micro/nano scale fabrication [24 25 27]. The advancement of the synthesis process cantailor the shape, size, and assembly of different nanomaterials with extensive variation of compositions and crystal structures, such as nanoparticles, nano-rod, nanotubes, nano-spheres, nanoflakes, nanosheets, hollow spheres, hierarchical nano-architectures, octahedral, etc. [31 89]. The large electroactive surface-area-to-volume-ratio of these crystals enhances the sensitivity, and their well-defined crystal lattice leads to control catalytic reactions for stability of the sensors [31]. The open pores and large voids of various nanostructures enhance response and recovery time of gas sensing [18]. These crystals are typically formed by different carbon allotropes (e.g. graphene, carbon nanotubes) and noble metals (e.g. Au, Ag, etc.) or metal oxides (e.g. SnO_2, ZnO, TiO_2, WO_3, In_2O_3, etc.) [38 90]. Among them, ZnO and SnO_2 were widely explored for biosensing for their high quantum yields, high refractive index, wide bandgap (~ 3.37 eV), and high binding [91 92]. The conductivity of these types of sensors can be altered through the variation of different parameters (e.g. radius, inter-particle distance, di-electric constant of inter-particle medium) of nanoparticles [93]. Their sensing performance can be further improved through tailoring their surface area in a metal-organic-framework (MOF) [94]. Different potential VOC sensors for real-time detection, their sensing mechanism, limitations and prospects are discussed in the following section.

2.3.1 Optical sensors

Optical sensing is a potential sensing method for the detection of VOCs in healthcare and wellness management. This detection approach is preferred over other conventional analytical techniques, different spectroscopic techniques (e.g. Surface-enhanced Raman spectroscopy) and commercially available VOC detectors (e.g. PID, FID), as it provides comparatively better selectivity, reversibility, fast multiplexing features with elimination of electromagnetic interference, and portability [95]. The detection mechanism of optical sensors relies on the following properties of the electromagnetic waves: wavelength, phase, amplitude, intensity, and state of the polarization [96]. Recent advancements in optical sensing tools have concentrated on surface plasmon resonance (SPR), Bragg's fiber, colorimetric, Fabry–Perot cavity (FPC), and fiber optic-based sensors [97]. Plasmonic sensors have the potential for VOC sensing, owing to their high sensitivity [98]. They were achieved by enabling the identification of extremely small wavelength shifts in an order of 10^{-3} nm via noble-metal nanoparticles extinction spectra (absorption and scattering). This minute shifting has been controlled through the alteration of size, shape and assembly of the nanoparticles and the ambient refractive index (RI) [99]. The working mechanism of SPR affinity VOC sensors depends on the change of RI, formed by the capture of VOC molecules following the concentration gradient at the thin-film surface and their interaction [100]. The sensor response is proportionate to the alteration of binding-induced refractive index (n), where the binding occurs within this thin film at the sensor surface of thickness (t). The relationship can be expressed as [101],

$$\Delta n = \frac{dn}{dc}\,\frac{\Gamma}{t} \qquad (8)$$

where, (dn)/dc is the increment of RI with the concentration of analyte molecules and Γ denotes the surface concentration in mass/area.

Cheng et al. demonstrated the reversible and highly sensitive localized surface plasmon resonance (LSPR)-based sensor for the detection of toluene, n-octane, chlorobenzene, pentanol, and m-xylene. In their work, Ag-nanoparticles and Au-nanoshells enhanced the surface area, which promoted significant adsorption of VOCs [102]. Chen et al. modified the thin film surface made of Ag-nanoparticles with the thiolate self-assemble monolayer, which enhanced the VOC-selectivity and reversibility [103]. Iitani et al. demonstrated fluorescence-based fiber optic bio-sniffers for the detection of acetaldehyde (AcH) from exhaled breath [104]. These bio-sniffers were calibrated with two different enzyme-mediated environments: alcohol dehydrogenase (ADH) and aldehyde dehydrogenase (ALDH), which make the sensor selective for AcH. It was operated over a wide dynamic range from 0.02 to 10 ppm, which covered the physiological range of breath AcH (1.2 ppm – 6 ppm) and showed rapid response (≤ 100s), as shown in Figure 2-2a and 2-2b. In another study, it was seen that ALDH2 extensively dominates the metabolic oxidation of AcH into acetic acid, with about 40% of Asians known to have lower metabolic action of ALDH2 (ALDH2[−]) than the others (ALDH2[+]) [105]. The bifurcated fiber optic bio-sniffers (Figure 2-2c) could be distinguished from ALDH2[−]) to (ALDH2[+] by 3-times greater signal, as shown in Figure 2-2d. Contrarily, Reddy et al. developed a hybrid FPC sensor for VOC detection on a micro-fabricated chip functionalized with μ-GC, employing a vapor-sensitive polymer on the substrate, as shown in Figure 2-2e [106]. The sensing mechanism relies on the alteration of the refractive index

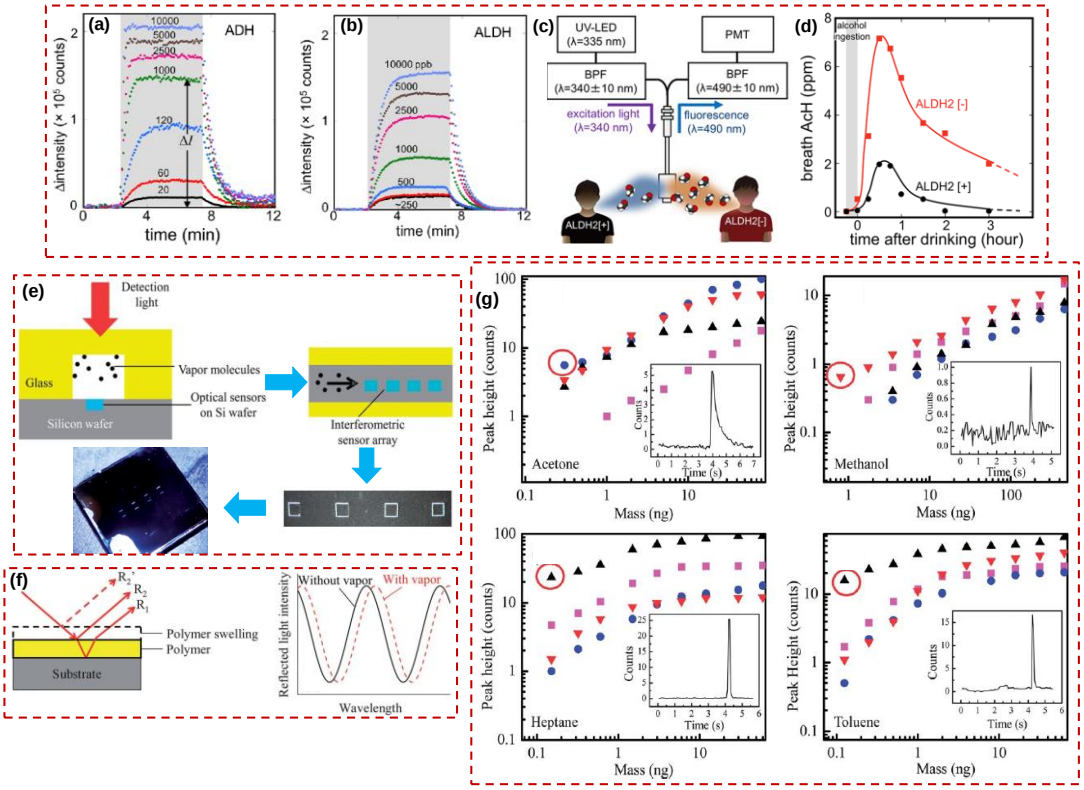

Figure 2-2: Responses of (a) ADH-mediated and (b) ALDH-mediated fiber optic bio-sniffer to different concentrations of AcH [104]. (c) Bifurcated fiber optic bio-sniffers set-up to the ALDH2[+] and ALDH2[−] subjects [104], (d) Their time course of concentration of breath AcH after drinking which is about 3-fold difference at the concentration level [104]. (e) Cross-sectional view of the FP sensor array (top left), Top-view of the FP sensor array (top right), Image of an etched silicon chip containing the sensor array (bottom right), Image of 4 wells on chip (bottom left) [106], (f) principle of the Fabry–Perot cavity (FPC) sensor and interference pattern generated by an FP sensor and the effect of analyte absorption absorbance properties of light [106], (g) chromatographic responses of four FP sensors to a mixture of acetone , methanol, heptane, and toluene [106].

with the concentration of VOCs (Figure 2-2f). The presence of the VOC in the polymer alters its thickness, which in turn changes its refractive index and shifts the wavelength to the degree of vapor sorption (Figure 2-2g). The kinetic and quantitative information of VOCs are obtained through the wavelength shifts inside the microfluidic channel. In the work of Reddy et al., chromatographic responses of four FPC sensors were grating sensors,

μ-ring resonator sensors, photonic crystal obtained (Figure 2-2g) from a mixture of acetone (1), methanol (2), heptane (3), and toluene (4). Scholten et al. also developed an on-chip μ-ring resonator integrated with fluidic connections and optical fiber probes for sensing five different kinds of VOCs. Their findings revealed five different peaks, confirming the level of sensitivities in the following order of ethylbenzene, toluene, perchloroethylene, isopropyl alcohol and heptane, respectively [107]. Contrarily, Xiaoyi Mu mentioned a bioluminescent bio-reporter-integrated-circuit technique for detection of breath toluene from bioluminescent bacteria, through the translation of biochemical energy to photonic energy. Though this method limited the target analyte to specific bacteria with very low (10 ppb) limits of detection (LoD), its longer response time (few minutes to hours) proved to be a hindrance to real-time monitoring [96]. Thus, the specific detection of a single analyte on a miniaturized scale with the development of a single optical sensor is a challenge. Therefore, Mazzone's group demonstrated the colorimetric sensor array combined with the prediction model to diagnose lung cancer. In their study, they collected 229 subjects' data and diagnosed 92 individuals as carcinogenic patients with the accuracy of 0.8 C-statistics [108]. A portable breath analyzer based on colorimetric detection that analyzed the data, processed it and communicated the information to the user via a cell phone for selective nitric oxide sensing in ppb-level (~ 50 ppbv) was also reportedly devised by Prabhakar et al. [109].

2.3.2 Chemi-resistive sensors

Different monolithic metal-oxide-based chemi-resistive sensors have been receiving attention due to their high potential for miniaturization to develop portable and

wearable diagnostic tools. The operating principle of these sensors relies on the variation of resistivity with the depletion layer due to redox reaction, adsorption, and surface chemical reaction of analytes [110]. The width of the depletion layer is either reduced or increased in the n-type metal oxide. The commonly used n-type metal oxides, namely tin oxide (SnO_2), tungsten oxide (WO_3), and zinc oxide (ZnO), are widely used for VOC sensing [111]. In the absence of VOC molecules, the presence of atmospheric oxygen species O^-, O^{2-}, or O^{2-} attributes electrons, which increase the depletion layer and resistivity, and vice versa. The relationship between the reaction mechanism and electrical signal can be expressed by the Langmuir-Hinshelwood equation as follows [112]:

$$S(t) = S_{max} \frac{C_{voc}K}{1+ C_{voc}K} [1 - \exp(- \frac{1+ C_{voc}K}{K} kt)] \qquad (9)$$

Here, S_{max} is the highest signal change in complete saturation, C_{voc} represents the concentration of VOC, K is defined as the adsorption constant of the target compound, and k represents forward rate constant.

P-type (nickel oxide, cobalt oxide) and zeolite-type MOS sensors are also used in the detection of VOCs [113 114]. Zeolite-based chemi-resistive sensors were reported for different VOCs, such as NH_3, amine, SO_2, different hydrocarbons and organic molecules [115]. The sensitivity and selectivity of any type of chemi-resistive sensor depends on the film thickness and working temperature [110]. Song et al described a ZnO–SnO_2 nanofiber-based ethanol gas sensor operating at 300 °C, providing high response, excellent linearity in the range of 1–300 ppm, quick response time (5s) and recovery time (6s), good reproducibility, stability, and selectivity [116]. Different metal oxide nanowires and ferroelectric WO_3 nanoparticles have been utilized for selective acetone sensing in breath-simulated media [114]. Choi et al. demonstrated a catalyst-functionalized method using

metal nano-particles (Pt) incorporated with WO_3 hemitubes for highly sensitive acetone sensing at the operating temperature 250 - 350 °C [117]. In their work, Pt-functionalized WO_3 hemitubes exhibited superior acetone sensitivity in the presence of H_2S. Righettoni et al. also performed in-depth studies on detecting of acetone in exhaled breath using Si-doped WO_3 nanoparticles (Figure 2-3a) for the diagnosing of physical conditions including halitosis and diabetes [118]. In his work, it was clearly inferred that the nanowires' response is greater than nanoparticles and nanoplatelets as a function of temperature for H_2S (Figure 2-3b). He also demonstrated thin-walled WO_3 hemitubes made by polymeric fiber-templating-based sensors operating at 350 °C for the diagnosis of halitosis and diabetes, detecting H_2S and acetone (~ 120 ppb), respectively (Figure 2-3c) [118]. Similarly, Fioravanti et al. demonstrated sub-ppm level acetone sensing with several metal-oxide materials: several ZnO nanoparticles (ZnO bi-sphenoidal nano-aggregates, ZBP; ZnO nanosheets, ZnS; ZnO hexagonal prisms, ZEP), aggregated ZnO nanostructures with Zr-loaded WO_3, and $TiO.5SnO.5O_2$, where ZnO nanoparticles-based sensors exhibited better sensitivity than others (Figure 2-3d-2-3g) [119]. Employing vanadium pentoxide (V_2O_5) nanobelts, Liu et al. improved the performance of selectivity to ethanol in a multivariate environment at relatively low temperatures (150 °C) to save the overall power consumption [120].

However, most of these chemi-resistive sensors require a high temperature to operate [121 122]. Moreover, semiconductor metal oxide-based sensors are more prone to interference and contamination in VOC detection. Portable, cost-effective breathalyzers (e.g. Figaro, Ketonix, BACtrack) are also commercially available for alcohol and acetone detection; meanwhile, wearable chemi-resistive sensors are still a challenge. Recently,

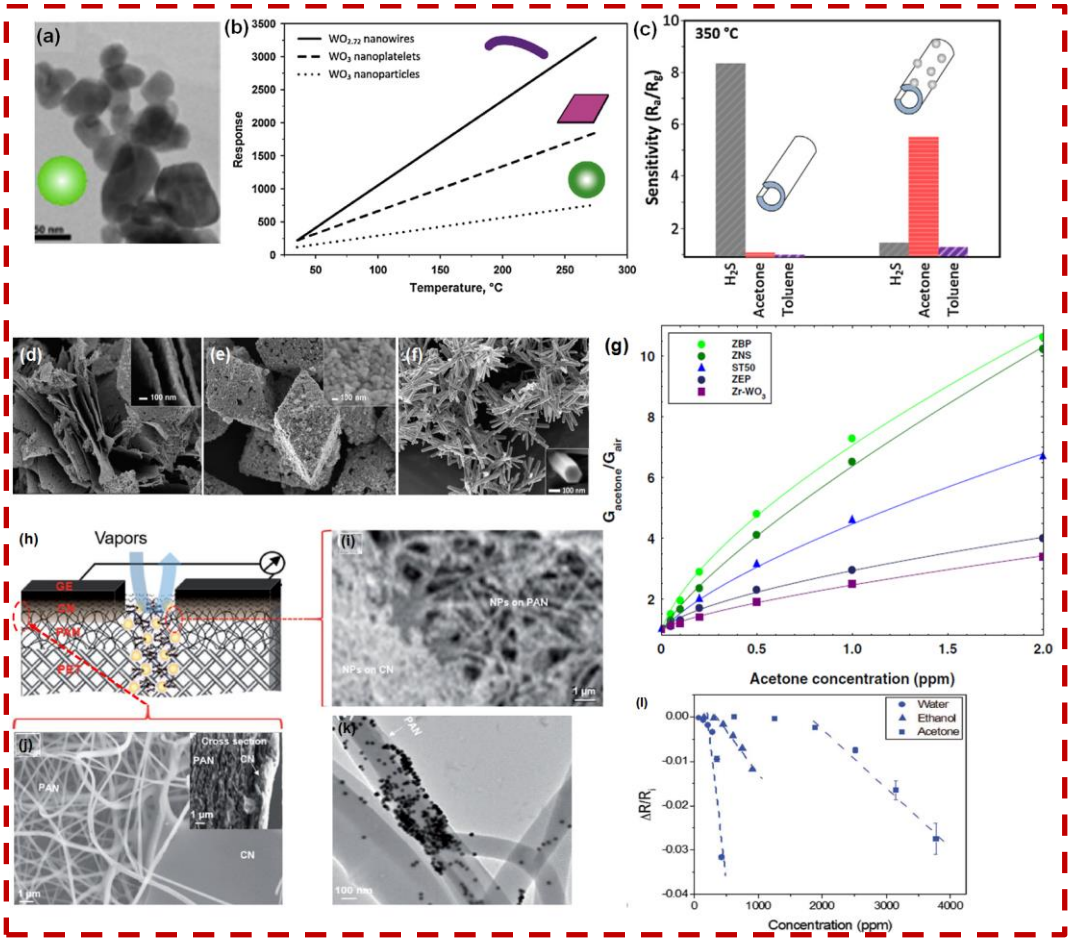

Figure 2-3: (a) SEM image of WO_3 nanoparticles [118], (b) WO_3 based sensor response to 1000 ppm H_2S for different structures as a function of temperature [118], (c) H_2S and acetone response characteristics of WO_3-based sensor [110]. SEM images of (d) ZNS, (e) ZBP and (f) ZEP, (g) Acetone response characteristics for different nanoparticles-based sensors [119]. SEM and TEM images (h, I, j, k) of the nano-fibrous paper and schematic of nano-fibrous paper-based sensor [124], and (l) the sensor response sensitivities (ppm (M): water (-1.9×10^{-4}), ethanol (-1.5×10^{-5}), and acetone (-1.1×10^{-5}) [124].

Tayebi et al. reported monolithic, micro-fabricated sensor arrays comprising different metal oxides, allowing independent temperature controls and readouts for VOC sensing on a wearable platform [123]. Though many breathalyzers are chemi-resistive-based, their high operating temperature and power management are key obstacles to overcome for

design on a wearable platform [121]. Yan et al. illustrated nano-fibrous paper-based chemi-resistive sensor fabricated with dendronized nanoparticles that show structurally tunable and negative signals in presence of ethanol and acetone at room temperature (Figure 2-3h-2-3i) [124]. In their work, the electrical properties of the nano-fibrous membrane matrix with dendronized nanoparticles are harnessed for exploring the multiple hydrophilic/hydrogen bonding sites in a 3D structural edge for sensing applications in humidity-leading atmosphere, such as human breathing or sweating.

2.3.3 Electrochemical sensors

Electrochemical VOC sensors are considered among the most promising types of VOC sensors for wearables today. Electrochemical sensors work on the principle of redox reactions that target analytes undergo to produce measures, which correlate with the concentration of the analyte [97]. These sensors can be classified as: voltammetric, amperometric, or potentiometric. These kinds of techniques are most compatible for wearable sensing due to the ease of fabrication and miniaturization, rapid response, high accuracy, wide range of detection, biocompatibility, and low power consumption [110].

Portable electrochemical sensors, like breathalyzers are available for alcohols, aldehydes, acetones, isoprene, etc. Portable Halimeter® (114 × 254 ×267 mm/3.6 kg) is popular for VSC (volatile sulfur compounds, e.g. hydrogen sulfide, methyl mercaptan, other thiols, and dimethyl sulfide) sensing for chronic halitosis following the electrochemical voltammetric technique, which shows a detection limit of 5 ppb with response time of 1s [125]. Apart from this, fuel-cell-based miniaturized and portable alcohol breathalyzers are popular and widely used for drinking under the influence (DUI)

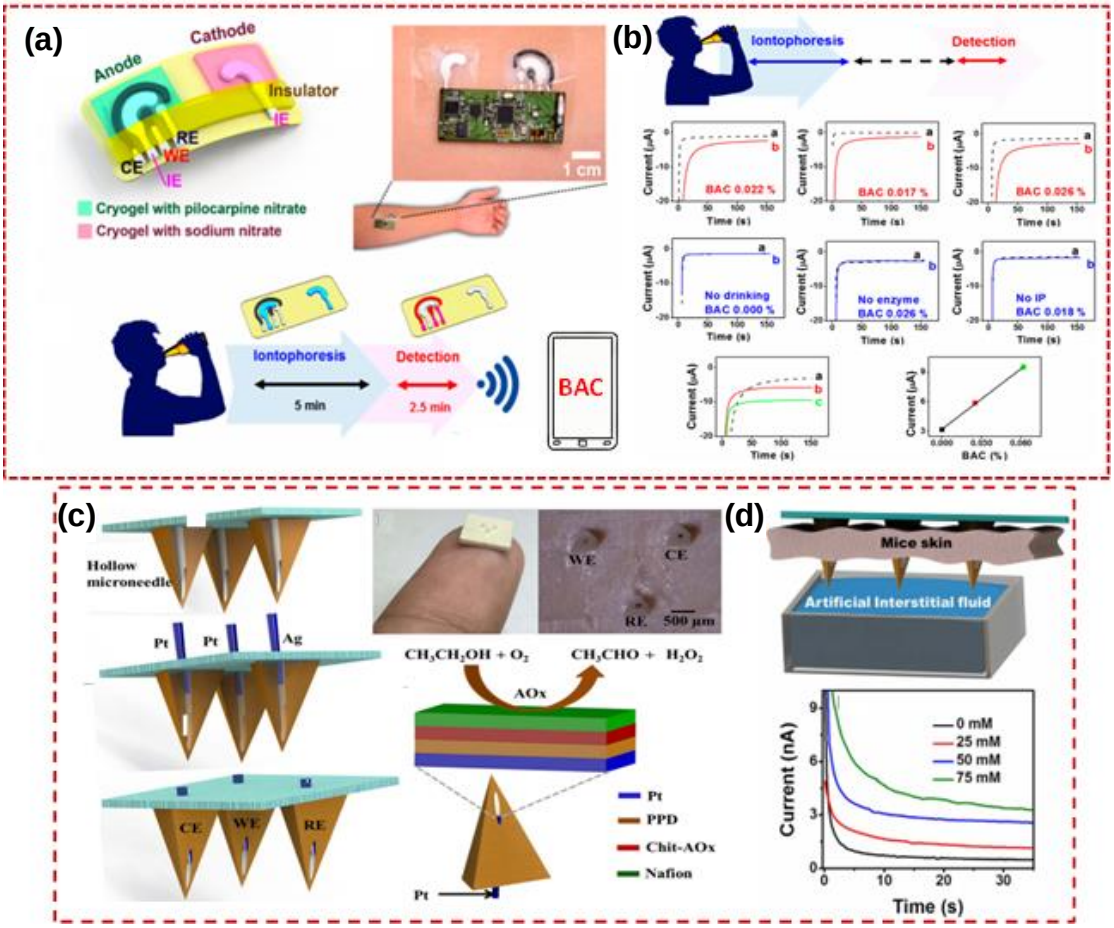

Figure 2-4: (a) Tattoo-based transdermal alcohol sensor and (b) its responses [130]. (c) schematic representation of micro-needle based chrono-amperometric sensor and (d) its responses [131].

cases in real-time but cannot be used for continuous measurements [33 126]. Obermeier reported integrated e-noses with three different amperometric sensors for the detection of aldehyde, NO, and CO at sub-ppb levels for the diagnosis of lung cancer and treatment of those succumbing to oxidative stress [127]. Electrochemical sensing techniques have also been reported for continuous monitoring of propofolin exhaled breath of patients under anesthesia [128]. However, miniaturization is essential for the embedded sensing device in the continuous monitoring and POC wellness management. A significant advancement

towards wearables for continuous monitoring of alcohol from sweat or skin perspiration was achieved in the last few decades. Field trials of the sweat patch identified problems with ethanol collection and storage, evaporation loss, back diffusion, and bacterial metabolism [129]. Giner's wrisTAS and SCRAM CAM bracelet are partially instantaneous (5 minutes to 2 hrs. interval) alcohol monitoring devices, through skin perspiration, using electro-chemical sensors [129 130]. These anklet and bracelet-based transdermal blood alcohol content (BAC) monitoring devices are used in semi-real-time and a continuous manner for preventing DUI and rehabilitation purposes. Kim et al. demonstrated integrated wearable epidermal tattoo-based amperometric biosensors with flexible iontophoretic sensing electrodes to improve the time in detection (Figure 2-4a– 2-4b) [130]. This new, skin-worn, low-cost, noninvasive alcohol monitoring device enables real-time alcohol measurements in sweat. BAC can be calculated from the following relationship [130]:

$$\text{BAC } (gl^{-1}) = 0.71 \times \text{sweat ethanol concentration } (gl^{-1}) \quad (10)$$

where, r = 0.912. Mohan et al. demonstrated a micro-needle-based enzymatic electrochemical sensor for minimally-invasive, continuous monitoring of alcohol from interstitial fluid (ISF). Their three-electrode micro-needle sensor comprised of Pt and Ag wires with the Pt-wire functionalized with the alcohol oxidase (AOx) enzyme and a perm-selective reagent layer (Figure 2-4c). The sensitivity of this sensor was known to be 0.062 nA/mM, having a correlation coefficient of 0.9886 (Figure 2-4d) [131].

An overview of sensing techniques, target VOC(s) and their availability in biofluids are listed in table 2-1.

Table 2-1. Comparative analysis of different sensing methods

Sensing method	Target VOC (s)	Biofluid	Detection Limit	Response time	Purpose
GC-MS [132]	VSC	Breath	1 ppb	480s	Halitosis
Chemi-resistive [133]	VSC	Breath	10 ppb	45s	Halitosis
Chemi-resistive [134]	H2S	Breath	50 ppb		Halitosis
Electrochemical [135]	VSC	Breath	5 ppb	< 1s	Halitosis
Chemi-resistive [136]	H_2S	Breath	100 ppb	18s	Halitosis
Chemi-resistive [137]	H_2S	Breath		1s – 2s	Halitosis
Chemi-resistive [138]	H_2S	Breath	0.3 ppm		Halitosis
Chemi-resistive [139]	H_2S	Breath	100 ppb	8.4s – 11.6 s	Halitosis
Electrrochemical (fuel cell) [84]	Ethanol	Skin perspiration	5 ppm	5s	DUI

Chemi-resistive [140]	Acetone	Breath	1 ppm		Diabetes
Chemi-resistive [141]	Acetone	Breath	0.12 ppm	300s	Diabetes
Chemi-resistive [139]	Acetone	Breath	100 ppb	< 15s	Diabetes
Chemi-resistive [141]	Acetone	Breath	120 ppb	300s	Diabetes
Chemi-resistive [142]	Acetone	Breath	10 ppm	9s	Diabetes
Chemi-resistive [143]	Acetone	Breath	1 ppm	0.5s	Diabetes
Chemi-resistive [144]	Acetone	Breath	20 ppb	78s	Diabetes
Chemi-resistive [145]	Acetone	Breath	200 ppb	3s -9s	Diabetes
Chemi-resistive [146]	Acetone	Breath	120 ppb	15s	Diabetes
Chemi-resistive [147]	Acetone	Breath	50 ppb	30s	Diabetes
µ-GC–MS [148]	2-butanone, methyl acetate, toluene, m-		0.04 – 0.11 ppb	15 min	Occupational health

	xylene, isobutyl acetate				
µGC- µCR [88]	Benzene, heptane, toluene, methyl isobutyl ketone, butyl acetate, m-xylene		100 ppm	~ 10 min.	Occupational health
PID [149]	Benzene	Breath	10 ppm	1.5s	Occupational health
PID [106]	benzene, toluene, ethylbenzene, xylene	Breath	10 ppb		Occupational health
Fabry–Perot interferometer [150]	acetone, methanol, heptane, toluene		~ 25 ppb	60 ms	
GC/MS [151]	pentane	Breath	10 -12 mol/l		schizophrenia
GC/MS [152]	methylated alkane, pentane, formaldehyde	Breath	10 -12 mol/l		Breast cancer
Tunable laser absorption	Carbonyl sulfide (COS)	Breath	30 ppb	50 ms	Liver and lung diseases

spectroscopy [153]					
Chemi-resistive [154]	Ethanol		10 ppm	4s	DUI
Chemi-resistive [155]	Isoprene	Breath	1 ppm	65s	Flu Virus
Chemi-resistive [119]	Acetone	Breath	0.1 ppm	40 – 60s	diabetes
GC-MS [156]	Propofol	Breath	2.8 – 22.5 ppb		anesthesia
Electrochemical fuel cell [127]	Aldehydes	Breath	1 ppmv	22 s	oxidative stress/ cancer
Electrochemical (micro-needle) [131]	Alcohol	Interstitial fluid	5 mM	30s	DUI
Electrochemical (tattoo) [130]	Ethanol	Sweat	52 ppm	7.5 min	DUI

2.4 Challenges and solutions for precise detection of VOCs in real-time

Clinical diagnosis of VOCs faced several challenges associated with the detection of ultra-low concentrations of target molecules in a collective, complex multivariate

environment. The development of continuous monitoring of VOC sensors faces several challenges in many respects, mostly from the following major fronts: i. standardizing sensors' calibration, ii. development of wearable devices, iii. complexities of metabolism and VOCs' kinetics in a multi-analyte system, and iv. inter/intra- person variability of VOCs' profiles in such varied environments. Human anatomy and physiology is identical, therefore, the standardization of a generic sensing device for a specific VOC detection is critical. For the same person, the pharmacokinetics and kinetics of different VOCs can differ from time to time, depending on diet, drug consumption, body temperature, ambient environment and physiological condition. Moreover, most sensors are influenced by the fluctuation of these ambient parameters and exogenous compounds that generate false positive readings [33 130 157]. The performance of a sensor degrades with time due to the aging effect, contamination, the corrosion of materials and the alteration of internal properties due to chemical or physical variables (e.g. temperature, humidity, pressure, etc.) [33 113 130]. Different sensing parameters, such as reliability, sensitivity, selectivity, stability and reversibility are crucial in implementing the design of the sensor in the wearable platform. The major challenges and their possible solutions on major parameters of different VOC sensing in humans are described below.

2.4.1 Sensitivity

The precise detection of low concentration is always a challenge in VOC sensing. Different analytical techniques are widely used in breath analysis to trace sub-ppm concentrations of VOCs [4 6 158]. Solid-state chemi-resistive, optical and electrochemical

sensors have also attracted attention in VOC detection due to their miniaturization and portability, higher sensitivity, and detection limit. The sensitivity of the sensor can be measured as in Equation 11 below:

$$S = \frac{R_{air} - R_{gas}}{R_{air}} \text{ x } 100 \qquad (11)$$

where, R_{air} and R_{gas} are the sensor resistances in normal air and under gas. Bur et al. improved sensitivity trough platinum gate gas-sensitive SiC field-effect transistor (SiC-FET), having a detection limit of ~1 ppb for benzene and naphthalene and ~10 ppb for formaldehyde in humid atmospheres [159]. Barsen et al. developed screen-printed ceramic MOS sensors, which achieved detection limits as low as at sub-ppb levels, utilizing the recognized grain-boundary effect [160]. Different amplification protocols that target recycling and the proper selection of transducers have also been seen to improve the sensitivity and detection limit. The use of nanoparticles in different forms, such as nanowires, nanoflakes, nanorods, nanofibers, nanotubes, nano-spheres, and other nanostructures, reportedly improve the sensitivity manifold in VOC sensors by increasing the surface area. Modifying the nanoparticles and pore size in the synthesis of nanocubes and nanorods of SnO_2, Kida's group improved the sensitivity to 5 orders of magnitude in response to 100 ppm of ethanol on an optical sensing film [161]. Recently, Marques and McKnight referred to the sensitivity of alcohol monitoring devices (SCRAM for transdermal alcohol content) which were 65.3% and 86.5% for 0.02 g/dL and 0.08 g/dL concentrations, respectively [162].

2.4.2 Selectivity

Cross-selectivity of sensors in a multivariate system is a prime concern in the detection of biomarkers. Non-specific detection of the existing sensors can generate false positive errors during measurements, from interactions with interfering compounds [130 157]. For example, anbesol, containing benzyl alcohol, is an anesthetic oral pain relief gel used to treat toothaches and canker sores that can yield a positive BAC reading. To improve the selectivity of the VOC sensors, different approaches can be employed. Selective catalysts or nanoparticles can improve the signal-to-noise-ratio in the detection of the target VOC [163 164]. In some cases, the size, shape and phase composition of the nanoparticles play a role in differentiating different VOCs [165]. Pure and Si-doped WO_3 nanoparticles based on chemi-resistive sensors allow the detection of acetone in ppb levels of concentration (~ 20 ppb), with a high signal-to-noise ratio [118]. It was found that Si-doping increases and stabilizes the acetone-selective ε-WO_3 phase, while increasing its thermal stability and sensing performance. Zhang et al. mentioned Ag-doped In_2O_3-activated sensors for the selective detection of alcohol in presence of acetone, formaldehyde, ammonia, and H_2 at low temperatures [166]. Cr_2O_3 nanoparticle-based chemi-resistive sensors are also known to have shown a better response to NH_3 in the presence of other VOCs of higher concentrations at room temperature [111]. Doping of specific metal molecules in various metal oxides improves the selective detection of some VOCs [114]. Lanthanum-doped nano-crystalline thin-film of $LaFeO_3$ demonstrated excellent selectivity and stability for the detection of ethanol in the transdermal range [167].

Polarity is another important factor that plays a role in VOC sensing, while polar and non-polar VOCs are selective to specific catalyst materials. The catalyst sensing element itself or the thin film of functionalized nanostructures on the sensing element can easily react with the polar compound through charge transfer and avoid reactions with non-polar VOCs [168]. For example, a thin layer of self-assembled polycyclic aromatic hydrocarbon (PAH) covering RN-CNT chemi-resistive films could discriminate between polar and non-polar VOCs in a controlled environment. Using pulsed laser deposition (PLD), morphology of highly porous sensing layers has been known to contribute towards enhanced the selective detection of naphthalene [169]. Secondly, a different dynamic approach can improve the selectivity of VOC sensors. For example, temperature-cycled operation (TCO) is accepted as a vigorous and adaptable technique, especially in chemi-resistive sensors where a certain temperature window is dedicated for specific types of compounds [170]. In a mixture of carbon monoxide, hydrogen and selective sorbent material (e.g., Tenax®, Car bopack X, Carboxen) is known to have the ability to entrap specific VOCs through thermal desorption (TD). Although the mentioned approaches improve selectivity, the detection of a specific compound from a multi-analyte system requires more robust techniques.

Recently, data mining and pattern recognition techniques have become popular and established tools to interpret datasets from a multidimensional environment, with precise measurement and classification of the volatile compound being measured. For precise calibration, the system needs to have multiple wearable “e-noses.” Therefore, large and diverse data sets can be acquired based on diurnal activities and performances of the wearer. After acquiring the raw data from multiple input systems, it needs to be processed

using machine learning or deep learning tools. These tools are suitable to train the algorithms on dependent and independent variables and provide a desired estimation for a precise calibration model for individual VOCs [171]. Different machine learning tools [172 173 174 175], such as PCA, canonic discriminant analysis (CDA), independent component analysis (ICA), DFA, PLS, artificial neural networks (ANNs), support vector machine (SVM) and hierarchical cluster analysis (HCA), have been reported to be adopted for specific VOC detection [21 22 23]. However, once a method of prediction has been established, the predictive accuracy is obtained through cross-validation of all the data sets. The prediction model improves the correlation of the data sets and infers a pattern, whereas the regression technique provides a specific concentration of the unknown value of future data streams in real-time through fitting with this pattern [40 176]. Mazzone's group (Cleveland Clinic) demonstrated a chemi-resistive sensor array for the detection of lung cancer from exhaled breath [177]. They applied PCA and CDA techniques for the classification of malignancy and benignity of lung cells, and SVM was employed to generate a prediction model from the data. Their sensors demonstrated a sensitivity of 71.4% and high specificity (91.9%) for lung cancer diagnosis. Similarly, Kim et al. studied WO_3-based (or its alloy) sensor arrays to understand the selectivity of acetone in the presence of H_2S, H_2, CO, ethanol and toluene (Figure 2-5a). In his study, they showed how mixture of the VOCs could be selectively detected without interference employing PCA (Figure 2-5b) [22]. They also showed how overlapped signals of healthy breath and halitosis breath could be differentiated using PCA (Figure 2-5c). Saidi et al. applied the PCA method for the classification of Chronic Kidney Disease (CKD), diabetes mellitus (DM), Healthy Subjects with High Creatinine (HSHC) and Healthy Subjects with low

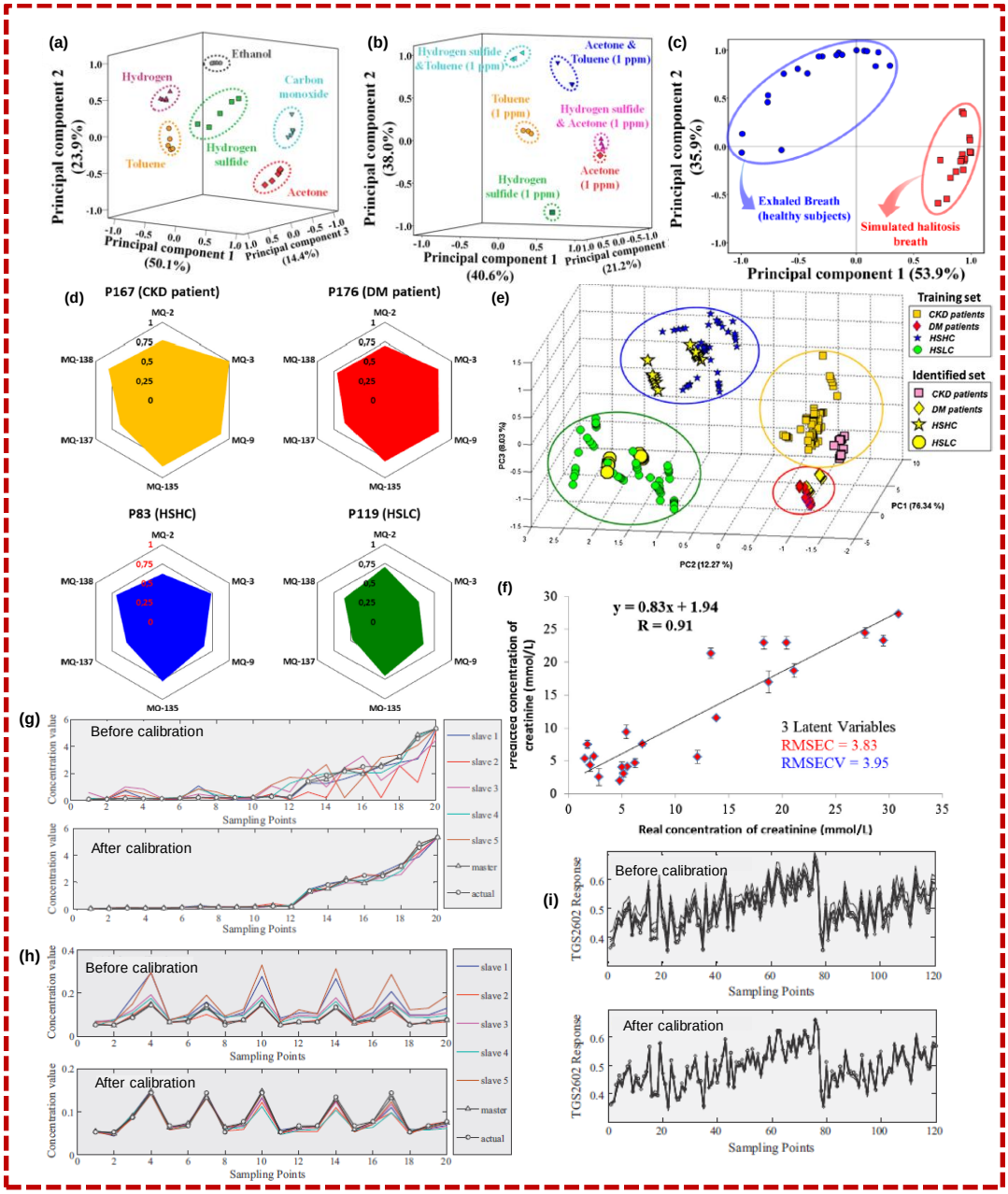

Figure 2-5: (a) The application of PCA for multiple biomarkers' classification [22], (b) The classification of their mixtures using PCA [22], (c) Classification between simulated halitosis breath and healthy human breath [22], (d) Radar plots of four breath samples expressed as the area under conductance of temporal responses gathered from e-nose for CKD and DM patients and healthy subjects [23], (e) The PCA model built using the first set of measurements, fitting the second data set onto the clusters [23], (f) The PLS prediction model for creatinine content in the urine [23], (g) TGS2602 responses with 120 samples measured before and after calibration, performance of predicted concentrations on test samples (before and after calibration): (h) formaldehyde, and (i) benzene [190].

Creatinine (HSLC) [23]. The radar plot is derived from e-nose responses, which demonstrated a significant distinction between the four different patterns, as shown in Figure 5d. The PCA and SVMs' results also presented a clear classification among the four groups. Moreover, this classification was further validated by analyzing 48 different samples from 8 new volunteers, which coordinated with the PCA model (Figure 2-5e). They also demonstrated the PLS model, which shows a significant correlation of 0.91 between the e-noses' results, as shown in Figure 2-5f [23]. Similarly, M. Philip et al. applied the Fuzzy logic model for the prediction of breast cancer with improved accuracy to their previously mentioned findings [178]. These studies reveal the prospects of machine learning toward the in-situ detection of specific VOC in a multi-analyte system.

2.4.3 Stability

The stability and shelf life of any VOC sensors are crucial parameters to consider when designing a sensor for POC application. These features affect a sensor's reliability; and any false readings can be generated because of its instability. Multiple parameters, like relative humidity or temperature, and operational conditions (e.g. applied voltage) can change the sensor's properties (e.g. impedance) in real-time. Hence, most of the VOC sensors require manual calibration or additional controlling equipment during measurements. However, wearable sensors are concerned with detection at sub-ppm or ppb levels in real-time. In an environment where humidity, pressure, and temperature change erratically, a minute's change of humidity, pressure or temperature can cause significant variation in the signals that affect the calibration of a sensor. Potyrailo et al. established humidity and temperature as factors that can affect the calibration of methanol and ethanol

in detection [179]. Similarly, the signals of a fuel cell sensor directly depend on humidity and temperature [33]. Additionally, other intrinsic or extrinsic properties of the sensors, such as structure alteration, phase conversion, poisoning, degradation, bulk diffusion or interference, may cause shifts in the baseline signal of the sensor with time [180]. Moreover, continuous exposure of any VOCs may instigate fouling effects, chemical alteration, and hysteresis (irreversible) nonspecific adsorption on the sensor surface [181].

Different approaches were considered to improve the stability. Deng et al. demonstrated improvements in the stability of thermodynamic properties of known unstable sensing materials (molecularly imprinted polymer, MIP) for the Quartz Tuning Fork (QTF) sensor [182]. This has been reported through the modification of MIP by mixing polystyrene. Their study showed the adsorption response increased with rising temperature for a new sensor, while it is vice-versa for an aged one. Their thermodynamic analysis on the calibrated data for VOC (e.g. o-xylene) demonstrated that a conversion takes place from endothermic to exothermic reaction through the alteration of MIP, which improves its stability and aging effect. Contrarily, different thermally stable metal oxides, such as ZnO, SnO_2, TiO_2, WO_3, In_2O_3, TeO_2, and Co_3O_4, formed thin film nanostructures in SAW sensors to improve thermal stability through controlling chemisorption or redox reaction of the target VOCs at certain elevated temperatures. This temperature-dependent property also enhances sensitivity and selectivity for specific VOCs [26]. However, Nguyen mentioned Ti_nO_{2n-1} as a good catalyst to improve the stability of the ethanol fuel cell sensor [183]. Similarly, Pt is widely used as a catalyst in fuel-cell sensing due to its high resistivity to corrosion, allowing a stable electrical response [184]. A multi-varied sensing platform integrated with different e-noses can potentially improve selectivity and

reliability through various tools, as mentioned earlier. This sensing platform acquires a multidimensional signature from diverse transducers collectively, in which data are collected and processed using machine learning tools and pattern generation [185 186 187 188 189]. Zhang et al. explored global affine transformation (GAT) and the Kennard–Stone sequential algorithm (KSS) model for the calibration of SnO_2 based e-noses for formaldehyde and benzene sensing (Figure 2-5g – 2-5i) [190]. The pattern matching relies on affine transformation, which can be extracted from the robust weighted least square (RWLS) algorithm and the Euclidean distance (dz) of the samples in the subspace. To evaluate the performance, the root mean square error of prediction (RMSEP) and mean absolute relative error of prediction (MAREP) were calculated from equations 12 and 13, as follows:

$$RMSEP = \sqrt{\frac{1}{n}}\sum_{n=1}^{N}(\varphi_n - T_n)^2 \qquad (12)$$

$$MAREP = \sqrt{\frac{1}{n}}\left|\sum_{n=1}^{N}(\varphi_n - T_n)\right| \qquad (13)$$

where φ_n and T_n denote the projected and real concentration samples for the nth variable, respectively. The applied algorithm eliminates the drifting effect and noise. Thus, any drift in response and interference issues can be minimized with desired quantification, considering known parameters affect the response.

2.5 Conclusion

VOCs as biomarkers provide a potential pathway for the simple, direct, and effective monitoring of certain health conditions, as discussed. However, challenges facing

the field of wearable VOC detection were addressed in the reliable calibration of a single biosensor. The sensitivity of the VOC sensors can improve significantly through the advancement of nanotechnology. However, specific detection by a single sensor from a multivariate surrounding is yet to be overcome in precise, accurate sensing for wearable applications. Most breathalyzer-based devices show 20% - 40% error, which makes these devices inefficient. G. Simpson mentioned that 90% of this ambiguity is due to the biological variables of the subject, and at least 23% of subjects will have their actual BAC overestimated [191]. However, the advancement of nanotechnology and micromachining promote the integration of multiple sensing modalities on a single platform. The integration of e-noses in a multimodal sensing platform through sensor-fusion have helped to do away with certain issues of selectivity in the specific diagnosis of a physiological condition of an individual. Pattern recognition and machine learning or deep learning tools have been being employed in multimodal sensing approaches via e-noses for precision and accuracy, as aforementioned. Such prospects provide pathways for the noninvasive detection of VOCs as biomarkers on a wearable platform for POC continuous monitoring and personal health management in real-time.

In summary, this chapter presented a comprehensive literature review on sensing VOCs as biomarkers in humans. The potential sources of different VOCs for POC diagnosis in real-time were explored. Different sensing techniques and their challenges were elucidated. The probable solutions to resolve these challenges were delineated at the end of this chapter.

CHAPTER III

PROTON EXCHANGE MEMBRANE (PEM) FUEL CELL SENSOR, ITS FABRICATION AND CHARACTERIZATION

A proton exchange membrane fuel cell (PEMFC) has a multitude of applications, such as power generation, for transportation and stationary systems, such as powered vehicles, uninterruptible power supply (UPS), and mobile phone station and sensing of volatile compounds (e.g. ethanol, methanol, CO etc.). For the application of sensing, a fuel cell sensor needs to provide stable and interference-free signals with accurate and precise calibration. In this chapter, the first section presents the working mechanism of a PEM fuel cell sensor and the reasoning for the selection of nickel as a catalyst material. The final section discusses the fabrication process of nickel and monel (nickel alloy) catalysts-based fuel cell sensors.

3.1 Polymer electrolyte membrane fuel cell (PEMFC) structure

The polymer electrolyte membrane (PEM) fuel cell, also termed proton exchange membrane fuel cell, employs a proton-conducting polymer membrane as an electrolyte. Fundamentally, the typical structure of a PEMFC consists of seven elements, as shown in Figure 3-1: [192]: i. feeding channels, ii. the diffusion layer, iii. the catalytic layer in the anode; iv. proton-conducting membrane; v. the catalytic layer in the cathode, vi. the diffusion layer, and vii. feeding channels in the cathode. The PEMFC combines in a unit, where the electrodes and the electrolytes are assembled in a very compact form. In

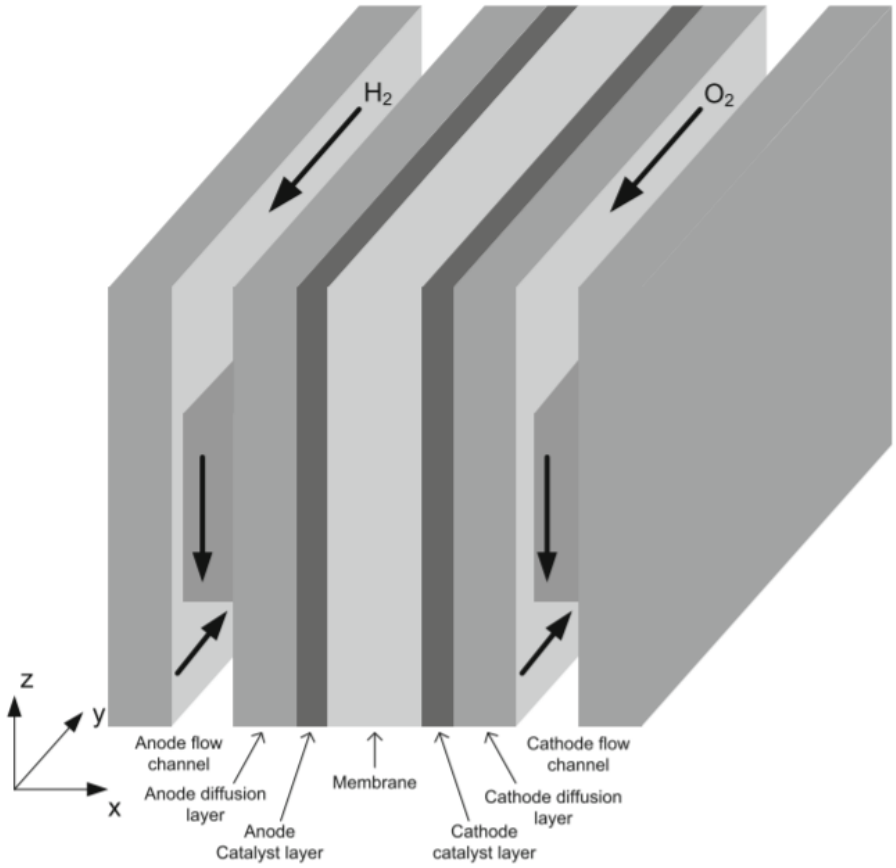

Figure 3-1: Three-dimensional schematic diagram of a fuel cell [192]

this structure, membrane electrode assembly (MEA) is the core part, where the membrane is sandwiched between the catalytic layers of anode and cathode. In figure 3-1, it is evident that fuel (here H_2) is oxidized at anode and oxygen (O_2) is reduced at cathode through the diffusion layers. Typically, feeding channels are essential parts for power generation, which are absent in sensing application.

3.2 PEM fuel cell for VOC sensing

The fuel cell sensor has high specificity, accuracy, calibration stability and a long working life compared to other kinds of sensors. However, different biosensors suffer from

high interference due to humidity, and they cannot be applied for continuous monitoring. For example, the ethanol sensor is widely used for the breathalyzer. These breathalyzers cannot be used for the continuous monitoring of ethanol for DUI offenders or for measuring blood alcohol concentration (BAC) through transdermal diffusion. The literature survey shows that there are a few reports for continuously monitoring alcohol through transdermal diffusion or perspiration with accuracy and precision. The present noninvasive way to measure the BAC is to measure the alcohol content in the breath. There are a few wearable continuous monitoring devices available because the pharmacokinetics of alcohol is complex due to the intricate nature of its distribution into the various tissues in the body. In detail, alcohol kinetics is dependent on absorption from the intestines into the blood, then elimination from the blood via the metabolism in the liver, and transportation into tissues via diffusion. This balance between absorption and the elimination of alcohol is reflected in the BAC. After a drink, the BAC rises until absorption is complete. After a maximum in the BAC is achieved, the BAC decreases during the elimination phase primarily due to the metabolism in the liver [5]. Therefore, the assumption that the supra-dermal ethanol concentration is the same as that of the BAC will lead to false positive or false negative results. Moreover, the noninvasive and continuous monitoring of alcohol sensors suffers from humidity or other interference in operations in a multivariate environment, and shows false readings. These issues can be overcome by continually monitoring the concentration curves and standardizing with the BAC.

In this research, a fuel cell-based sensor was constructed from different catalyst materials, such as stainless steel, nickel, and copper.

3.3 Fabrication of a fuel cell sensor

3.3.1. Materials and apparatus

A micro-perforated, stainless steel sheet (thickness 200 µm, 180 µm pore size) from the Advanced Materials Engineering Research Institute (AMERI) at Florida International University was used as the material for the electrodes. Copper, lead, and nickel sheets were purchased from McMaster-Carr and used for electro-deposition. Nafion424 reinforced with poly-tetrafluoro-ethylene (PTFE) as a PEM, 95% sulfuric acid, 37% hydrochloric acid, boric acid, copper sulphate, nickel chloride anhydrous, and nickel sulphamate were purchased from Sigma-Aldrich; these were utilized for the copper and nickel electroplating of stainless steel. Acetone and ethanol (95.27%) were purchased from Fisher Scientific Inc. The aqueous solutions were prepared with de-ionized (DI) water.

A hydraulic hot press (model 2100 from PHI) was used to prepare the sandwiched structure of the fuel cell sensor. For the electrochemical experiments, two potentiostat were utilized: CHI 1230B having MC470 and Autolab PGSTAT30. A 3D printer (model: Replicator2 from Makerbot) was employed for the chamber design of the experiments. A Bruker D5000 X-ray diffractometer from Siemens (presently Bruker) was used for the characterization of various catalysts.

3.3.2 Design and construction of the fuel cell sensor

The dimensions of the working (anode), counter (cathode), and reference electrodes were 1.5 cm x 0.8 cm, 1.5 cm x 1 cm and 1.5 cm x 0.2 cm, respectively (shown in Figure 3.2a). Since the counter electrode is the primary current collector, the overall

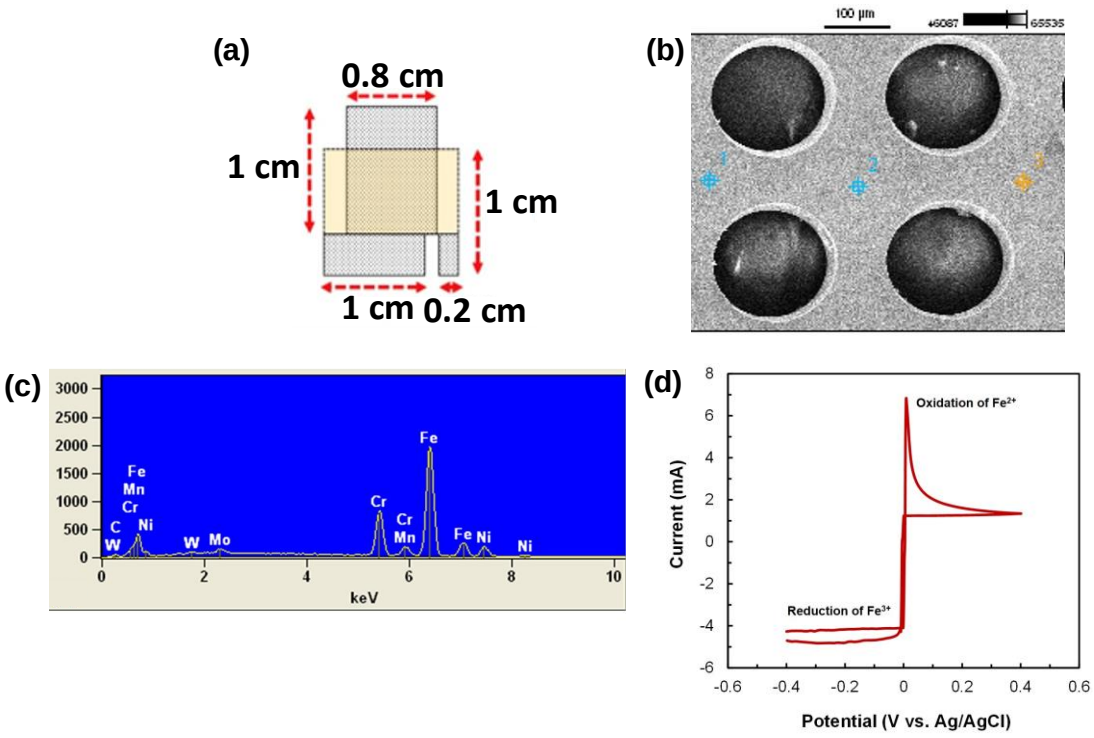

Figure 3-2: (a) Design of the PEM fuel cell; (b) SEM image of a stainless steel micro-perforated sheet, spots 1, 2 and 3 are the points for EDX measurement; (c) EDX spectrum of the stainless steel micro-perforated sheet; and Cyclic voltammogram of fuel cell type sensor containing Nafion membrane sandwiched between stainless steel electrodes. The scan rate was 0.02 Vs^{-1}. The CV was measured in the absence of ethanol and humidity.

dimensions of the counter electrode were designed to be substantially larger than the working and reference electrodes. In contrast, the dimensions of the reference electrode were designed to contain the smallest surface area. The electrolyte membrane, Nafion (1.5 cm x 1 cm) was sandwiched between the electrodes to form the MEA, which was assembled in a 3D-printed chamber. In the two electrode micro-fuel cell sensor, the anode was positioned on the PEM and the cathode was on the opposite facet, which was made of PTFE. The three-electrode fuel cell sensor followed the same structure as the two-electrode system, except that it had a reference electrode, which was placed near (1 mm) the counter electrode on the same PTFE facet. The sandwich structure of MEA was made by hot

pressing it at 75 ˚C and 2500 psi for 10 min. Before experiments, a constant relative humidity was maintained for each sensor by treating the sensors in the humidity chamber for 30 min at 24 ˚C.

Contrary to a traditional fuel cell two-electrode system, a three-electrode one was developed to monitor the signals in these studies. The three-electrode system is more advantageous than the two-electrode system. For example, the electrochemical potential measurement in the two-electrode system (anode and cathode) shows the full cell reaction potential, whereas when using the three-electrode system, the half-cell potential can be measured. In these studies, the three-electrode system was constructed in such a way that working and reference were nearer to each other (Figure 3-2a). This design facilitates monitoring the anodic reaction of the fuel cell sensor. The importance of the design and the electrochemical reactions of the fuel cell-type ethanol sensor will be described in the later sections.

The stainless-steel material (from AMERI lab) used for the fuel cell-type sensor construction was characterized using scanning electron microscope (SEM) and Energy-dispersive X-ray (EDX) spectroscopy. The pores were of uniform size, with the diameter of 180 µm, with the inter space distance of 100 µm (Figure 3-2 b). For EDX studies, the electron beam was targeted on the three spots, as marked in Figure 3-2a. The obtained EDX spectra (Figure 3-2c) show that the concentration of the iron was higher than all the elements present. This high concentration of iron with chromium, nickel, manganese and molybdenum represents stainless steel alloy. The weight percent calculation from the EDX data is given in Table 3-1. Comparing the composition of the materials in Table 3-1 with the literature proves that the stainless steel used in this work was the SS-304 type

Table 3-1. EDX spectrum analysis weight% data of micro-perforated stainless-steel sheet used in fuel cell type ethanol sensor.

	C	*Cr*	*Mn*	*Fe*	*Ni*	*Mo*	*W*
Spot 1	9.15	15.53	1.88	63.00	8.58	1.52	0.34
Spot 2	9.28	15.70	1.67	63.39	8.44	1.51	0.00
Spot 3	10.68	15.38	1.73	61.51	8.87	1.82	

C Carbon; *Cr* Chromium; *Mn* Manganese; *Fe* Iron; *Ni* Nickel; *Mo* Molybdenum; *W* Tungsten.

[193]. The carbon content listed in Table 3-1 is high compared to the composition in the stainless steel because it is hard to eliminate the carbon contamination surface of the analyzed sample. Similarly, tungsten impurity was noticed in the results, however it exists in a negligible amount. Even though the SS-304 type stainless steel was used as an example for these studies, the other stainless-steel alloys, metals, and carbon materials modified with nanomaterials can be used for the fuel cell-type ethanol sensor construction.

The electrochemical activity of the fuel cell-type sensor was measured using the cyclic voltammogram (CV) technique, as given in Figure 3-2d. The iron present in the electrodes showed a redox property during CV measurements. The CV measurements were carried out in the potential range of -0.4 to 0.4 V at the scan rate of 0.02 Vs^{-1}. In the CV (Figure 3-2d), the anodic peak potential of Fe^{2+} oxidation (E_{pa}) is at the same potential of the cathodic peak potential of Fe^{3+} reduction at formal potential $E_0 = 0$, where the peak separation $\Delta E = 0$. This result indicates the reaction is a highly surface-confined process, which proves: (i) the presence of iron on the electrode surface and (ii) the electrodes are electrochemically active and suitable for fuel cell-type sensor construction.

3.3.3 Electrode preparation

Three kinds of catalysts (stainless steel, copper, and nickel) were studied for ethanol sensing, where stainless steel was always the base metal. For copper and nickel studies, they were electroplated on the stainless steel. Before electroplating the porous metal sheet, it was cleaned thoroughly with a detergent, deionized (DI) water, and acetone in an ultrasound bath for 5 min. Then, the sheet was anodically electro-cleaned by placing the lead cathode in 25% H_2SO_4 for 5 min. below room temperature, with a current density of 13.94 Am^{-2}. After a thorough wash in DI-water, the stainless-steel sheet was cleaned at room temperature for 45s with a solution of HCl, H_2SO_4 and DI-water with a volumetric ratio of 1:10:1000. Afterward, to improve the metal-metal adhesion, "Wood's Nickel Strike" [194 195] was performed to deposit a thin layer of nickel or copper onto the stainless-steel sheet. For nickel electroplating, "Watt's deposition method" was employed at 50 ˚C and a 0.2 A and 2 V rating [195]. The electrolyte for Wood's nickel strike includes HCl and anhydrous nickel chloride. The electrolyte for Watt's deposition method includes nickel sulfamate, nickel chloride, and boric acid. The nickel-deposited sheets were rinsed in DI-water and baked at 190 ˚C for 2h. For copper electroplating copper sulphate solution was employed for the copper deposition. Copper electroplated sheets were air dried at room temperature.

3.3.4 Characterization of the electrodes

X-ray diffraction (XRD) analysis was used to understand the fingerprint characterization and the phase identification of the crystalline structure of the catalysts on

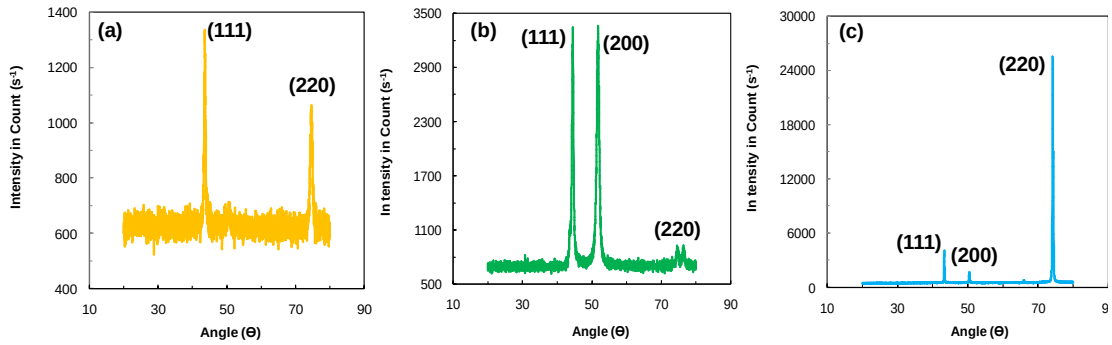

Figure 3-3: XRD profile of (a) stainless steel, (b) nickel and (c) copper

the electrode [193 196 197]. As shown in Figures 3-3a-3-3c, for stainless steel, two strong peaks were observed at the angles of 43.62˚ and 74.64˚. These two peaks represent SS (111) and SS (220) structures, respectively. A small peak was also found at 50.48˚. From the miller indices, it was assured that the stainless-steel sample represents the SS-304 type [193], and its structure is in a single-phase face-centered cubic (FCC) pattern. For the nickel sample, three strong peaks were obtained at 44.5˚, 51.78˚, and 78.7˚, which correspond to Ni (111), Ni (200), and Ni (220), respectively [196]. This result confirms that the electroplating of nickel was well crystalline. For copper sample, the peaks were found at 43.38˚, 50.54˚, and 74.14˚, which correspond to the Bragg reflections of Cu (111), Cu (200), and Cu (220), respectively. Comparing this data with the Joint Committee on Powder Diffraction Standards (JSPDS) data sheet confirmed that the specimen is face-centered cubic (FCC) copper crystalline [197].

3.3.5 Nickel as a catalyst for ethanol sensing

The performance of three different sensors made of copper, stainless steel and nickel was evaluated by the amperometric response (Figure 3-4a – 3-4c). The setup

includes the fuel cell sensor in a chamber where 10 µl of 15.8 M pure ethanol was applied on the 0.2 cm^2 opening of the working electrode. Hence, the contact area remained the same for all three sensors. The counter electrode had an opening for the oxygen reduction reaction. All the sensors showed an ethanol response within 2s. However, the steady-state signals were achieved after 700s by the stainless-steel sensor and 2s by nickel. Though copper showed a good current response (20 µA) initially, there was no steady-state response. This instability of the copper can be attributed to the quick and irreversible oxidation reaction of the copper on the cathode. The steady-state current obtained from stainless steel and nickel sensors were 0.2 µA and 60 µA, respectively. The amperometric results revealed that nickel provided a 300 times higher current than the stainless steel (Figure 3-4). Moreover, nickel showed a more stable response among these three catalysts, whereas copper showed poor stability. Therefore, for the following studies, nickel was selected as the catalyst material.

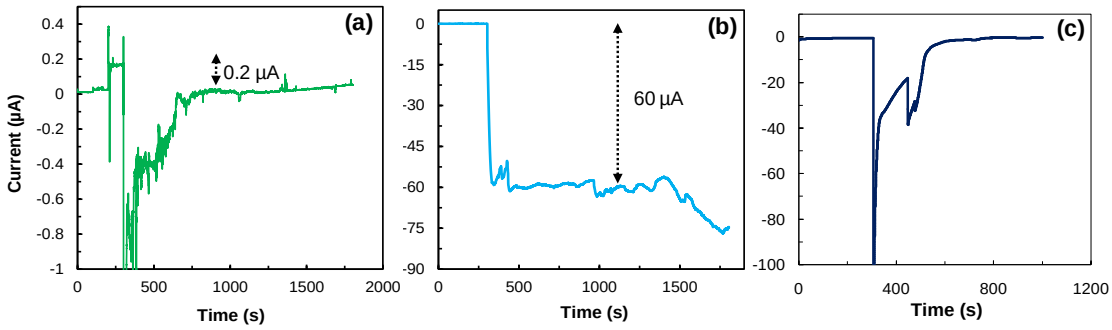

Figure 3-4: Amperometric responses for the 15.8M pure ethanol for various catalysts: (a) stainless steel, (b) nickel and (c) copper

3.4 Fabrication of the Monel-based fuel cell sensor

3.4.1 Materials and apparatus

Monel (Nickel 400 containing minimum 63% Nickel and 28% Copper) wire mesh from TWP Inc. has been employed as the electrode material. Its noncorrosive nature prevents oxidation and provides signal stability compared with pure copper or nickel. Laser cutting of the Monel sheet was executed at SBC Industries in Miami to provide specific shapes and dimensions of the all electrodes. Nafion perfluorinated 424, reinforced with PTFE fibers (thickness 0.03 cm), from Sigma Aldrich was used as proton exchange membrane (PEM).

3.4.2 Design and fabrication of the micro fuel cell

The dimensions of the working electrode (WE), counter electrode (CE), and reference electrode (RE) (1 cm x 1 cm x 0.025 cm) of the micro-fuel cell were considered, respectively (the cross-sectional and top views are shown in figure 3-5a). The electrolyte membrane, Nafion (2 cm x 1 cm x 0.02 cm), was sandwiched between the electrodes to form the MEA. The overall area of the CE electrode was designed to be substantially larger than the WE and RE, as mentioned earlier. In contrast, the area of the RE was designed to contain the smallest surface area, and it was placed maintaining a specific distance from the CE on the same side of the membrane. This distance (L= 0.55 cm) was kept greater than three times ($L/\delta > 3$) the membrane thickness (δ = 0.02 cm) to avoid the asymmetrical current distribution and potential variation on WE due to the edging effect [198]. The WE was placed on the opposite side of the CE in such a way that the maximum

area of the WE overlapped with that of CE. The Monel sheet was cut according to the design that was created at SolidWorks CAD with a tool, as shown in Figure 3-5b. After laser cutting, the micro-porous wire mesh of Monel was cleaned thoroughly with detergent, DI water, and isopropanol (IPA) in an ultrasound bath for 5 min.

An aluminum mold was designed using the SolidWorks CAD tool for hot pressing, shown in Figure 3-5c and 3-5d. The mold was designed in the 7x6 matrix so that 42 PEMFC sensors could be fabricated simultaneously. The sandwich structure of the three-electrode fuel cell was achieved by placing the strips of the Monel electrode pieces (Figure 3-5b) with the membrane inside the mold according to design. Subsequently, the MEA was hot pressed at 75 ˚C and 2500 psi for 10 min. by the hydraulic press (model 2100 from PHI),

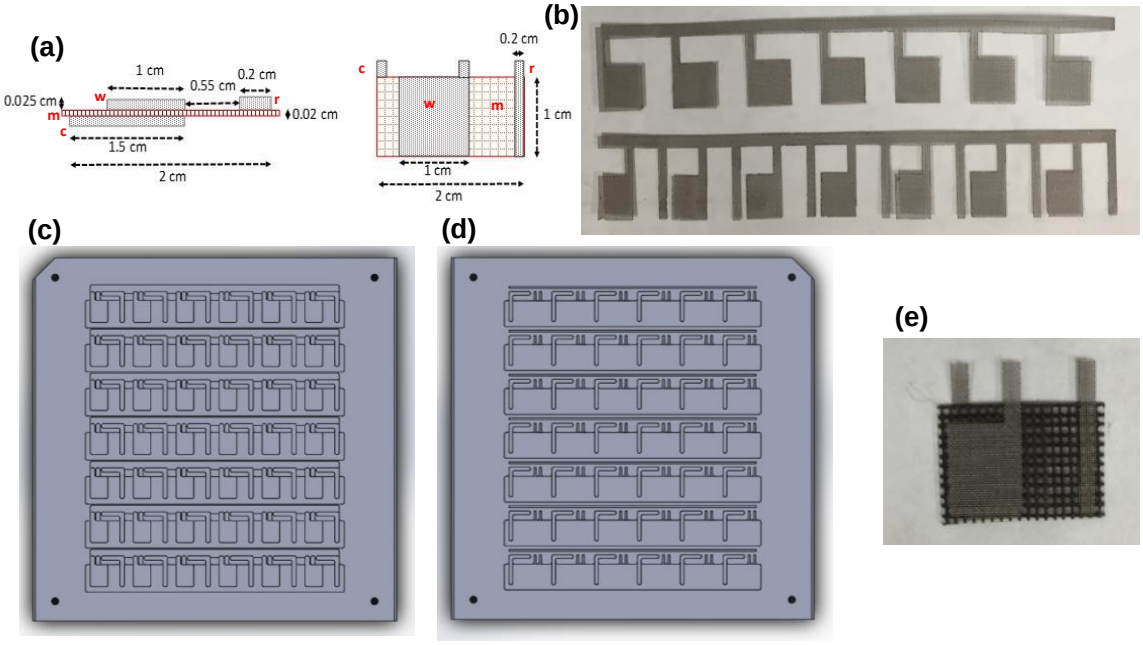

Figure 3-5: (a) design of the three-electrode fuel cell sensor; (b) the strips of the Monel electrodes after laser cutting; the CAD design of the aluminum-made mold (c) the bottom part and (d) the top part (e) the three-electrode fuel cell sensor after fabrication

like that which was mentioned in section 3.3.2. The fabricated arrays of fuel cells were kept at room temperature for 1-2 hrs. inside the mold, and it was observed that the electrodes properly adhered to the membrane through the thermal cycling process [199, 200]. Finally, the fuel cell sensor was cut from the strips using a guillotine.

3.5 The working mechanism of the PEM fuel cell

The hydrophilic sulfonic acid group governs the kinetics of proton transfer, where the transportation mechanism can be explained by the widely accepted cluster channel model proposed by Hsu and Gierke [201]. In this model, the sulfonated acid groups form water-filled clusters over which the protons are transported, as shown in Fig 3-6a and 3-6b. From this model, it can be inferred that only under the conditions of an optimum hydration level can Nafion transport protons across. The conductivity of these ions is proportionally related to relative humidity (RH) in the environment. A relationship of proton conductivity vs. % of RH is plotted in Figure 3-6c. This plot supports our claim that a change in RH leads to a linear change in ionic conductivity. Proton conductivity (σ) in

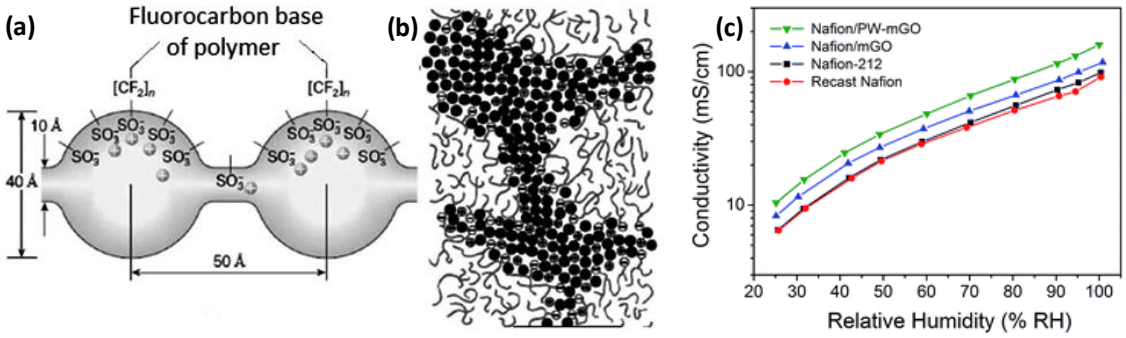

Figure 3-6: (a) The cluster channel model with the (b) Cluster [202], (c) %RH vs. conductivity [202]

polyelectrolytes also depends on temperature ($\sigma T = \sigma_0 e^{\frac{E_a}{kT}}$) and the hydrophilic volume fraction, $\sigma \sim (\varphi - \varphi_c)^2$ [202]. This volume fraction has also been seen to share a quadratic relation with the diffusion of water molecules, $D_w \sim \varphi^2$ [202]. H_2O diffusion flux (J_{H_2O}) is generally controlled by the electro-osmotic drag (EOD), diffusion and applied electric force, where J_{H_2O} is assumed to be a linear superposition of EOD and diffusion [203]:

$$J_{H_2O} = \xi\sigma + c_w D_w \frac{da_w}{dx} \quad (1)$$

where, $\xi \left(= F \frac{dJ_{H_2O}}{d\sigma}\right)$ is the EOD coefficient, F is the Faraday constant, σ is current density, c_w is the concentration of water in mol/cm^3, D_w is the diffusivity of water in cm^2 s^{-1}, and $a_w \left(= \frac{P_w}{P_w^0}\right)$ is water activity due to partial pressure of the vapor phase of water molecules. The diffusion of H^+ ions is governed by the Grotthuss mechanism, *en masse* diffusion, and surface diffusion, where the relationship among them for a single pore is given by the following equation [204]:

$$\sigma_p = \sigma_{H^+}^{\Sigma} + \sigma_{H^+}^{G} + \sigma_{H^+}^{E} \quad (2)$$

In the above equation, $\sigma_{H^+}^{\Sigma}, \sigma_{H^+}^{E}$, and $\sigma_{H^+}^{G}$ represent H^+ ion conductivity for the surface, *en masse*, and Grotthuss diffusion. Combining equation (2) with Nernst-Einstein equation, the overall membrane conductivity, σ_{H^+} is found, as follows [204]:

$$\sigma_{H^+} = \frac{\varepsilon_i}{\tau} \left[\frac{F^2}{RT}\left(D_{H^+}^{\Sigma} C_{H^+}^{\Sigma} + D_{H^+}^{G} C_{H^+}^{C} + \frac{D_{H^+}^{W}}{1+\delta_c} C_{H^+}\right)\right] \quad (3)$$

where ε_i is the molar fraction of the water per acidic chain, τ is the tortuosity factor of the pore, $C_{H^+}^{\Sigma}$ and C_{H^+} are the surface and bulk membrane distribution of the proton concentration, respectively, and $D_{H^+}^{\Sigma}$, $D_{H^+}^{G}$ and $D_{H^+}^{W}$ are the surface, *en masse*, and Stefan-Maxwell diffusion coefficients, of the hydronium ion, respectively.

In a PEM galvanic cell, H^+ ions are contributed by the fuel, for example, ethanol [205 206]. These ions are transferred through Nafion, and the flow of electrons is regulated through the circuit. The operation of a PEM galvanic cell depends primarily on (i) the redox reaction at the electrode surface, (ii) the PEM's hydration and its ability to transport protons from the anode to the cathode, and (iii) the catalyst's ability to enhance the redox reaction. In Figure 3-7, the reaction mechanism is depicted for transdermal ethanol detection by the PEMFC sensor. Here, the target compound ethanol is exposed (oxidized), and ambient oxygen is reduced at the cathode [207]. The electromotive force in this PEM galvanic cell is caused by the standard potential (E_0), given by the Nernst equation (1).

$$E = E_0 - \frac{\mathrm{RT}}{nF} ln\, Q_r \qquad (4)$$

where, E is the half-cell potential, n is number of electrons transferred, F is the Faraday constant, R is the molar gas constant, T is temperature and Q_r is the reaction quotient. The standard potential drives the faradic current in the presence of the target

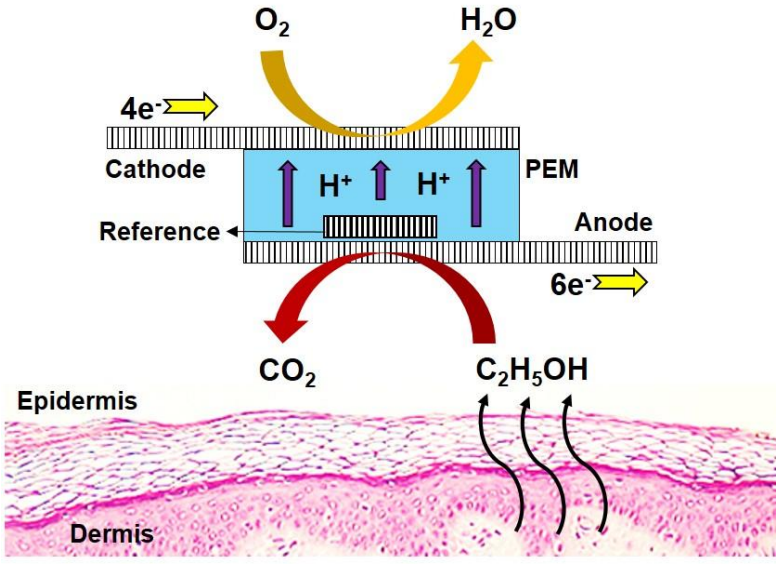

Figure 3-7: The working mechanism of PEM galvanic cell

analyte. This generated current depends on: the open circuit potential (OCP) of the reactions, applied potential across the electrodes, and the rate of the reaction.

CHAPTER IV

CALIBRATION OF THE FUEL CELL SENSING PLATFORM FOR VOC SENSING IN A TWO-ANALYTE SYSTEM

This chapter is divided into three major sections. The first section presents the development of a nickel-based PEMFC sensing platform for the detection of VOC(s), such as alcohol. The second section focuses on the detection mechanism of the alcohol by the fuel cell sensor and its improvement of calibration by eliminating the noise of major interfering compounds, such as humidity. Finally, the third section explores the prospect of this wearable alcohol-sensing device.

4.1 Background of wearable alcohol measurement systems

A continuous wearable alcohol measurement system has been sought in numerous fields, ranging from law enforcement to clinical monitoring to safety systems [208 209]. Breath alcohol (BA) measurement devices are used by law enforcement agencies for the random monitoring of drivers to determine whether they are driving under influence of alcohol [10 210 211 212]. Since law enforcement involves measuring the BA content of a random population at one point in time, breath analyzers are adequate. However, in a clinical application focused on understanding the consumption and metabolism of alcohol, measurements are required over extended periods, ideally starting from 30 min. before consumption and extending to 8h. after the last drink. Given that alcohol is generally consumed in the evenings and the subject will likely sleep following his ingestion of alcohol, breath analyzer, a continuous alcohol sensor, is preferred. The simplest approach

to continuous monitoring of alcohol is a wearable sensor that uses alcohol vapors emanating from the skin and secreted with sweat [213 214 215].

After alcohol ingestion, a very small proportion (1% of overall alcohol consumption) is excreted with sweat from the exocrine sweat gland or in a diffusive manner [162]. The sweat is mostly composed of water (~99% of overall volume), with a small amount of nitrogenous compounds, metal and nonmetal ions, metabolites, xenobiotics, organic volatile compounds, and so on [216]. Hence, the elimination of cross selectivity with different compounds, especially with the water content of sweat or atmospheric humidity, is challenging for any transdermal alcohol sensors. The reaction kinetics [217] and maximum power density [218] of the PEMFC sensor are directly dependent on relative humidity. In the electrochemical sensing, therefore, humidity has an adverse impact on the calibration of the sensors. Like humidity, other volatile compounds released from the skin, such as aldehydes and ketones [219], will undergo a reaction in the anode, creating an interference signal. Only a selective and accurate alcohol measurement device would be the possible solution to overcome this issue. This can be achieved in two ways: first, to develop a highly selective sensor that can offer an accurate signal for only alcohol, or second, electrically eliminate the noise signals following a robust electrochemical technique.

Wearable transdermal alcohol measurement devices have been built before, e.g. “GinerWrisTAS” [205]. However, this device did not have a data acquisition system and required a humid chamber for measurements. Others [205] integrated the data acquisition system and incorporated PEM as an electrolyte. However, these sensors suffered from false positive readings due to the presence of VOCs, the lack of selectivity, and the need for

frequent manual calibrations. Both fuel cell/electrochemical breathalyzers and wearable devices measure interactions between the sensor and VOCs, such as acetone, acetophenone, isoprene, etc. [220]. The interactions lead to a change in potential and generate a signal. When these devices are used to for the measurement of alcohol, the VOCs trigger false positives.

To address the needs of the target users, a complete wearable system needs to be developed. Such a system should be able to recalibrate and reference itself to its environment, minimizing the effect of VOCs, thus enabling long-term quantitative monitoring. The platform needs to provide real-time statistical analysis for different vapor footprints, including alcohol, so it can be calibrated to the needs of the user. Such systems should also be low power to ensure long usage life between charges. This paper presents such a sensing system that can communicate with external devices through Bluetooth for longitudinal data analysis to ensure functionality. Finally, the sensor was packaged into a wristwatch format.

4.2 Experimental

4.2.1 Materials and Methods

Materials for PEMFC sensor fabrication were discussed in section 3.3.

The MICRO5 PID sensor was purchased from BW Technologies. Potentiostat (CHI 1230B with MC470) was purchased from CH instruments Inc. LMP91000 miniaturized potentiostat with analog front end (AFE), a 16-bit ultra-low power microcontroller (MSP430F5529LP), RN42 Bluetooth chip and the LP2591 power management system were purchased from Texas Instruments (TI). The MCP72831 charge controller, a 12-bit

digital-to-analog converter (ADC) with integrated electrically erasable programmable read-only memory (EEPROM), and an I2C compatible serial interface from Microchip were purchased.

The fabricated PEMFC sensor (as mentioned in section 3.3) was interfaced with the AFE of the LMP91000 on a wearable platform. The WE, RE, and CE of the sensor were connected to the corresponding pins of the AFE. The AFE was linked to the microcontroller via an inter-integrated circuit (I2C) interface. The Bluetooth module was connected via a universal asynchronous receiver/transmitter (UART) peripheral of the MSP430. The liquid

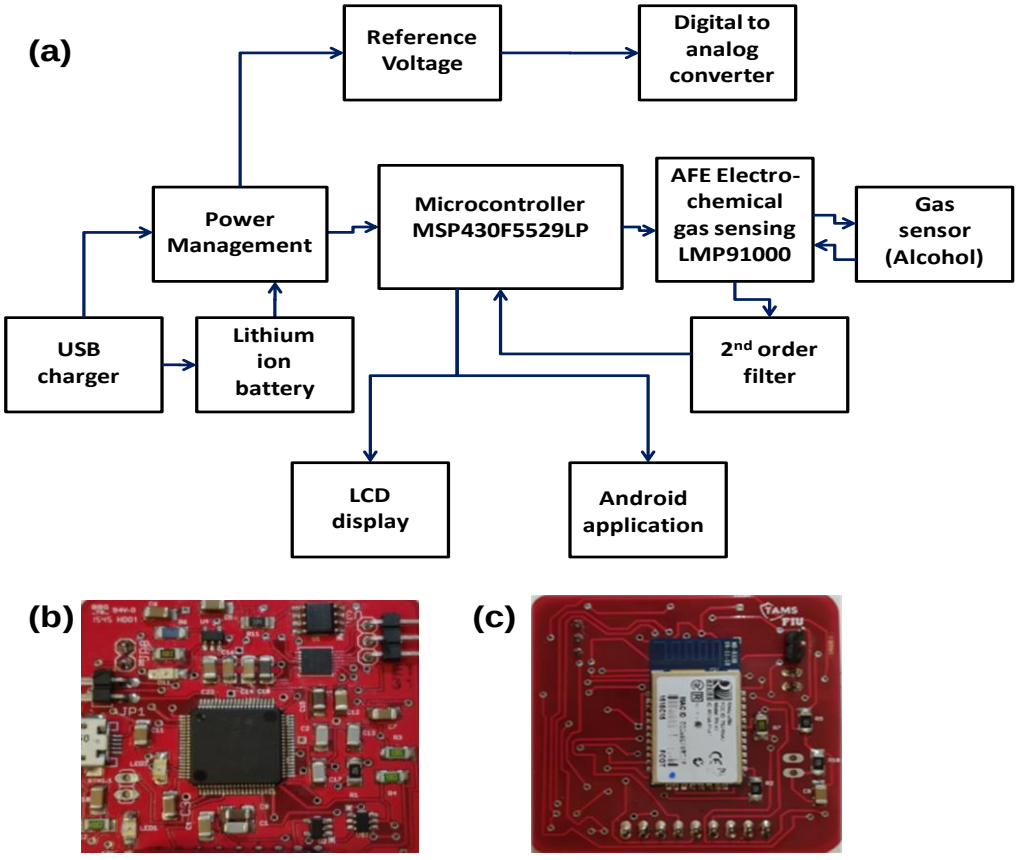

Figure 4-1: (a) Block diagram and schematic of peripheral connections in the alcohol monitoring device, (b) the top and (c) bottom layer of the PCB board, where the top layer consists of a LMP91000, microprocessor and other integrated electronic components, and the bottom layer consist of Bluetooth component

crystal display (LCD) used the serial peripheral interface (SPI) of the MSP430. The connections and their functions are discussed in the results and discussion. The peripheral connection is depicted in the block diagram, as shown in Figure 4-1a. The printed circuit board (PCB) was manufactured on a two-layer board using a 1.6 mm-thick FR-4 substrate, with 28.35 g copper and an area of 6.45 cm^2. All the electronic components, including the microcontroller, AFE, power management system, and associated circuitry, were mounted on the top layer, as shown in Figure 4-1b. The Bluetooth chip was solely mounted on the bottom layer Bluetooth (Figure 4-1c).

Standard solutions of ethanol and vapor were calibrated using the MICRO5 PID sensor. OCP and amperometric studies of the fuel cell were with the commercial potentiostat. Ethanol vapor was generated by bubbling a constant flow of air through a 15.8M-ethanol solution. Ethanol vapor was passed through a custom 3D printed chamber (~0.7 cm^3) containing a standard PID sensor or the WE of developed sensor for measurements. The chamber was designed in such a way that the CE was exposed to the atmosphere.

4.3 Results and Discussions

4.3.1 The Electrochemical Mechanism of the Ethanol Fuel Cell Sensor

The operation of the PEM fuel cell sensor depends primarily on (i) the redox reaction at the anode and cathode surface, (ii) the PEM's hydration and its ability to transport protons from the anode to the cathode, and (iii) the catalyst's ability to enhance the redox reaction. The redox reactions of the ethanol fuel cell can be represented by

equations (1), (2), and Figure 4-2a. The overall fuel cell reaction can be represented by equation (3) [221]:

$$C_2H_5OH + 3H_2O \rightarrow 12H^+ + 12e^- + 2CO_2 \quad (E^0 = 0.085V) \quad (1)$$

$$3O_2 + 12H^+ + 12e^- \rightarrow 6H_2O \quad (E^0 = 1.23V) \quad (2)$$

$$C_2H_5OH + 3O_2 \rightarrow 2CO_2 + 3H_2O \quad (E^0 = 1.145V) \quad (3)$$

In this reaction, protons are exchanged from the anode to the cathode through the PEM, and the electrons flow through the internal circuit. The E_0 values given in equations (1) and (2) are the thermodynamic standard potentials vs. standard hydrogen electrode (SHE), and the E_0 value in equation (3) is the equilibrium potential difference, which represents 12 electrons per ethanol molecule. However, the thermodynamic values are practically of little use, as practical systems don't operate under reversible conditions. To obtain the characteristics of the constructed three-electrode PEMFC sensor, the OCP technique (time vs. voltage) was used. In these studies, to enhance oxygen reduction and

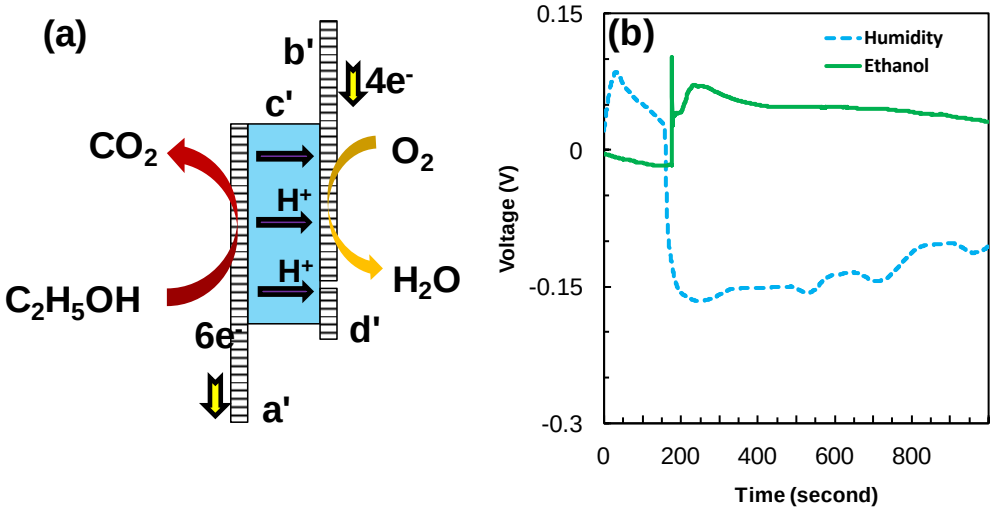

Figure 4-2: Schematic of ethanol oxidation and oxygen reduction in a fuel cell sensor, where a', b', c', and d' represent WE, CE, PEM and RE, respectively. (b) OCP of a fuel cell sensor in the presence (continuous green) and absence (dashed blue) of 95% ethanol in 100% humidity.

ethanol oxidation, Ni was used as a catalyst [28 221]. The effect of humidity on H^+ ion transport was minimized by treating each sensor in a humid chamber for 30 min. at room temperature, as it is established that the rate and amount of proton exchange depend on the water content of the PEM [222]. The OCP measurements were taken over a period of 1,000s in a closed chamber containing the fuel cell sensor. Even though the steady-state potential of the sensor was attained within 5s, t = 100s was chosen to introduce the ethanol to illustrate the stability of the baseline. The response time of the sensor can be seen to be less than 2s (Figure 4-2b). The same figure shows that the OCP of ethanol oxidation (100% humid condition) was 0.07 V. In our sensor, we consider thermodynamic standard potential instead of equilibrium potential difference, as the fuel cell sensor is a three-electrode system and measurements were half-cell measurements. According to the Nernst equation, the OCP of ethanol should be much higher than the thermodynamic standard potential of ethanol (0.085V). This low ethanol OCP value is due to the mixed potential generated because of both ethanol and humidity.

The experimental results in Figure 4-2b also revealed that there was a ~-0.2 V deviation in OCP for 100% humidity (absence of ethanol) compared to the OCP in the presence of ethanol. This deviation varies with the percent change in humidity at the rate of 2.7 mV for each percentage decrease in humidity (Figure 4-3). The humidity level varies inconsistently in practical conditions, and the exposure to various humidity percentages revealed that the reference value of the sensors' OCP signal oscillates for the sample size, n = 5. Therefore, deriving a relationship between humidity and the ethanol, the OCP signal generation for calibration was not possible based on empirical results. Hence, quantifying ethanol based on the OCP technique alone was inaccurate, even though significant signals

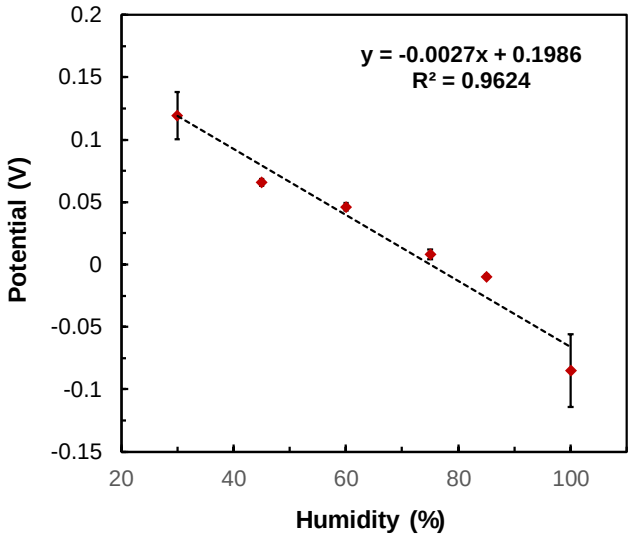

Figure 4-3: Plot representing the effect of humidity (%) on the OCP of the micro-PEMFC sensor in the absence of ethanol, where there was a 2.7 mV change in OCP for each percentage decrease in humidity for n = 5.

were measured for ethanol in OCP. However, the OCP signal variation between ethanol and the humidity (-0.2 V) provided a significant opportunity to design a multimodal method to eliminate interference. Like humidity, any organic volatile compounds capable of oxidizing on the anode has its own OCP signature, which is an important characteristic supporting the selective detection of desired compound in a given binary system.

4.3.2 A Method to Eliminate the Interfering Signal

Selectivity is the biggest challenge in the successful construction of any fuel cell sensor. In the diffusion control process, OCP, due to any given reaction, is independent of its concentration. However, in the case of low concentration and low volume measurements, the rate of the reaction, rate of diffusion, and rate of evaporation are the limiting parameters. If the concentration of the interfering compound is much higher than

the ethanol, the sensors' accuracy will be low. This is because, as discussed above, the experimental potential of each compound varies due to the mixed potential, which in turn affects the current generated by the fuel cell. To improve accuracy, a multimodal method containing both OCP and the amperometric techniques was employed for subsequent measurements.

During the redox reaction, the current flow between the electrodes can be measured using the amperometric method as the faradaic current. This generated current depends on: the formal potential of the reactions, the applied potential across the electrodes, and the rate of the redox reaction. For example, the amperometric measurement of ethanol at a fixed potential (-0.05V) in the presence of high humidity given in Figure 4-4a revealed that there is a response for not only ethanol but the humidity as well. The same figure showed that if the applied potential was lower than the OCP of ethanol, it resulted in a negative current response, and vice versa for the humidity. The response depended on the difference (ΔV) between OCP and the applied potential, resulting in a variation in the output current. This showed that the rate of faradaic reactions on the electrode surface could be manipulated using external voltage. As a step toward eliminating humidity interference signals, a signal due to humidity was taken as an example for the following studies. A similar method can be applied for eliminating the signals of all other organic, volatile compounds. However, the method reported here is only applicable for a binary chemical system and has not been validated for multiple interfering compounds.

The selectivity of ethanol in the presence of humidity was achieved through the following steps: (i) identifying the OCP in the presence of humidity, and (ii) applying the obtained OCP value across the WE and RE, and measuring the current flow between the

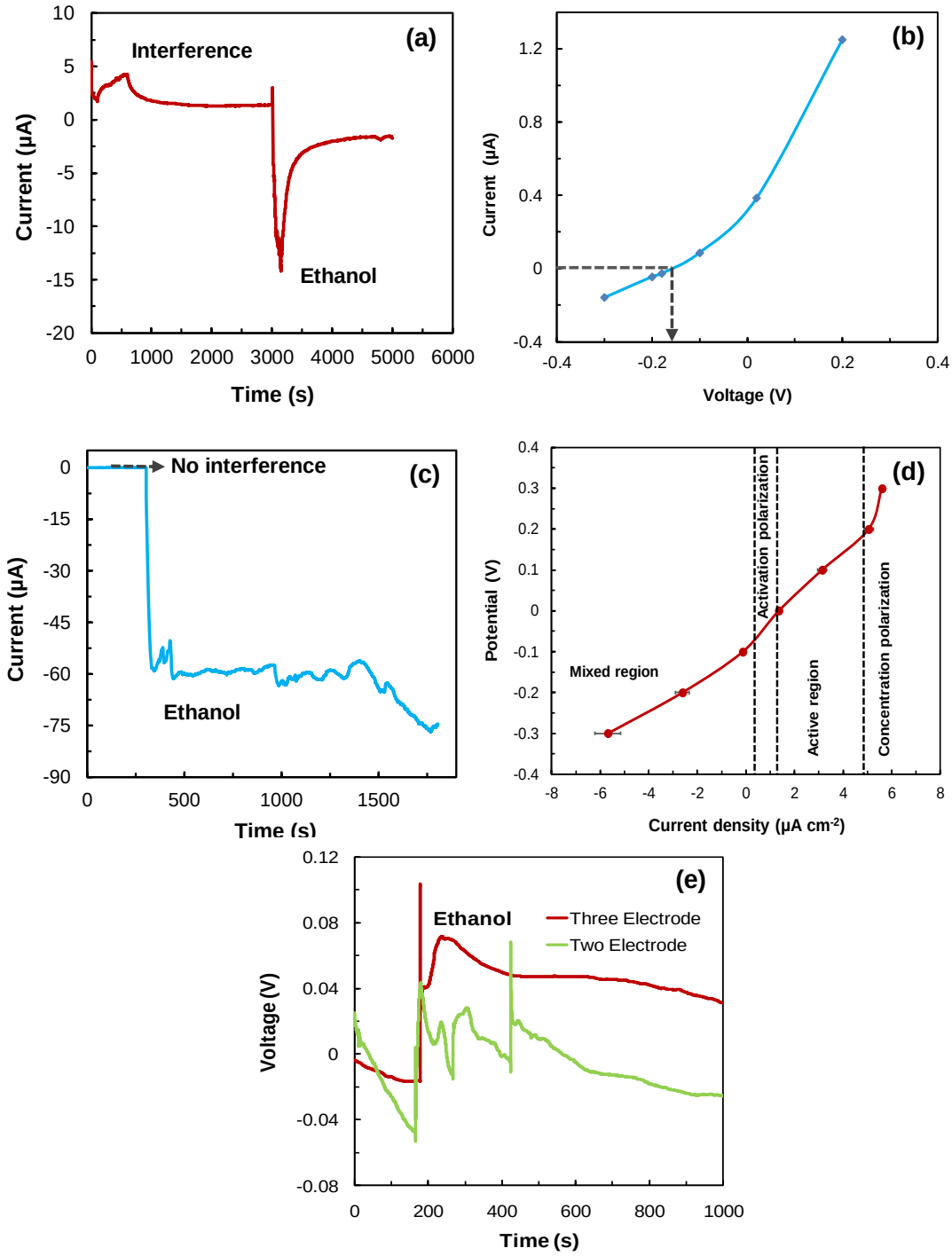

Figure 4-4: (a) Amperometric plot showing humidity and ethanol signals, (b) calibration plot of current vs. voltage scan in presence of humidity showing the voltage at 0A, (c) amperometric studies after calibration showing only the ethanol signal, where the interfering signal was eliminated, (d) anodic polarization curves of the micro-fuel cell sensor in the presence of 50 ppm of ethanol and 46% of humidity. (e) OCP signature comparison of ethanol in two and three-electrode systems.

CE and WE. In this process, the current signal due to humidity was eliminated, and the current flow due to ethanol oxidation for that potential was recorded. The experiments with humidity (> 90%) showed that the OCP of the fuel cell sensor varied between -0.05 V to – 0.2 V. By keeping the potential exactly at the experimental potential (E_{cell}) at any given humidity level (in the absence of ethanol), the current flow due to humidity was eliminated.

The identification of the E_{cell} at any given humidity was carried out by a series of amperometric studies, where various potentials were applied across the electrodes and the current was measured (Figure 4-4b). From the applied potential vs. current plot, the exact E_{cell} at which the current falls to zero was identified for that humidity. Even though the steady-state OCP measurements can be used to measure this E_{cell} value, the amperometric method was used to find the E_{cell} to significantly improve the accuracy. Attaining OCP, the steady-state value would vary depending on the environment and the need for prolonged scans in real-time calibrations. The amperometric results after calibration (Figure 4-4c) show the ethanol signal only, and the signal interference due to humidity was eliminated.

In a separate study, the anodic polarization of the micro-fuel cell (Figure 4-4d) showed a linear increase in the current, from -0.3 V to -0.08 V, indicating the mixed potential signal of both humidity and ethanol. In the same curve, there was a change in slope in the region of -0.08 V to 0 V, indicating the activation polarization for ethanol oxidation. The active region of the ethanol oxidation was in the range of -0.8 V to 0.2 V. The region greater than 0.2 V was the concentration polarization, where the reaction is diffusion-limited.

4.3.3 Improving the Stability of the OCP Signature

To achieve the chemical specificity, it was imperative that the sensor had a precise E_{cell} for each chemical compound in any given electrochemical system. The current fuel cell sensors in the market are made of a two-electrode set-up; maintaining a precise E_{cell} is generally not possible with a two-electrode system due to the potential drop across the cell because of electrolyte resistance and the possible polarization of the CE. It is well known that during amperometric measurements, the electrodes are polarized, which in turn perturbs the electrochemical system. However, a precise E_{cell} can be maintained in this process using a three-electrode system, in which the potential of the WE is measured relative to the RE. Further, due to the high impedance between the WE and RE, the current passes between the WE and CE, avoiding the polarization of the RE. The electromotive force in a three-electrode system caused by the standard potential (E_0) is given as the Nernst equation (4).

$$E_0 = -\Delta G_0/nF \qquad (4)$$

where ΔG_0, n, and F are respectively Gibb's free energy, the number of electrons, and the Faraday constant. The stability of the E_{cell} was tested using the OCP technique, and the two and three-electrode systems were compared, as seen in Figure 4-4e. The results showed that after the addition of ethanol, there were erratic changes in the OCP of the two-electrode fuel cell sensor, while the three-electrode configuration resulted in a stable OCP of the three-electrode system.

4.3.4 Algorithm for the Sensor Auto-Calibration

Based on the experimental observations reported in section 3.2, a flow chart (Figure 4-5) was developed for implementing an algorithm that would result in the chip-potentiostat having auto-calibration ability and selectivity to ethanol in highly humid conditions. The nullification of the current signal produced by humidity was achieved by the two following functions:

Function 1: auto-calibrate the fuel cell sensor at certain intervals (which depend on the steady-state response of the nickel catalyst).

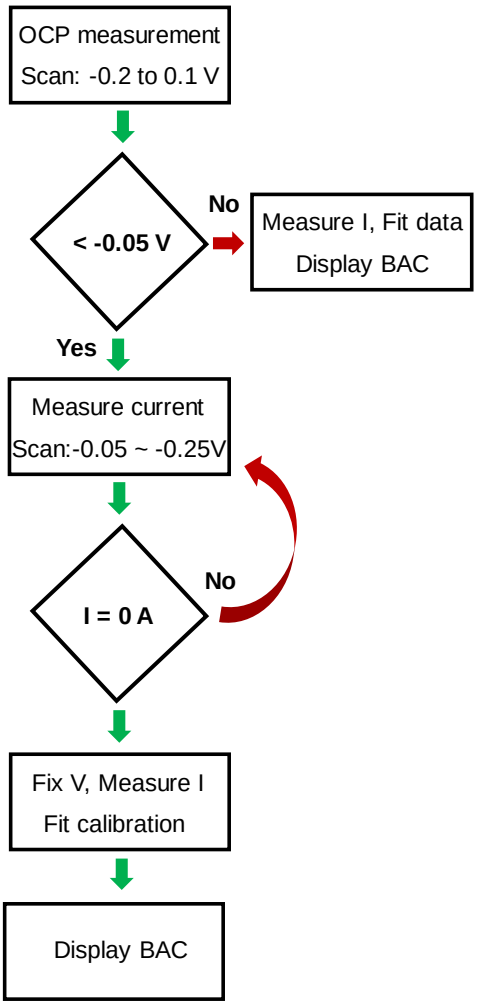

Figure 4-5: Flow chart representing steps involved in selective ethanol detection.

Function 2: measure ethanol using the amperometric measurement.

The calibration (1st function) was necessary to know the humidity signal and nullify this in the second function. The 1st function involved OCP and amperometric measurements; the 2nd function involved amperometric measurements. In the 1st function, if the value was lower than the threshold OCP, it indicated no ethanol presence, and the system proceeded to amperometric measurements. In this step, the E_{cell} for 0 A was identified by measuring the current across the electrodes while scanning the potential. The obtained E_{cell} value was stored in the system. This stored value was the bias voltage for amperometric measurements in the 2nd function, where the current was measured and fitted against a pre-determined calibration curve. In the device memory, there will be multiple pre-determined calibration curves stored for each biasing voltage. These curves were used, as the current signal magnitude in the 2nd function depends on the biasing potential. The final step is to display the BAC from the calibration curve fitting. This process nullifies the interfering signal in any given environment.

4.3.5 The Configuration of the Analog Front-End Alcohol-Sensing Device

A schematic of the potentiostat is given in Figure 4-6a. The arrangement of the circuit is that of a non-inverting operational amplifier. The voltage supplied by source E was closely followed by the voltage between the RE and WE terminals. Z1 and Z2 are the characteristic impedances of the fuel cell between the respective terminals. Any change in impedance due to ethanol coming in contact with the WE was reflected by the change in current I_c (current at CE), as show in Figure 4-2a. As described in previous sections, the

impedance at the negative terminal of the amplifier was very high, which made the current flowing through the RE negligible.

The LMP91000 can be configured to perform different types of electro-analytical techniques. The detection method used in the system was amperometric. Referring to Figure 4-6b, amplifier A1 is the control amplifier that implements the potentiostat circuit. The variable bias block of the LMP was used to provide a user configured potential across positive and negative terminals of A1. This potential was held constant between the reference and working terminals by the potentiostat. The transition from minimal current flow to voltage was made available by the trans-impedance amplifier (TIA), whose forward voltage gain is dependent upon on a feedback resistor R_{tia}. It can be connected either internally or externally to the feedback path of the TIA, as depicted in the internal block diagram of the AFE of LMP91000 in Figure 4-6b. It converts the current flowing from the CE and WE to a proportional voltage. Its output is connected to the V_{out} pin (this pin can be toggled to give output of the temperature sensor of the LMP) and the C2 pin.

The LMP was configured via the microcontroller to perform three-electrode amperometry following the functional block diagram sketched in Figure 4-6b. The microcontroller was connected to the LMP via the I2C interface, as depicted in Figure 4-1a and 4-6b. The serial clock line and serial data bus line on the I2C bus were connected to 3.3 V_{dc} from the system power management unit, with one external pull-up resistor each. The schematic representation in Figure 4-6b was derived for the 3-lead amperometric cells in the potentiostat configuration. The output voltage available at the V_{out} pin of the LMP91000 was then routed to the microcontroller's general-purpose input/output (GPIO),

where it was conditioned by an internal analog-to-digital converter (ADC) for interpretation. The TIA gain is adjusted to provide a voltage proportional to cell current. It can be internally programmed via software for a range of 2.5 kΩ $\leq R_{tia} \leq$350 kΩ and externally configured, as required.

The internal feedback resistor was optimized for an optimal TIA amplifier gain using a value of R_{tia} = 120kΩ. This provided a large enough signal gain to manipulate the

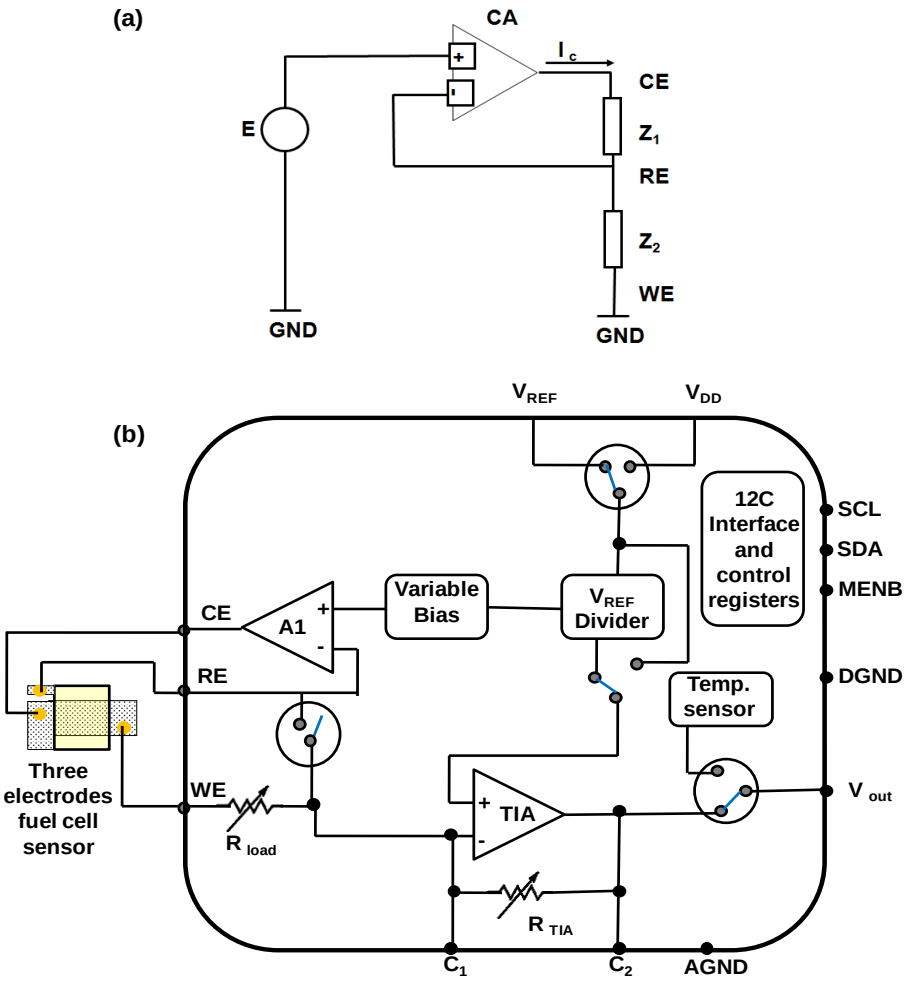

Figure 4-6: (a) Block diagram of a simple potentiostat, where CA is the control amplifier, Ic is the current at the counter electrode, Z1 is the impedance across the counter and reference electrode, Z2 is the impedance across the reference and working electrode, and E is a voltage source. (b) Functional block diagram of LMP91000 AFE with the fuel cell sensor.

data and provided sufficient headroom for voltage swings because of changes in alcohol concentration. The module-enable (MENB) was tied to ground to signal a communication-ready status to the microcontroller. In the case of multiple alcohol sensors, the MENB line of each AFE sensing device on the I2C bus can be individually toggled through to extract data from each sensor. The voltage reference (V_{REF}) to the AFE sensing device was externally provided by the digital-to-analog converter (MCP4724), and was adjustable through software. It can meet a wide range of supply voltages to the LMP91000 and specify bias voltages with accuracy. The load resistor was set to its lowest internal resistance value of R_{load} = 100 Ω to draw the maximum current from the sensor and subsequently become amplified by the TIA.

4.3.6 Microcontroller Operation and the Alcohol Concentration Measurement Technique

MSP430F5529LP was chosen due to its small LQFP-80 pin packaging size and low power mode settings that allow power consumption down to 1.4 µA in LPM3, a low operating voltage range of $1.8\,V_{DC} \leq V_{Batt} \leq 3.7\,V_{DC}$, and portability to other microprocessing units if desired due to the simplicity of the C programming language. Features that made this microcontroller attractive for our application were its ability to store 128 kB of non-volatile flash memory and 8 kB of RAM, allowing the software to execute during power-on and reset events, and a 12-bit ADC that was used to measure the analog output of the LMP.

The MCU has the capability to communicate via SPI, UART, and I^2C. The alcohol sensing platform uses I^2C to communicate with the LMP91000 and MCP4724, UART to

communicate with the RN-42 Bluetooth module, and SPI to communicate with the monochrome LCD. The present configuration for the MCU was shown in Figure 4-1b. In the figure, the MCU can be programmed and debugged on-chip and on a minimally system-invasive procedure simply by connecting two Spy-Bi-Wire emulator cables. The external circuitry, shown in Figure 4-1b, consists of bypass capacitors and ground connections required for proper MCU operation. This configuration was derived from a device-specific datasheet and user guide. The algorithm for interpreting sensor data was adapted from [223]; under this configuration, two additional cables were routed from the C_1 and C_2 pins to the GPIO pins. The data from C1 and C2 consists of the analog output voltage $V_{out,}$ and this voltage presents at the inverting input of the TIA, which is directly connected to the electrodes of the sensor, and is the same voltage at the non-inverting input of the WE TIA. This was a fixed percentage of the VREF or divided reference voltage ($V_{REF_{DIV}}$), and is chosen dependent on current flow to the WE. This allowed the computation of the current flowing at the WE of the three-electrode system (I_{WE}), as follows. $I_{WE}=(V_{out}-V_{REF_{DIV}})/R_{tia}$ has been established using the aforementioned-procedure. R_{tia} was chosen depending on the sensitivity of the sensor, given in ppm, as previously discussed. The current of the sensor was then calibrated via software as a function of all described parameters.

4.3.7 Power Management, Data Transmission and User Interactivity

The developed wearable platform operated on a 3.7VDC lithium-ion (Li-ion) battery capable of providing up to 1000mAh. Battery replacement was a trivial task in the platform. The unregulated battery voltage was regulated to provide a constant 3VDC

source to the system through a battery voltage range of $3V_{DC} \leq V_{DC} \leq 3.7V_{DC}$. The system was designed to prevent Li ion battery drainage below a 3 V_{DC} - 2.4 V_{DC} threshold, as this can potentially cause an unsafe condition [224] through means of a Power Management Unit LP5921. The system operates with a current draw of 2 mA during normal operation with Bluetooth disabled. When Bluetooth capabilities were enabled by the user, the current consumption of the system increased to approximately 40 mA. As shown in the block diagram in Figure 4-1a, the Li-ion battery can be recharged on the wearable platform through a micro-USB device connected directly to a Li-ion battery charging circuit, which allows simultaneous system operation and charging functions.

The AFE LMP91000 was chosen as the signal path solution between the MSP430F5529LP and the sensor due to its ability to detect a current in the nano-Ampere (nA) range and provide an output voltage proportional to current times' gain factor. To ensure a reliable AFE sensing operation, automatic system calibration based on a sensor's OCP and a reliable reference voltage to the AFE sensing device, the DAC device (MCP4725) provided a configurable reference voltage to the AFE sensing device, of which a fixed percentage would be applied across the sensor for biasing purposes, as determined during calibration time. Having a fixed voltage percentage that was software programmable allows the platform to configure itself to any sensor to eliminate abnormalities that may be present. Information sent from the Bluetooth module to the receiving device is encrypted using a simple algorithm to avoid data compromise, and is subsequently decrypted at the authorized receiving device and displayed to the user.

4.3.8 Comparison of MC470 and LMP91000

To validate the device, data from the commercially available electrochemical device MC470 was compared with the constructed LMP91000 device, as shown in Figure 4-7a and 4-7b, respectively. During these experiments, both the devices were placed in an identical setup with similar parameters, as given in the experimental section. The concentration of ethanol used for these experiments was 7.272 M. The experiments were carried out for 700s, where the humidity was introduced after 50s and the ethanol was introduced after 200s. The biasing potential was kept constant at -0.2 V for both the experiments. Both results show there was interference due to humidity, and there was a response to ethanol (Figure 4-7a and 4-7b). Comparing the results in the same figure shows that the LMP91000 device has a 30-times higher current signal due to the presence of an amplifier in the device.

The effect of ethanol concentration on the fuel cell sensor was studied for sensor evaluation. In these experiments, there were ten different concentrations tested in the physiological range of transdermal ethanol (5ppm to 800ppm). The optimized sensor

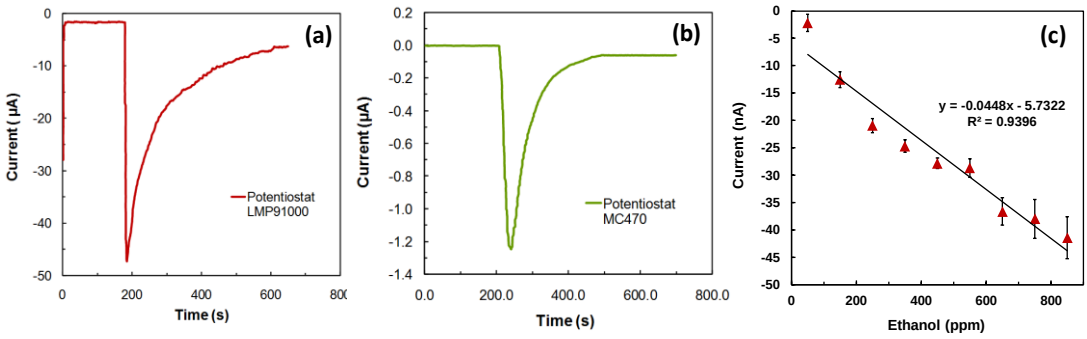

Figure 4-7 Amperometric data obtained in (a) a commercial MC470 potentiostat and (b) a LMP91000 potentiostat in the presence of ethanol and humidity (c) concentration vs. current plot showing the linear response of the sensor with the RSD of 30%.

operating parameters were 42% humidity at 25 ˚C, at -0.05 V biasing potential. The concentration vs. current plot given in Figure 6c shows that the sensor response is linear, from 50 ppm to 800 ppm, with the sensitivity of -0.23 nA ppm^{-1} cm^{-2} (RSD=30%), with the lowest detection limit of 5ppm. The RSD value for concentration below 50ppm was 55%, which went down to 18% for the concentrations higher than 50ppm. These results prove that the device, along with the sensor, has the capability to measure even the ethanol concentration within the physiological range.

Bland-Altman plots were used to characterize the repeatability and reproducibility of the sensor (Figure 4-8a and 4-8b). The plots show the average and difference between two measurements of current on the x-axis and y-axis, respectively. In the repeatability experiments, two sensors were studied, and the data was collected multiple times (n=10), whereas for reproducibility, ten different sensors were studied, and the data was collected twice in each sensor. The concentration of ethanol and percentage of humidity used in these experiments were 50ppm and 46%, respectively. Bland-Altman plots show that an absence

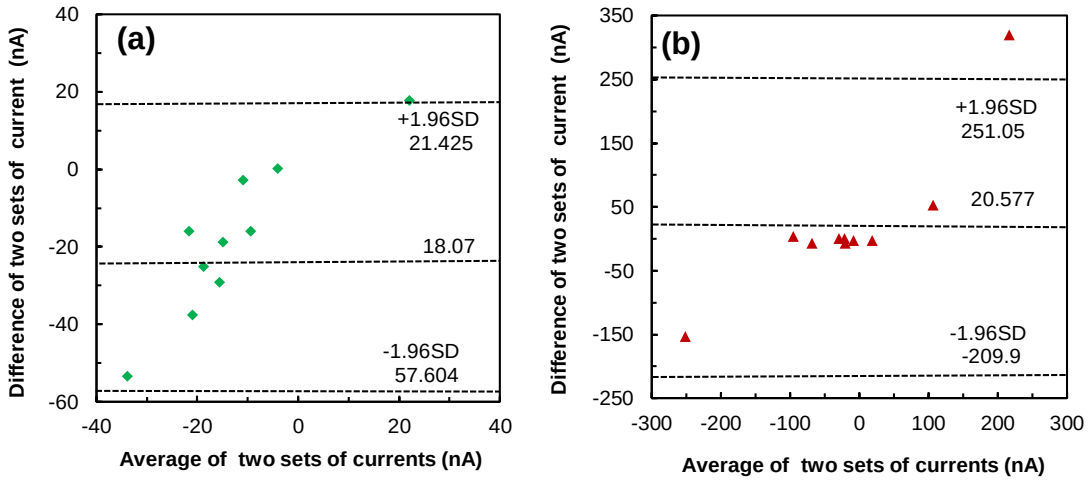

Figure 4-8. Bland-Altman plots representing (a) repeatability and (b) reproducibility of the micro-fuel cell sensor in the presence of 50 ppm of ethanol and 46% humidity. The biasing potential was -0.05V.

of bias in measures of repeatability (p=0.0004) and reproducibility (p=0.0004) were considered statistically significant. The correlation coefficient values for repeatability (r^2 = 0.8123) and reproducibility (r^2 = 0.8102) are closer to unity, indicating a strong relationship between multiple measurements. The limits of agreement are expressed as averages of the differences ±1.96 SD. The limits of agreement for repeatability were 21.43 and 57.60, and for reproducibility it was 251.1 and -209.9.

4.4 Conclusion

A miniaturized alcohol monitoring system containing a micro-fuel cell sensor with a compact potentiostat has been developed. The device includes data processing and transmission units with low power consumption, which can also provide a highly stable signal. The multi-modal technique provided a pathway to design a method to eliminate the major interfering factor, humidity, in an alcohol-based monitoring device. An algorithm was developed to implement self-calibration in the developed device to improve ethanol selectivity. The method in this investigation for eliminating signal response caused by humidity demonstrated a potential pathway for eliminating any organic volatile compound interfering signals. The modification of nickel-plated electrode with the thin film catalyst could be a prospective development of the present work, where sensitivity and detection limit can be improved several folds.

CHAPTER V

MULTIVARIATE ANALYSIS FOR IMPROVING THE CALIBRATION OF A FUEL CELL SENSOR FOR SENSING VOC

This results and discussion of this chapter is divided into three major sections. The first section presents the limitations of the linear calibration of a fuel cell sensor. The second section focuses on the improvement of the calibration of the fuel cell sensor employing a classification method, such as PCA and its limitations. Finally, the resolution of the overlapping of the signals employing the multivariate regression method, such as PCR, is discussed.

5.1 Background

Fuel cells are electrochemical devices that convert chemical energy into electricity, as discussed earlier. These devices are found in many different forms, specifically designed for intended roles. For example, miniaturized PEMFC have been widely used in breathalyzers. The PEMFCs operate at low temperatures and therefore can be used as a sensor in wearable devices. Compared to infrared-based sensors, PEM fuel cell sensors have portability and a long working lifetime as advantages [225]. However, both these sensors suffer from high interference due to humidity and volatile compounds. Due to high signal interference in a multivariate environment, these sensors cannot be used for continuous monitoring. These signal interferences also lead to signal fluctuation and overlapping over time. Therefore, the standalone sensor provides false positive and negative results, which makes the linear calibration model obsolete for the quantification of isoflurane or any volatile compound. Moreover, these environments exist in biological

fluids and vapors. The fuel cell sensors alone are incapable of specifically separating a single VOC signal in the biological environment. The non-specific detection of existing sensors is mainly due to the PEM's dependency on different ambient parameters, such as humidity, pressure, and temperature, for its function.

Data mining and pattern recognition techniques have become popular for the selective and accurate detection of volatile compounds in a multi-dimensional environment. These tools interpret datasets from single or multiple sensors to selectively quantify a specific compound. This can be achieved by training the computational algorithms with large and diverse data sets before implementing the sensor for real-time measurements. Among these techniques, multivariate statistics is a robust tool that provides precision measurement and classification [40 41 226]. The most common multivariate statistical techniques are PCA, DFA, and PLS [15 39 227]. PCA is a pattern recognition method that reduces the redundancy and dimensionality of the data sets through the simplification and interpretation of the data by the first few major components. These data plots contain most of the variance in the data without having preceding information on the data sets. This work presents a study of PCA with predicative regression model-driven isoflurane biosensor regression.

5.2 Experimental

Materials and the sensor fabrication approach were described in section 3.3.

5.2.1 Sensor set-up and measurement protocols

A chamber was used for the sensor setup, where the cathode had a window of (1.5 cm x 1 cm) so that the atmospheric oxygen could interact with the counter electrode. On the other side, the sealed chamber had an opening of 1 cm diameter cylinder (1.57 cm^3) to expose the working electrode to the isoflurane environment. During the experiment, the headspace remained constant at a height of 2 cm. During the measurement, the concentration of isoflurane at the headspace was calculated using Henry's formula at constant temperature, as follows [228]:

$$\frac{\text{Concentration of isoflurane in the liquid phase}}{\text{Concentration of isoflurane in the vapor phase}} = K_{w/a} \quad (1)$$

Here, $K_{w/a}$ is the "Ostwald partition coefficient." If a diluted isoflurane solution is brought to equilibrium in air, the partial pressure of isoflurane in the vapor phase is a function of the system temperature (25 ˚C) and the isoflurane concentration in the liquid phase. The partition coefficient of isoflurane is 0.61 at 25 ˚C [229]. Different concentrations (40 ppm, 80 ppm, 160 ppm, 320 ppm, and 775 ppm) of isoflurane were exposed to the working electrode of the fuel cell and measured by the amperometric method at the applied potential of -0.3 V.

5.2.2 Reaction mechanism

The reaction mechanism of the fuel cell involves oxidation at the anode and reduction at the cathode. The anodic reaction can be expressed by equation (2 – 4), where the oxidative addition of isoflurane occurs instead of a direct oxidation reaction.

Anode reaction:

$$Ni + R - Cl \rightarrow RNi(II)^{-} + Cl^{-} \quad (2)$$

$$Cl_2 + H_2O \rightarrow HCl + HClO \quad (3)$$

$$4HCl + 2Ni + 12H_2O \rightarrow 2NiCl_2.6H_2O + 4H^{+} + 4e^{-} \quad (4)$$

where, R-Cl is the isoflurane. As given in equation (3), the byproduct HCl is oxidized on the anode, and the electrons are produced in this process. On the cathode, the oxygen is reduced, as given in equation 5.

Cathode reaction:

$$O_2 + 4H^{+} + 4e^{-} \rightarrow 2H_2O \quad (5)$$

During this reaction, the electrons and H^{+} ions flow from the anode to cathode, generating a faradic current proportional to the concentration of isoflurane. This faradic current was detected by the amperometric method for this study. The biasing voltage across the working and reference electrode was -0.3 V.

5.3 Results and discussion

5.3.1 Linear calibration of the fuel cell sensor

The amperometric signals from different concentrations of isoflurane exposure vary within sub-nano Ampere, causing signal overlapping at narrow concentration ranges. In the case of low concentration and low measurement volumes, the rate of the reaction, rate of diffusion, and rate of evaporation are the limiting parameters. If the concentration of the interfering compound (example: humidity) is much higher than the isoflurane, the sensors' accuracy will be low. These limitations of the fuel cell sensor were studied in the presence of isoflurane with five different concentrations in ambient temperature and

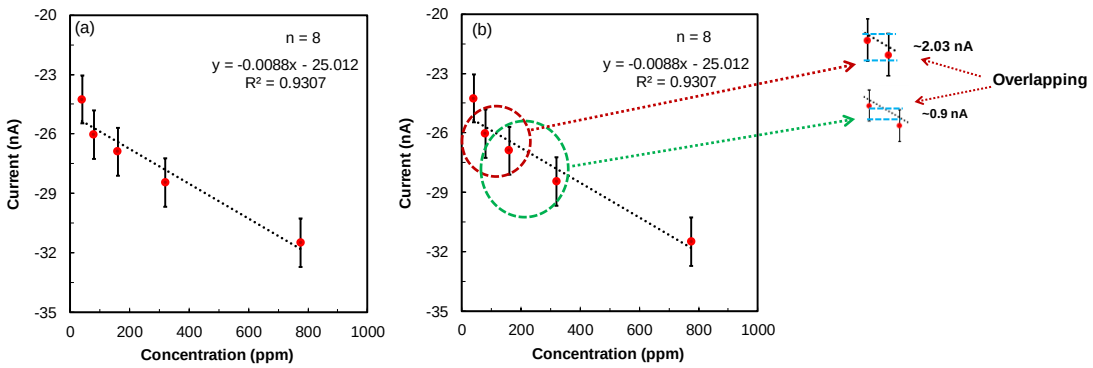

Figure 5-1: (a) Linear calibration plot of isoflurane measured in the fuel cell sensor and (b) Overlapping amperometric signals in the linear calibration plot (inset: the overlapping was in the sub-nano Ampere range).

humidity, as given in the experimental section. Each concentration was measured eight times and plotted in a linear plot, as given in Figure 5-1a. Even though the current signal increases with respect to the concentration of isoflurane, the linear calibration plot shows: (i) significant overlapping between the concentrations, (ii) excellent linearity with R^2 = 0.9307, and (iii) very low sensitivity (0.0112 nA ppm^{-1} cm^{-2}). The magnification of each data point (in Figure 5-1b) reveals that there was a significant overlapping of the signals between the different concentrations, which impedes reliability at the ppm level of detection. For example, the overlapping between 80 ppm to 160 ppm and 160 ppm to 320 ppm were determined as 2.03 nA and 0.9 nA, respectively. Although the sensor shows excellent linearity, its poor sensitivity and the overlapping of the signals in the calibration curve significantly affect the determination. To overcome these calibration issues, PCA was explored.

5.3.2 The implementation of principal component analysis (PCA)

PCA is a powerful technique to eliminate redundancy and dimensionality in data sets. This method was applied to the above-mentioned data by the following algorithm: (i) standardizing the data, (ii) obtaining the eigenvectors and eigenvalues (d) from the covariance or correlation matrix (iii) sorting eigenvalues in descending order and choosing the k eigenvectors that correspond to the k largest eigenvalues. k is the number of dimensions of the new feature subspace ($k \leq d$). Mathematically, for a response matrix X, each element x_{ij} concerns the j_{th} measurement value for the i_{th} considered data, and the k_{th} principal component is noted PC_k [227]:

$$PC_k = \sum_{i-1}^{n} \alpha_{ik}\, x_{ij} \qquad (6)$$

where n is the number of variables and α_{ik} is the eigenvector for the i_{th} variable. Then, the original data was multiplied by the eigenvectors to re-orient the data onto the new axes, and these newly oriented data were plotted subsequently.

For the mathematical calculations, two response variables — steady-state current (I_{ss}) and difference (ΔI) between I_{ss} and control signal were considered, as shown in Figure 5-2a. The (40 X 2) matrix was created for each variable, and 5 datasets (5 different concentrations) contain the (8 X 2) matrix. The mean of each data set was governed and standardized. A covariance matrix was developed for those two variables, and the eigenvectors (V) were determined from this matrix. The eigenvalues (d) were 14.3088 and 1.8255, respectively. Here, the number of dimensions of the principal components, k = 2 in the subspace, and eigenvalues (or, eigenvectors) are equal to the principal components (k = d); therefore, both were considered as principal components. The data variances of the first and second principal components are 88.68% and 11.31%, respectively. The final

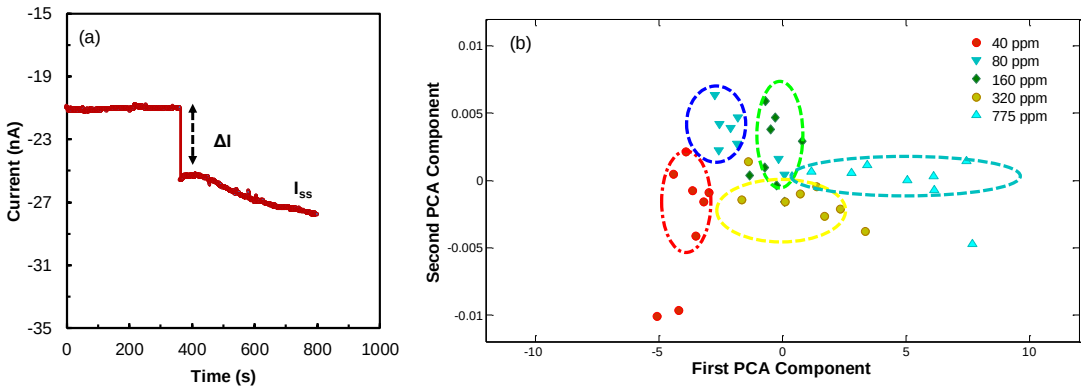

Figure 5-2: (a) The variables (Iss and ΔI), which are considered for PCA, and (b) PCA for the five different concentrations of isoflurane, considering two variables.

datasets were plotted from the standardized eigenvector data. It is observed from the plot that there is a marginal overlap between the domains of 160 ppm, 320 ppm, and 750 ppm.

Results show that (in Figure 5-2b), data can be separated into five different clusters corresponding to specific concentrations, which removes the redundancy and reduces the dimensionality of the linear calibration data of isoflurane. The same figures show 8 data points having a maximum of 2 outliers from each cluster or concentration group. The clusters are obvious and distinguishable, though there are few overlapping between the data points due to indefinite variables (Figure 5-2b). The indefinite variables can be listed as: (i) fuel cell membrane degradation over time, (ii) electrode surface fouling, (ii) membrane water content variation and (iii) temperature variation. It is observed from the both subspaces that the cluster of 750 ppm dispersed more, compared with the other data sets, due to the above-mentioned reasons. Although the clusters of the PCA are isolated from each other for the five different concentrations, this cluster model is incapable of determining any regression model for the isoflurane concentrations within the physiological range.

5.3.3 Regression analysis for calibration

The objective of this study was to develop a PCA regression model from the data matrix. It was achieved by considering all the data points from the data matrix of the above-mentioned variables. In these calculations, the matrix was expressed in another form, given in equation 7 [226].

$$D = RC \tag{7}$$

where *R* and *C* are the scores and loading matrix, respectively. The eigenvalues (d), eigenvectors (V) and covariance matrix (Z) are directly related to the data matrix, D. To minimize the residual error, the eigenvectors were derived by subtracting d and V from Z. This iteration process was continued for eigenvectors until the eigenvalue reached below 0.001 of the maximum one. Equation 7 was modified by employing a transformation matrix, as *R* and *C* matrices do not exhibit any chemical and physical connotation. This transformation can be executed, as follows:

$$D = (RT)(T^{-1}C) \tag{8}$$

Here, *T* is a square matrix having dimension n, and n is the number of significant factors determined by PCA. This transformation matrix can be expressed as below:

$$T = \begin{vmatrix} \mathrm{xcos}(\delta) & -\mathrm{ysin}(\delta) \\ \mathrm{zsin}(\delta) & \mathrm{wcos}(\delta) \end{vmatrix} \tag{9}$$

The values of the coefficients a, b, c, and d are unity when this matrix is orthogonal, or else they can be determined considering the information of the real factors. In our case, x = 1, y = -2.5, z = 2, w = 5, and δ = 354°. For regression fitting, loading fractions C_1 and 1-C_1 were determined empirically from PCA and fitted with respect to the concentration of isoflurane [28], as shown in Figure 5-3. As all the experimental parameters are constant,

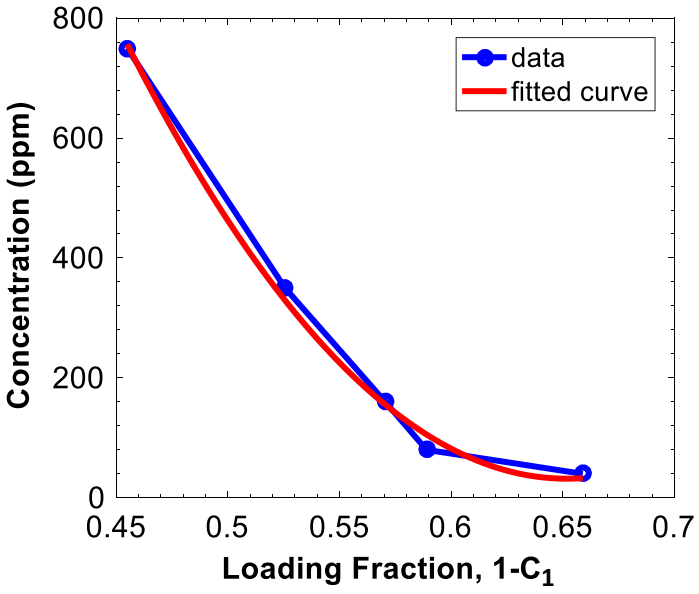

Figure 5-3: PCA regression model for the calibration of a micro-fuel cell sensor for isoflurane detection.

the sum of the loading fractions was approximately unity (1). Therefore, the regression plot was obtained from the loading fraction (1-C_1) vs. concentration (y). A polynomial function was fitted with the regression curve using MATLAB, following the equation below:

$$y = \alpha(1 - C_1)^2 + \beta(1 - C_1) + \gamma \quad (10)$$

Here, the values of coefficients α, β, and γ are 1.87 x 10^4, -2.437 x 10^4, and 7.974 x 10^3, respectively. Any isoflurane concentration within the physiological range can be determined by fitting the loading fraction (x) in this regression model, as shown in Figure 5-3.

5.3.4 The operation of the miniaturized potentiostat

A wearable platform (Figure 5-4a) with a miniaturized potentiostat has been developed for a sustainable solution for isoflurane detection. It was housed with an

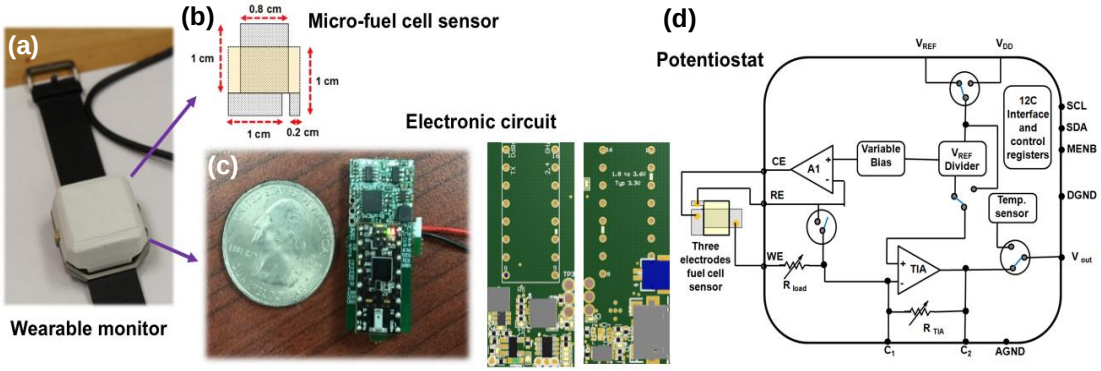

Figure 5-4: (a) Wearable device for isoflurane detection, (b) Design of a micro-fuel cell sensor (c) Printed circuit board of four layers' miniaturized potentiostat (left) its size, and (right) and its design, (d) LMP91000 potentiostat integrated with a three-electrode micro-fuel cell sensor.

integrated data acquisition system, Li-ion battery, and a three-electrode fuel cell sensor. The fabricated three-electrode sensor (shown in Figure 5-4b) was integrated with four-layers of printed circuit board (PCB), as shown in Figure 5-4c. This customized four-layered PCB for data acquisition was designed to accommodate a miniaturized potentiostat (LMP91000, as shown in Figure 5-4d), an ADC, and a low power data processing microcontroller – nRF51822 (incorporated with a 32-bit ARM® Cortex™ M0 CPU with 256kB/128kB flash + 32kB/16kB RAM). This device uses nRF51822 from a Nordic semiconductor as an integrated wireless microcontroller with Bluetooth low energy (BLE) capabilities to provide wireless communication and peripheral controls. This embedded 2.4GHz transceiver with nRF51822 supports BLE for wireless data transmission. The detection method used in this system was amperometric, and the functionality of the potentiostat has been reported previously [33].

This LMP91000 potentiostat can be configured to perform electro-analysis for isoflurane. The device begins amperometric operation when it detects a voltage less than

0.02 V across the sensor electrodes (reference and working). The current generated from the working electrode was determined, as follows [33]:

$$I_W = \frac{(V_o - V_{REF_{DIV}})}{R_{tia}} \quad (11)$$

Here, I_W is the current generated from the micro fuel cell, V_o represents output voltage, $V_{REF_{DIV}}$ represents divided reference voltage, and R_{tia} is the feedback resistance of the trans-impedance amplifier (shown in Figure 5-4d). This detected current (I_W) corresponds to the concentration of isoflurane, which can be determined through calibration. The current from LMP91000 is converted to a potential and fed to the internal ADC of the wireless microcontroller. This information is then sent wirelessly via Bluetooth to the end device (e.g. smartphone), which can send the data to the cloud.

5.3.5 Power management of wearable device

The algorithm for precise calibration requires computational power, which is demanding on both devices used. Hence, the calibration algorithm for precise results can be done on the cloud once the data are uploaded. This saves battery power and comparatively limited computational power over the device and phone. The power consumption of the device depends on different parameters: i. run time current drawn from the central processing unit (CPU), ii. BLE transmission and communication, and iii. LMP91000's amperometric operation. Since most of these operations only occur for the emergency period, the modules that run them can be pushed to a lower power state, thereby reducing their consumption. The CPU runs for a short time during BLE transmission and the ADC of analog output from LMP91000. The remaining time can be utilized by the

CPU to run other peripheral operations consuming ~ 2.6 µA at a lower power. LMP91000, while in the amperometric mode, consumes ~10 µA. It consumes an average current of ~7.95 µA over time, with a total uptime of 39%. Including ~5 µA for cell conditioning, the current for this sensor is calculated as 9.75 µA with the LMP in "stand mode" for 60% of the time. While the nRF51822 runs for ~5 seconds at a lower power from the CPU, it can be shown that the total power consumption is ~56 µW. Using a 3.7 V and 365 mAh battery, the operational lifetime of the system is ~ 5 days.

5.3.6 Database management and user interactivity

The database system was designed around the required flow of information, which is a general design for such systems (shown in in Figure 5-5a). The device captures the raw data and sends it via BLE or Bluetooth smart to a compatible smartphone. The smartphone serves as a gateway for the data to the cloud. The cloud hosts the database, storing data of relevant subjects/users securely. The data can be accessed in a hierarchical scheme, with the server admin having the highest level of access. This is to ensure the proper handling of sensitive medical information. Anlaytic tools can be built on the cloud to provide data analysis for the corresponding isoflurane level in blood. An APP or a web portal was developed at the end interface for the anesthesiologist to monitor this data.

The database system consists of three layers (shown in Figure 5-5b): i. user interface (UI), ii. logic, and iii. data. Each of the three layers of this system is a subsystem of the whole. User interface allows the anesthesiologist to control the system with touchscreen presses. It provides him with an option to scan for and connect to a device, initiating the connection services in the next layer via an APP or a web portal. The UI

displays to him the state of the patient and measurements of the isoflurane concentration in blood, and allows him to select what kind of graphs they would like to view, as shown in Figure 5-5b.

The UI is programmed in Java and XML. Logic is the bridge between the UI and data subsystems, and it transmits data between th UI and the data subsystems (shown in Figure 5-5b). This subsystem is made up of the BLE Connection service and the DB

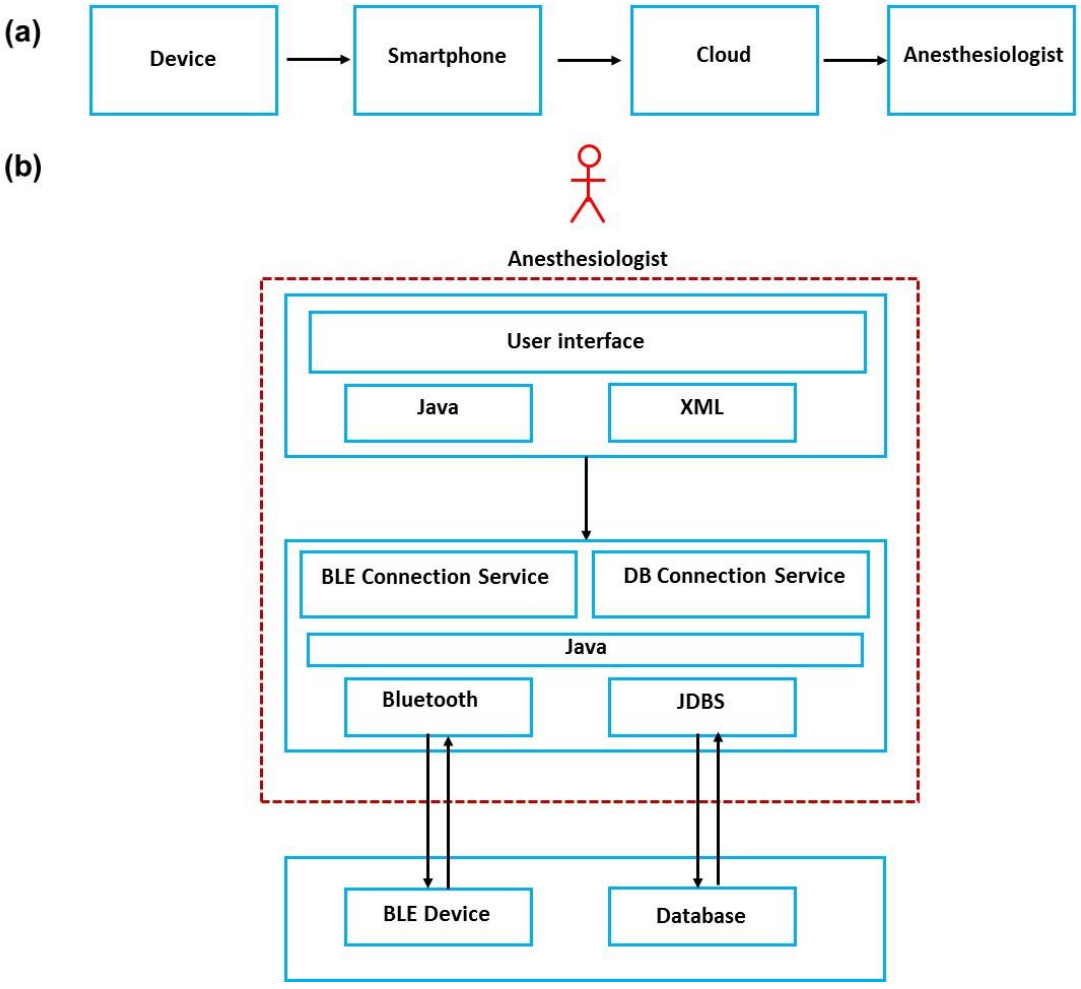

Figure 5-5: (a) Block diagram of the wearable device operation for isoflurane measurement, and (b) Different layers of the database subsystems.

Connection service. They allow the app to connect to the micro-fuel cell sensor device and the database, respectively. The BLE Connection service also manages this sensor on the device and formats the data from them to make it readable. Contrarily, data subsystems consist of the BLE biosensing device, from which the data originates, and the database, where the data are stored. In between this, the data moves through the Logic layer for processing. The database runs on a MS SQL Server.

5.4 Conclusion

PCA and its predictive regression analysis were successfully implemented for the isolation of signals in the sub-nano Ampere range of the isoflurane data. The conventional linear calibration method is limited in isolating signals for minimal fluctuations due to lower sensitivity (0.0112 nA ppm^{-1} cm^{-2}), which has substantial standard deviations. PCA accurately classified and discriminated different concentrations in the data subspace. The eigenvalues for two variables were 14.3088 and 1.8255, respectively, which inferred the command of the 1^{st} principal component (88.68%). The cluster plot of PCA is unable to demonstrate the relationship between inter-calibration points. Therefore, a predictive model is derived from PCA, which can be employed for regression fitting. Last, a miniaturized fuel cell sensor was designed in a wearable format for isoflurane detection that can operate in a low power mode, having ~5 days battery life.

CHAPTER VI

DETERMINING ALCOHOL AND ISOFLURANE FROM HUMAN SAMPLES/SUBJECTS

This chapter is divided into two major sections. The first section presents the POC detection of alcohol from perspiration of the human skin. The second section focuses on the analyses, results, and discussion of the application of the PEMFC sensors for the detection of isoflurane from human sweat (*in vitro*) and human subjects (*in vivo*).

6.1 Wearable device and its components

A watch-style wearable platform with a miniaturized potentiostat was constructed for the detection of VOCs, like ethanol or isoflurane, in humans. The sensor fabrication was described in detail in section 3.4. The development of said wearable device was mentioned in sections 5.3.4 and 5.3.5.

6.2 Determining alcohol from human skins

6.2.1 Protocol-sensor calibration and human study

During calibration and measurements, the headspace for alcohol vapor was maintained constant at a height of 0.1 cm and area of 1 cm x 1 cm for every data set. The concentration of alcohol at the headspace was calculated using Henry's formula at a constant temperature [228]. Different concentrations (50 ppm, 100 ppm, 200 ppm, 400 ppm, 600 ppm, 800 ppm, and 1000 ppm) of alcohol were exposed to the WE, and the

corresponding currents were recorded at the potential of -0.05 V. The recordings were used to build the PCR model.

Human studies were executed for 5 anonymous subjects (S1, S2, S3, S4, and S5) with their written consent to take part, following the Institutional Ethical Guidelines (IRB-17-0300-AM01). The measurements (control variables) were made at 25˚C and 55% relative humidity. All data collected were from the upper side of the wrist, like when wearing a watch. The gap between the sensor and the skin was 0.1 cm during measurements to maintain a constant headspace volume. Each subject started drinking after 30 min. of wearing the device. Each shot contained 50 ml, 35% alcohol from the same brand, and 6 consecutive shots were consumed by each subject at 10 min. intervals. Commercial breathalyzer device data was also collected after 5 minutes of drinking each shot. The details of this study were summarized in Table 6.1, as below:

Table 6-1. Human subjects study for transdermal alcohol determination

No. of Subject	Age (Yrs.)	Wei-ght (Kg)	Distributi on factor (V_d)	Amount contains in each shot (ml)	Total Amo-unt (ml)	Interval in between of shots (min.)	No. of shot	Alcohol Conc. (%)
S1	65	88.9	0.68	50	250	10	6	35
S2	28	80.74	0.68	50	250	10	6	35

S3	32	84.37	0.68	50	250	10	6	35
S4	21	77.11	0.6	50	250	10	6	35
S5	30	81.193	0.68	50	250	10	6	35

6.2.2 Sensor calibration for alcohol vapor quantification

The linear regression calibration of the fuel cell sensor for alcohol vapors was investigated within the physiological range. The data set contained amperometric signals of seven different concentrations were obtained, with over 88 samples of each concentration. The results for the same concentrations varied within the sub-nano Ampere, causing signal overlap. The plausible causes of signal overlap include: i. deviation of the baseline over time due to the change in H^+ ion counts in PEM, ii. change in reaction rate of the electrodes due to transient fouling, iii. slight variation in the ambient environment,

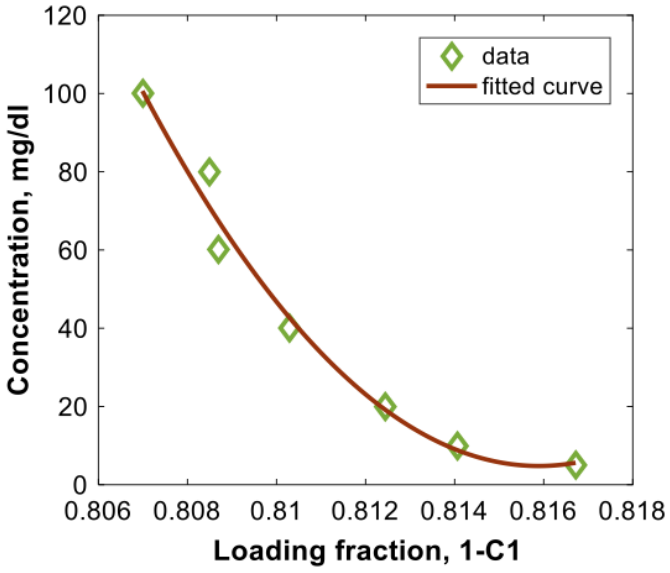

Figure 6-1: The PCR model of the fuel cell sensor for alcohol vapor.

such as humidity interference. The signal overlaps between the alcohol concentrations were resolved by employing a PCR model, which was derived from the sensor data. PCR was executed by MATLAB considering all the data points from the matrix of 7 x 88, where the number of sample concentrations was 7 and the data frequency was 88.

The values of the coefficients a, b, c, and d are unity when this matrix is orthogonal, or else they can be determined considering the information of the real factors. In this case, a = 2, b = - 20.5, c = 2.5, d = 20, and δ = 355°. For regression fitting, loading fractions C_1 and 1-C_1 were determined empirically from PCR and fitted with respect to the concentration of alcohol, as shown in Figure 6-1. As all the experimental parameters are constant, the sum of the loading fractions was approximately unity (1). Hence, the regression plot was obtained from the plot of a loading fraction (1-C_1) vs. concentration (y), where the coefficient of determination (R^2) was 98.15%. A polynomial function was fitted with the regression curve using MATLAB, following the equation below:

$$x = \alpha(1 - C_1)^2 + \beta(1 - C_1) + \gamma \qquad (1)$$

Here, the values of coefficients α, β, and γ were 1.218×10^7, -1.99×10^7, and 8.124×10^6, respectively. An unknown vapor concentration (x) can be determined by fitting the loading fraction (1-C_1) in this regression model. The algorithm of this model was programmed in the microcontroller of the device for accurate data fitting.

6.2.3 Human studies -validation of the transdermal alcohol sensor

The BAC readings from the transdermal alcohol sensor and the breathalyzer were validated by comparing theoretical values (Figure 6-2). The % of the BAC values of the theoretical model were calculated from equation 2 [230]. The plots show a linear

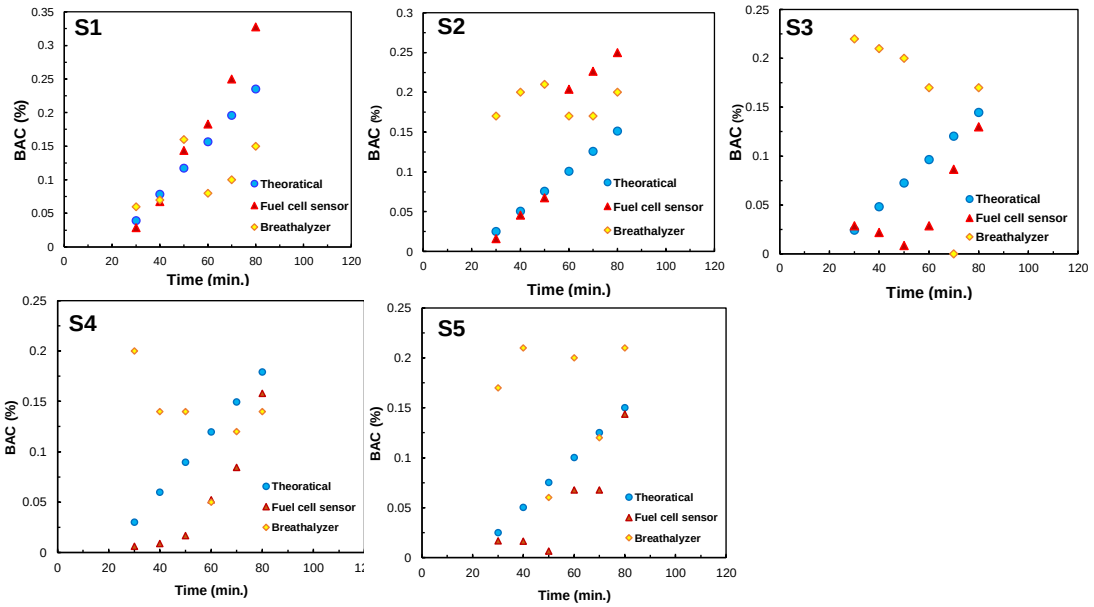

Figure 6-2: The comparison of a transdermal alcohol sensor and breathalyzer with the theoretical model for 5 human subjects (a) S1, (b) S2, (c) S3, S4, and S5.

relationship between theoretical % of the BAC with the dose of alcohol ingestion, with respect to time for all three subjects (blue dots in Fig. 6-2). For this model, alcohol consumption at every 10 min (6 consecutive shots) was considered for all subjects, where each shot contained 50 ml or 35% of alcohol.

$$\%BAC = \frac{(vol.\ ingested\ (ml)\ x\ \%\ alcohol\ x\ S.G._{\ eth.} x\ 1000)}{V_d\ x\ body\ weight\ x\ 10}\ x\ 0.001 \qquad (2)$$

$S.G._{eth.}$ is the specific gravity of ethanol and V_d is the volume of distribution, which is 0.68 and 0.6 for males and females, respectively.

Breathalyzer data showed a nonlinear response with each shot for all 5 subjects (yellow dots in Fig. 6-2). The average deviation of the breathalyzer results away from the theoretical values was about 162%. Even at the first shot it showed a high false positive reading and intoxication (subjects 2 and 3), then gradually correlated with the theoretical values in consecutive shots. The deviation and the false positive signals can be

corroborated to the mouth-alcohol contamination [231 232]. It is evident from these results that the discrete % of the BAC data recorded from a breathalyzer have limitations for the accurate determination of alcohol.

The same human subjects tested with the transdermal alcohol sensor showed a significant correlation with the theoretical values with minimal deviation (red dots in Figure 2), a 75% improvement in accuracy compared to the breathalyzer. The device provided continuous % of the BAC data, which was processed and fitted into the above PCR model to determine accurate transdermal alcohol content (TrAC), where it was converted into % of the BAC by the following equation 3 [130]:

$$BAC\ (gl^{-1}) = 0.71 \times TrAC\ (gl^{-1}) \quad (3)$$

where the correlation coefficient, r = 0.912. In all three subjects, the transdermal alcohol sensor provided slightly lower values at the first few shots and higher values in consecutive shots compared to theoretical values. These deviations can be attributed to the slow alcohol metabolism at the beginning, where it takes a while for the full concentration to vaporize from the skin. However, with the consecutive shots, there was an accumulation of alcohol vapor at the epidermis [129]. In subjects 2 and 3, the sensor values deviated further from the theoretical model, which can be attributed to i. a variation in self-reported body weight, ii. unknown physiological conditions, including food/drug consumption prior to alcohol ingestion, iii. a variation in metabolism rate from person to person. Moreover, these variations were influenced by numerous factors, such as age, race, thickness of fat and skin layer, ingestion of food or medication, etc. [233]. These mentioned factors are not included in our theoretical model, as they are the subject of future work.

6.3 Determination of isoflurane from human sweat

6.3.1 Linear calibration of the fuel cell sensor for isoflurane detection

The amperometric signal of the sensor from five different concentrations of isoflurane exposure at ambient temperature and humidity were studied. Each concentration was measured 8032 times and plotted in a linear plot, as given in Figure 6-3a. The results show that the current increases with respect to the concentration of isoflurane. The linear calibration plot shows: (i) a significant overlap between the concentrations, (ii) excellent linearity with R^2 = 0.8605, and (iii) very low sensitivity (~ 0.038 nA ppm^{-1} cm^{-2}). The relative standard deviations (RSD) for the five different concentrations were determined to be 5.84%, 5.77%, 6.09%, 6.76%, and 10.62%, respectively. From Figure 6-3a, it has been revealed that there was a significant overlap of the signals between different concentrations due to higher RSD, which impedes the reliability at the ppm level of detection. For example, the overlapping between 80 ppm to 160 ppm and 160 ppm to 320 ppm were determined to be 2.05 nA and 2.24 nA, respectively. Although the sensor shows excellent linearity, its poor sensitivity and the overlapping of the signals in the calibration curve significantly affects the determination of any given sample. This sub-nano Ampere signal overlaps at narrow concentration ranges and can be attributed to the limiting parameters, such as (i) the rate of the reaction, (ii) the rate of diffusion, and (iii) the rate of evaporation. If the concentration of the interfering compounds (e.g. humidity) is much higher than the isoflurane, the sensors' accuracy will be reduced, as discussed earlier. To overcome this calibration issue, PCR was explored.

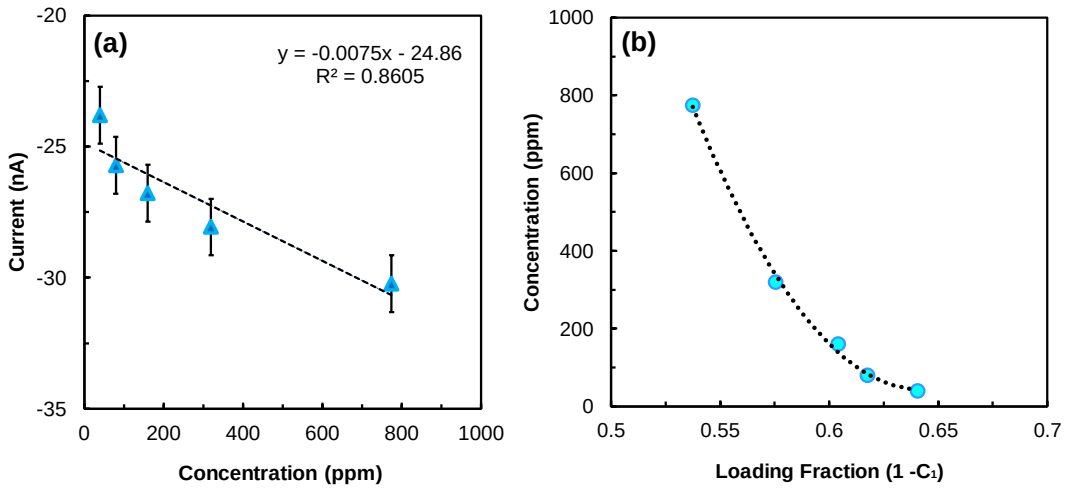

Figure 6-3: (a) Linear calibration of isoflurane measured in a fuel cell sensor, inset: fuel cell sensor and (b) Calibration curve obtained from the PCR model.

6.3.2 PCR for the calibration of a fuel cell sensor for isoflurane

PCR was executed by MATLAB considering all the data points from the matrix of 5 X 8032, where the number of sample concentration was 5 and the data frequency was 8032. The values of the coefficients a, b, c, and d are unity when this matrix is orthogonal, or else they can be determined considering the information of the real factors. In our case, x = 1, y = - 2.5, z = 2, w = 5, and δ = 351°. For regression fitting, loading fractions C_1 and 1-C1 were determined empirically from PCR and fitted with respect to the concentration of isoflurane, as shown in Figure 6-3b. As all the experimental parameters are constant, the sum of the loading fractions was approximately unity (1). Therefore, the regression plot was obtained from the plot of the loading fraction (1-C_1) vs. concentration (y), where the coefficient of the obtained determination (R^2) was 99.77%. A polynomial function was fitted with the regression curve using MATLAB, following the equation below:

$$c = \alpha(1 - C_1)^2 + \beta(1 - C_1) + \gamma \qquad (4)$$

Here, the values of coefficients α, β, and γ are $1.789x10^4$, $-2.329x10^4$, and $7.626x10^3$, respectively. An unknown concentration can be determined by fitting the loading fraction ($1-C_1$) in this regression model.

6.3.3 The measurement of isoflurane vapor from sweat samples (in vitro)

In humans, a minimal percentage of isoflurane is excreted through the skin by sensible and insensible perspiration [234 235]. This study was designed to determine the feasibility of the fuel cell sensor to measure the isoflurane vapor released from the sweat. The headspace of human sweat samples with various isoflurane concentrations was measured and compared with theoretical values to validate the sensor readings. Four different sweat solutions with isoflurane concentrations v/v%: 0.01%, 0.013%, 0.02%, and 0.038%, respectively, were tested. The theoretical isoflurane vapor concentrations were derived through Henry's formula [228]. The readings from the sensor were fitted with both linear regression and PCR models (Figure 6-4) to identify deviations from the theoretical

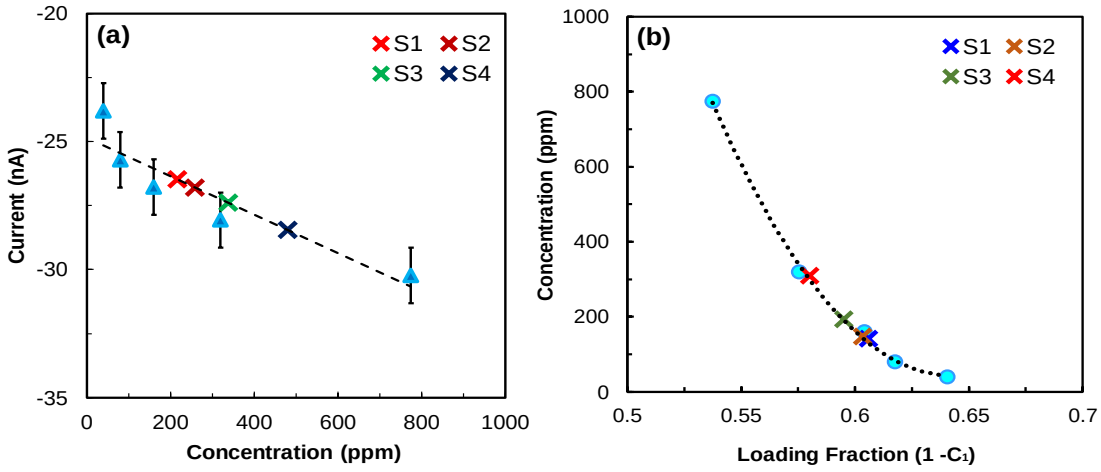

Figure 6-4: The PCR model of the fuel cell sensor for alcohol vapor.

values. Due to overlapping signals in the linear regression model, there was significant deviation from theoretical values (~67.72%), resulting in low resolution and inaccuracy (Table 6-2). The data from the PCR model improved compared to linear regression with a minimal deviation of about 12.74%. This ~81% improvement can be attributed to the consideration of covariates in the PCR model, compared to the univariate in linear regression. These results show the micro-fuel cell sensor, along with PCR fitting, can be used to determine the isoflurane vapor concentrations from the sweat.

Table 6-2. Comparison of PCR with linear regression for isoflurane detection in sweat

Sample	Theoretical (ppm)	Linear regression (ppm)	Deviation (%)	PCR (ppm)	Deviation (%)
S1	112	216.91	93.67	141.59	26.42
S2	144	258.24	79.33	147.36	02.33
S3	216	338.4	56.66	192.63	10.82
S4	350	480.24	37.21	310.08	11.41

The micro-fuel cell sensor device was successfully implemented for determination of transdermal isoflurane. The isoflurane vapor concentrations derived from PCR correlated with theoretical values compared to the linear regression model. PCR enabled isolation of signals in the sub-nano Ampere range and improved resolution of signal on an average of five times compared to the linear regression. PCR accurately classified and discriminated different concentrations in the subspace. Hence, PCR method was

implemented for the in vivo determination of transdermal isoflurane with for the different anonymous humans subjects, as described below in section 6.4.

6.4 Transdermal isoflurane determination from human subjects (*in vivo*)

6.4.1 Protocol-sensor calibration and human study

During calibration and measurements, the headspace for isoflurane vapor was maintained constant at a height of 0.1 cm and area of 1 cm x 1 cm for every data set. The concentration of isoflurane at the headspace was calculated using Henry's formula at constant temperature [228]. Different concentrations (50 ppm, 100 ppm, 200 ppm, and 400 ppm) of isoflurane were exposed to the WE, and the corresponding currents were recorded at the potential of -0.05 V. The recordings were used to build the PCR model, as similar to the previous alcohol study.

The human studies were executed for 4 anonymous subjects (S1, S2, S3, and S4) during their surgeries in the operation theater at 20˚C and 55% relative humidity, under IRB-20180767. The controlled environment in the operating theater ensured a constant temperature and a relative humidity level during the measurements. The isoflurane delivery to each subject was also maintained the same during the surgery. All the subjects wore the device on the front side of their wrists. The gap between the sensor and the skin was maintained at 0.1 cm during measurements to keep the headspace area the same. Each subject wore the device before 20 min. of isoflurane exposure for a stable steady-state baseline of the signals. The gold standard infrared spectroscopy (IR) data were also

collected after the exposure of isoflurane during surgery. The details of this study are as shown in Table 6-3 below:

Table 6-3. Human subjects' study for transdermal isoflurane determination

No. of Subject	Age (Yrs.)	Weight (Kg)	Height (cm)	Duration of exposure (min.)	Case
S1	41	124.738	170.18	74	Umbilical hernia repair
S2	64	82.554	175.26	52	Cysto-retroscopy with resection of bladder tumor
S3	70	131.542	190.5	145	Excision leucoma
S4	44	127.006	165.1	145	Laparoscopic cholecystic

6.4.2 The calibration of a fuel cell-based wearable device for isoflurane vapor quantification

The linear regression calibration of the fuel cell sensor for isoflurane vapors was investigated under the physiological range. The data set contained amperometric signals of four different concentrations obtained over 20 times. Like alcohol, PCR was executed by MATLAB considering all the data points from the matrix of 4 x 20, where the number of sample concentrations was 4 and the data frequency was 20.

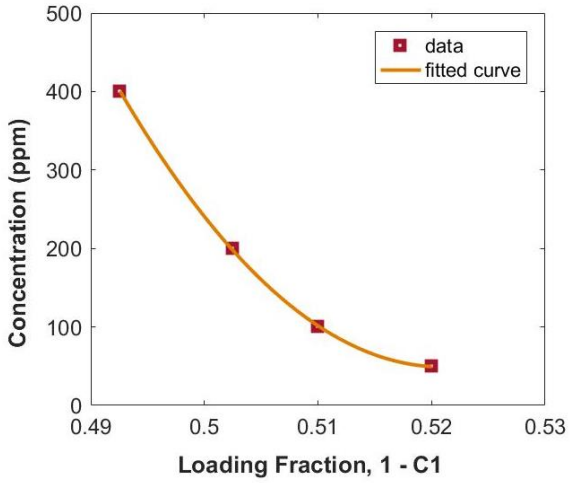

Figure 6-5: The PCR model of the fuel cell sensor for isoflurane vapor.

The values of the coefficients a, b, c, and d are unity when this matrix is orthogonal, or else they can be determined considering the information of the real factors. In this case, a = 1, b = - 2.5, c = 2, d = 5, and δ = 351°. For regression fitting, loading fractions C_1 and 1-C_1 were determined empirically from PCR and fitted with respect to the concentration of isoflurane, as shown in Figure 6-5. As all the experimental parameters are constant, the sum of the loading fractions was approximately unity (1). Hence, the regression plot was obtained from the plot of the loading fraction (1-C_1) vs. concentration (y), where the coefficient of determination (R^2) obtained was ~99%. A polynomial function was fitted with the regression curve using MATLAB, following the equation below:

$$x = \alpha(1 - C_1)^2 + \beta(1 - C_1) + \gamma \qquad (5)$$

Here, the values of coefficients α, β, and γ were 4.316×10^5, -4.544×10^5, and 1.184×10^5, respectively. An unknown isoflurane concentration (x) can be determined by fitting the loading fraction (1-C_1) in this regression model. The algorithm of this model was programmed in the microcontroller of the device for accurate data fitting.

6.4.3 Human studies -validation of the transdermal isoflurane sensor

This study was executed in a controlled environment following the protocols mentioned in section 6.4.1. All data collected were from the front side of the wrist as shown in Figure 6-6a. The blood isoflurane readings from the fuel cell sensor were validated by comparing the concentrations measured by the gold standard IR device (Figure 6-6b – 6-6e). These plots showed comparisons between blood isoflurane levels of two devices with the exposure of isoflurane, with respect to time for four anonymous subjects. The average deviation of the steady-state fuel cell responses from the IR device for the subjects 1-4 were 18.04%, 3.11%, 5.89%, and 30.12%, respectively. The average deviation from the steady-state responses of IR was ~14.29%. It is evident from these results that the discrete % of blood isoflurane data, recorded from fuel cell sensors, have a moderate deviation for the determination of isoflurane.

These deviations can be attributed to the lower diffusion rate of transdermal isoflurane at the beginning, where it took a while to reach to steady-state levels. The sensor values deviated further from the IR device for the following reasons: i. minute errors in calibration set-up, ii. the variation of the thickness of skins, which affected the measurements of transdermal isoflurane concentrations, iii. unknown physiological conditions, including food/drug consumption prior to isoflurane exposure, iii. the variation in metabolism rate from person to person [237]. Moreover, this variation was influenced by numerous factors, such as age, race, or suction during operation.

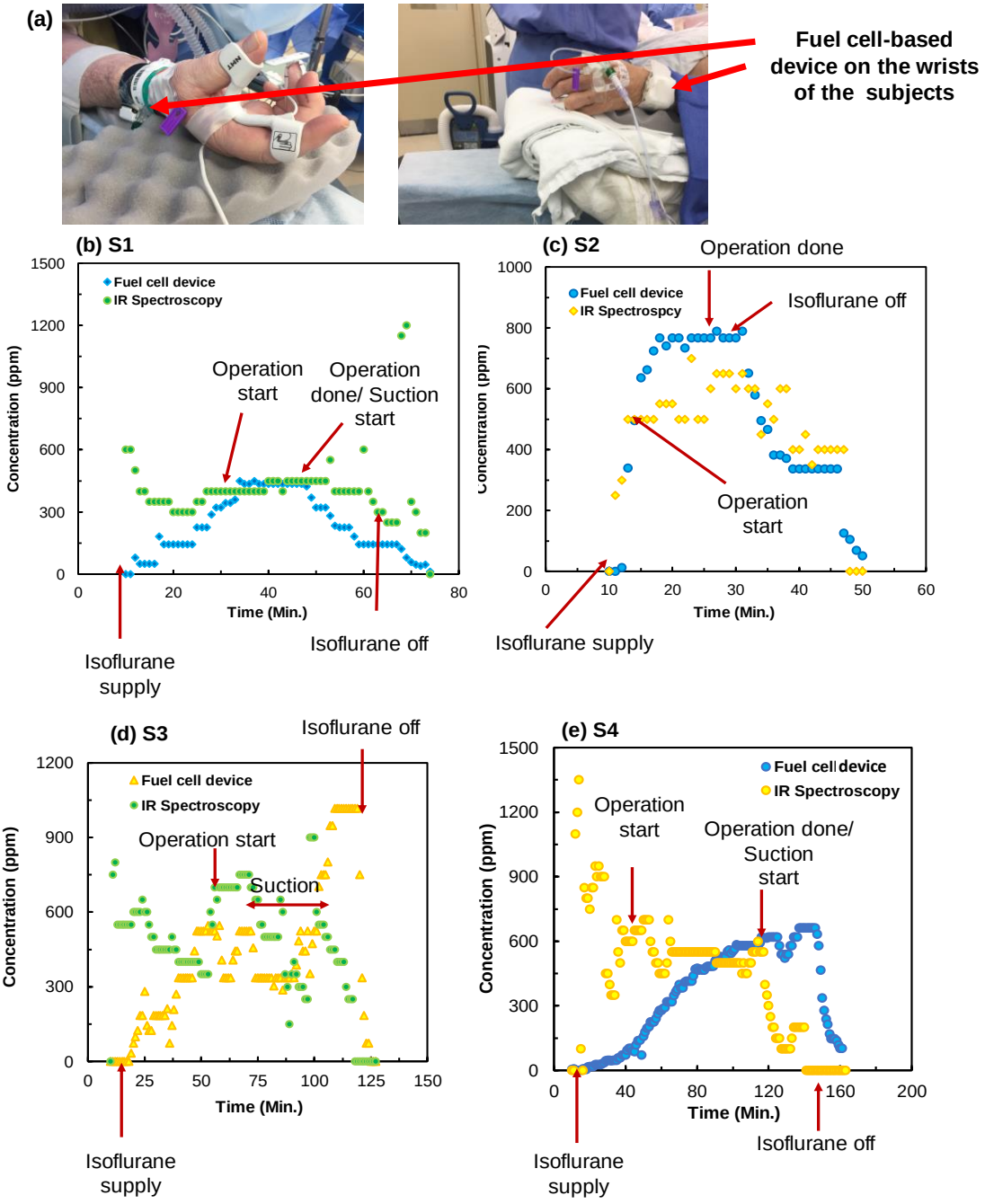

Figure 6-6: (a) Fuel cell-based device on the wrists of the subjects, (b to d) Comparison of fuel cell sensors and gold standard infrared spectroscopy devices for the blood isoflurane determination with for 4 human subjects S1, S2, S3, and S4.

CHAPTER VII
CONCLUSIONS

7.1 Summary and conclusions

In summary, we report the design, fabrication and calibration of a micro-fuel cell sensor and improvement in its calibration by employing a multivariate analysis. This study addresses an enduring problem in the biosensing field — the importance of eliminating interfering signals toward the precise detection of VOCs in a multivariate environment. Initially, this approach has been demonstrated in vitro through the detection of alcohol, while eliminating the contribution of major interfering compounds (e.g. humidity) in a micro-fuel cell sensor system. This signal separation method is novel and significant for potential transdermal alcohol detection. However, many other VOCs exist in a multi-dimensional environment [238, 239, 240], which require more robust tools for the detection of sub-ppm/ppb level of measurements.

Hence, this work developed a fuel cell-based, wearable sensing platform, incorporating multivariate analysis methods to improve specificity and precision. The traditional linear regression method has limitations of signal overlap for the calibration of a fuel cell sensor. Multivariate calibration methods, such as PCR, establish an accurate relationship between a response variable (the concentration of analyte) and predictor variables (sub-nA currents) for estimating the response variable based on the values of the predictor variables. Therefore, PCR can contribute to eliminating the redundancy of the data sets and improving calibration based upon the new variables, which were derived from the principal components.

In this work, a complete wearable platform has been developed, capable of providing a comprehensive, low-power, high-accuracy, selective and easily sustainable electrochemical sensor. Moreover, this device has been implemented on human subjects for transdermal alcohol measurements and demonstrated 62% better accuracy compared to a commercial breathalyzer in an unstructured study. Due to limitations with blood sample collection, the unstructured study improved our confidence to move on to another VOC: anesthetic isoflurane detection. This study allowed us to control humidity and temperature in the operating theater. This also allowed control with the isoflurane delivery. By comparing to the gold-standard IR device present within the operation theater, our wearable fuel cell biosensor showed an average accuracy of ~14.29%. This shows that there is a potential to replace the rather large IR device with the wearable biosensor developed in this study.

Therefore, this work could lead to significant improvements in specific detection of VOCs. These improvements could be felt at point of care facilities during the rehabilitation processes and/or during the monitoring of various biomarkers and diseases.

7.2 Recommendations for future research

For the further improvement of VOC sensing with fuel cells, this work needs to improve in the following domains. They are:

1. A calibration chamber needs to be designed to execute and understand the fundamental relationship of relative humidity and temperature with the signals of different concentrations of specific VOC.

2. An integrated humidity sensor, temperature sensor and fuel cell sensor need to be fabricated in a single platform.
3. A prediction model can be derived from the large data sets [241], correlating humidity and temperature data, for the precise calibration of any analyte.

REFERENCES

1. Schwoebel, H.; Schubert, R.; Sklorz, M.; Kischkel, S.; Zimmermann, R.; Schubert, J. K.; Miekisch, W. Phase-Resolved Real-time Breath Analysis during Exercise by means of Smart Processing of PTR-MS Data. Anal. Bioanal. Chem. 2011, 401 (7), 2079–2091.

2. Shirasu, M.; Touhara, K. The Scent of Disease: Volatile Organic Compounds of the Human Body Related to Disease and Disorder. J. Biochem. 2011, 150 (3), 257–266.

3. de Lacy Costello, B.; Amann, A.; Al-Kateb, H.; Flynn, C.; Filipiak, W.; Khalid, T.; Osborne, D.; Ratcliffe, N. M. A Review of the Volatiles from the Healthy Human Body. J. Breath Res. 2014, 8 (1), 14001.

4. Mochalski, P.; Sponring, A.; King, J.; Unterkofler, K.; Troppmair, J.; Amann, A. Release and Uptake of Volatile Organic Compounds by Human Hepatocellular Carcinoma Cells (HepG2) in Vitro. Cancer Cell Int. 2013, 13 (1), 72.

5. Jalal, A. H.; Alam, F.; RoyChoudhury, S.; Umasankar, Y.; Pala, N.; Bhansali, S. Prospects and challenges of volatile organic compound sensors in human healthcare, ACS Sensors. 2018. 3 (7), 1246-1263.

6. Potera, C. Scented Products Emit a Bouquet of VOCs. Environ. Health Perspect. 2011, 119 (1), A16.

7. Phillips, M.; Herrera, J.; Krishnan, S.; Zain, M.; Greenberg, J.; Cataneo, R. N. Variation in Volatile Organic Compounds in the Breath of Normal Humans. J. Chromatogr. B Biomed. Sci. Appl. 1999, 729 (1–2), 75–88.

8. Filipiak, W.; Mochalski, P.; Filipiak, A.; Ager, C.; Cumeras, R.; Davis, C. E.; Agapiou, A.; Unterkofler, K.; Troppmair, J. A Compendium of Volatile Organic Compounds (VOCs) Released By Human Cell Lines. Curr. Med. Chem. 2016, 23 (20), 2112–2131.

9. Program, N. R. C. (US) C. on R. and E. of the A. C. S. D. Occupational Health and Workplace Monitoring at Chemical Agent Disposal Facilities; National Academies Press (US), 2001.

10. Mason, M. F.; Dubowski, K. M. Alcohol, Traffic, and Chemical Testing in the United States: A Résumé and Some Remaining Problems. Clin. Chem. 1974, 20 (2), 126 – 140.

11. Jalal, A. H.; Umasankar, Y.; Chowdhury, M.; Bhansali, S. A Fuel Cell Based Sensing Platform for Selective Detection of Acetone in Hyperglycemic Patients. ECS Trans. 2017, 80 (10), 1369–1378.

12. Opitz, P.; Herbarth, O. The volatilome – investigation of volatile organic metabolites (VOM) as potential tumor markers in patients with head and neck squamous cell carcinoma (HNSCC). J. of Otolaryngology – Head and Neck Surgery. 2018, 47 (42), 1 – 13.

13. Jones, A. W. Measuring Alcohol in Blood and Breath for Forensic Purposes - A Historical Review. Forensic Sci. Rev. 1996, 8 (1), 13–44.

14. Borkenstein, R. F.; Smith, H. W. The Breathalyzer and Its Applications. Med. Sci. Law 1961, 2 (1), 13–22.

15. Saidi, T.; Zaim, O.; Moufid, M.; El Bari, N.; Ionescu, R.; Bouchikhi, B. Exhaled Breath Analysis Using Electronic Nose and Gas Chromatography–mass Spectrometry for Non-Invasive Diagnosis of Chronic Kidney Disease, Diabetes Mellitus and Healthy Subjects. Sensors Actuators B Chem. 2018, 257, 178–188.

16. Agbroko, S. O.; Covington, J. A Novel, Low-Cost, Portable PID Sensor for Detection of VOC. Proceedings 2017, 1 (4), 482.

17. Salomaa, E.-R.; Sällinen, S.; Hiekkanen, H.; Liippo, K. Delays in the Diagnosis and Treatment of Lung Cancer. Chest 2005, 128 (4), 2282–2288.

18. Tricoli, A.; Nasiri, N.; De, S. Wearable and Miniaturized Sensor Technologies for Personalized and Preventive Medicine. Adv. Funct. Mater. 2017, 27 (15), 1605271.

19. Brattoli, M.; Cisternino, E.; Dambruoso, P. R.; de Gennaro, G.; Giungato, P.; Mazzone, A.; Palmisani, J.; Tutino, M. Gas Chromatography Analysis with Olfactometric Detection (GC-O) as a Useful Methodology for Chemical Characterization of Odorous Compounds. Sensors (Basel). 2013, 13 (12), 16759–16800.

20. Lindinger, W.; Jordan, A. Proton-Transfer-Reaction Mass Spectrometry (PTR–MS): On-Line Monitoring of Volatile Organic Compounds at Pptv Levels. Chem. Soc. Rev. 1998, 27 (5), 347.

21. Španěl, P.; Smith, D. Selected Ion Flow Tube Mass Spectrometry for On-Line Trace Gas Analysis in Biology and Medicine. Eur. J. Mass Spectrom. 2007, 13 (1), 77–82.

22. Wang, C.; Sahay, P. Breath Analysis Using Laser Spectroscopic Techniques: Breath Biomarkers, Spectral Fingerprints, and Detection Limits. Sensors 2009, 9 (10), 8230–8262.

23. Gloess, A. N.; Yeretzian, C.; Knochenmuss, R.; Groessl, M. On-Line Analysis of Coffee Roasting with Ion Mobility Spectrometry–mass Spectrometry (IMS–MS). Int. J. Mass Spectrom. 2018, 424, 49–57.

24. Kadir, R. A.; Rani, R. A.; Zoolfakar, A. S.; Ou, J. Z.; Shafiei, M.; Wlodarski, W.; Kalantar-zadeh, K. Nb2O5 Schottky Based Ethanol Vapour Sensors: Effect of Metallic Catalysts. Sensors Actuators B Chem. 2014, 202, 74–82.

25. Kim, H.-J.; Lee, J.-H. Highly Sensitive and Selective Gas Sensors Using P-Type Oxide Semiconductors: Overview. Sensors Actuators B Chem. 2014, 192, 607–627.

26. Devkota, J.; Ohodnicki, P. R.; Greve, D. W. SAW Sensors for Chemical Vapors and Gases. Sensors (Basel). 2017, 17(4), 1-28.

27. Semwal, V.; Shrivastav, A. M.; Verma, R.; Gupta, B. D. Surface Plasmon Resonance Based Fiber Optic Ethanol Sensor Using Layers of Silver/silicon/hydrogel Entrapped with ADH/NAD. Sensors Actuators B Chem. 2016, 230, 485–492.

28. Jalal, A. H.; Umasankar, Y.; Bhansali, S. Development and Characterization of Fuel Cell Sensor for Potential Transdermal Ethanol Sensing. ECS Trans. 2016, 72 (31), 25–31.

29. Kim, N.-H.; Choi, S.-J.; Yang, D.-J.; Bae, J.; Park, J.; Kim, I.-D. Highly Sensitive and Selective Hydrogen Sulfide and Toluene Sensors Using Pd Functionalized WO3 Nanofibers for Potential Diagnosis of Halitosis and Lung Cancer. Sensors Actuators B Chem. 2014, 193, 574–581.

30. Vishinkin, R.; Haick, H. Nanoscale Sensor Technologies for Disease Detection via Volatolomics. Small 2015, 11 (46), 6142–6164.

31. Broza Y. Y., Haick H. Nanomaterial-based sensors for Detection of Disease by Volatile Organic Compounds, Nanomedicine. 2013, 8(5), 785-806.

32. Paska, Y.; Haick, H. Interactive Effect of Hysteresis and Surface Chemistry on Gated Silicon Nanowire Gas Sensors, ACS Appl. Mater. Interfaces, 2012, 4 (5), 2604–2617.

33. Jalal, A. H.; Umasankar, Y.; Gonzalez, P. J.; Alfonso, A.; Bhansali, S. Multimodal Technique to Eliminate Humidity Interference for Specific Detection of Ethanol. Biosens. and Bioelectron. 2017, 87, 522–530.

34. Romain, A. and Nicolas, J. Long term Stability of Metal Oxide-based Gas Sensors for E-nose Environmental Applications: An Overview, In AIP Conference Proceedings 1137, 2009, 443.

35. Dieffenderfer, J.; Goodell, H.; Mills, S.; McKnight, M.; Yao, S.; Lin, F.; Beppler, E.; Bent, B.; Lee, B.; Misra, V.; Zhu, Y.; Oralkan, O.; Strohmaier, J.; Muth, J.; Peden, D.; Bozkurt, A. Low Power Wearable Systems for Continuous Monitoring of Environment and Health for Chronic Respiratory Disease, IEEE J Biomed Health Inform., 2016, 20(5), 1251–1264.

36. Yao, S.; Swetha, P.; Zhu, Y. Nanomaterial-Enabled Wearable Sensors for Healthcare, Adv. Healthcare Mater. 2018, 1-27.

37. Pattar, S.; Buyya, R.; Venugopal, K. R.; Iyengar, S. S.; Patnaik, L. M. Searching for the IoT Resources: Fundamentals, Requirements, Comprehensive Review and Future Directions, IEEE Communications Surveys & Tutorials, 2018, 1-32.

38. Kim, S. J.; Choi, S. J.; Jang, J. S.; Cho, H. J.; Kim, I. D. Innovative Nanosensor for Disease Diagnosis. Accounts of Chem. Res., 50 (7), 2017, 1587–1596.

39. Delpha, C. ; Siadat, M.; Lumbreras, M. An Electronic Nose for the Identification of Forane R134a in an Air Conditioned Atmosphere. Sensors Actuators B, 2000, 69, 243–247.

40. Yang, J.; Acharya, R.; Zhu, X.;. Köse, M. E.; Schanze, K. S. Pyrophosphate Sensor Based on Principal Component Analysis of Conjugated Polyelectrolyte Fluorescence, ACS Omega, 2016, 1 (4), 648–655.

41. Jalal, A. H.; Alam, F.; Ahmed, A.; Ahad, M. A. Precise calibration of optical fiber sensor for ammonia sensing using multivariate analysis, SPIE Defense + Commercial Sensing. 2018, 10654, 106540W-1 – 106540W-7.

42. Amann, A.; Costello, B. de L.; Miekisch, W.; Schubert, J.; Buszewski, B.; Pleil, J.; Ratcliffe, N.; Risby, T. The Human Volatilome: Volatile Organic Compounds (VOCs) in Exhaled Breath, Skin Emanations, Urine, Feces and Saliva. J. Breath Res. 2014, 8 (3), 34001.

43. Broza, Y. Y.; Mochalski, P.; Ruzsanyi, V.; Amann, A.; Haick, H. Hybrid Volatolomics and Disease Detection. Angew. Chemie Int. Ed. 2015, 54 (38), 11036–11048.

44. Hajimiragha, H.; Ewers, U.; Brockhaus, A.; Boettger, A. Levels of Benzene and Other Volatile Aromatic Compounds in the Blood of Non-Smokers and Smokers. Int. Arch. Occup. Environ. Health 1989, 61 (8), 513–518.

45. Aggazzotti, G.; Fantuzzi, G.; Righi, E.; Predieri, G. Blood and Breath Analyses as Biological Indicators of Exposure to Trihalomethanes in Indoor Swimming Pools. Sci. Total Environ. 1998, 217 (1–2), 155–163.

46. Horvath, G.; Andersson, H.; Paulsson, G. Characteristic Odour in the Blood Reveals Ovarian Carcinoma. BMC Cancer 2010, 10 (1), 643.

47. Selyanchyn, R.; Nozoe, T.; Matsui, H.; Kadosawa, T.; Lee, S.-W. TD-GC-MS Investigation of the VOCs Released from Blood Plasma of Dogs with Cancer. Diagnostics (Basel, Switzerland) 2013, 3 (1), 68–83.

48. Liu, H.; Wang, H.; Li, C.; Wang, L.; Pan, Z.; Wang, L. Investigation of Volatile Organic Metabolites in Lung Cancer Pleural Effusions by Solid-Phase Microextraction and Gas Chromatography/mass Spectrometry. J. Chromatogr. B. Analyt. Technol. Biomed. Life Sci. 2014, 945–946, 53–59.

49. Lourdusamy, V.; Tharian, B.; Navaneethan, U. Biomarkers in Bile-Complementing Advanced Endoscopic Imaging in the Diagnosis of Indeterminate Biliary Strictures. World J. Gastrointest. Endosc. 2015, 7 (4), 308.

50. Tominaga, M.; Ishikawa, T.; Michiue, T.; Oritani, S.; Koide, I.; Kuramoto, Y.; Ogawa, M.; Maeda, H. Postmortem Analyses of Gaseous and Volatile Substances in Pericardial Fluid and Bone Marrow Aspirate. J. Anal. Toxicol. 2013, 37 (3), 147–151.

51. Bouatra, S.; Aziat, F.; Mandal, R.; Guo, A. C.; Wilson, M. R.; Knox, C.; Bjorndahl, T. C.; Krishnamurthy, R.; Saleem, F.; Liu, P.; Dame, Z. T.; Poelzer, J.; Huynh, J.; Yallou, F. S.; Psychogios, N.; Dong, E.; Bogumil, R.; Roehring, C.; Wishart, D. S. The Human Urine Metabolome. PLoS One 2013, 8 (9), e73076.

52. Prabhakar, A.; Quach, A.; Zhang, H.; Terrera, M.; Jackemeyer,D.; Xian, X.; Tsow, F.; Tao, N.; Forzani, E. S.; Acetone as Biomarker for ketosis Buildup Capability - A Study in Healthy Individuals Under Combined High Fat and Starvation Diets. Nutrition Journal 2015, 14 (41), 1–11.

53. McKee, H. C.; Rhoades, J. W.; Campbell, J.; Gross, A. L. Acetonitrile in Body Fluids Related to Smoking. Public Heal. reports (Washington, D.C. 1896) 1962, 77 (7), 553–554.

54. Wang, C.; Feng, Y.; Wang, M.; Pi, X.; Tong, H.; Wang, Y.; Zhu, L.; Li, E. Volatile Organic Metabolites Identify Patients with Mesangial Proliferative

Glomerulonephritis, IgA Nephropathy and Normal Controls. Sci. Rep. 2015, 5 (1), 14744.

55. Khalid, T.; Aggio, R.; White, P.; De Lacy Costello, B.; Persad, R.; Al-Kateb, H.; Jones, P.; Probert, C. S.; Ratcliffe, N. Urinary Volatile Organic Compounds for the Detection of Prostate Cancer. PLoS One 2015, 10 (11), e0143283.

56. Matsumura, K.; Opiekun, M.; Oka, H.; Vachani, A.; Albelda, S. M.; Yamazaki, K.; Beauchamp, G. K. Urinary Volatile Compounds as Biomarkers for Lung Cancer: A Proof of Principle Study Using Odor Signatures in Mouse Models of Lung Cancer. PLoS One 2010, 5 (1), e8819.

57. Arasaradnam, R. P.; Westenbrink, E.; McFarlane, M. J.; Harbord, R.; Chambers, S.; O'Connell, N.; Bailey, C.; Nwokolo, C. U.; Bardhan, K. D.; Savage, R.; Covington, J. A. Differentiating Coeliac Disease from Irritable Bowel Syndrome by Urinary Volatile Organic Compound Analysis – A Pilot Study. PLoS One 2014, 9 (10), e107312.

58. Banday, K. M.; Pasikanti, K. K.; Chan, E. C.; Singla R.; Rao, K. V.; Chauhan, V. S.; Nanda, R. K. Use of Urine Volatile Organic Compounds to Discriminate Tuberculosis Patients from Healthy Subjects. Anal Chem. 2011, 83 (14), 5526-5534.

59. Soini, H. A.; Klouckova, I.; Wiesler, D.; Oberzaucher, E.; Grammer, K.; Dixon, S. J.; Xu, Y.; Brereton, R. G.; Penn, D. J.; Novotny, M. V. Analysis of Volatile Organic Compounds in Human Saliva by a Static Sorptive Extraction Method and Gas Chromatography-Mass Spectrometry. J. Chem. Ecol. 2010, 36 (9), 1035–1042.

60. Kim, J.; Imani, S.; de Araujo, W. R.; Warchall, J.; Valdés-Ramírez, G.; Paixão, T. R. L. C.; Mercier, P. P.; Wang, J. Wearable Salivary Uric Acid Mouthguard Biosensor with Integrated Wireless Electronics. Biosens. Bioelectron. 2015, 74, 1061–1068.

61. Gallagher, M.; Wysocki, C. J.; Leyden, J. J.; Spielman, A. I.; Sun, X.; Preti, G. Analyses of Volatile Organic Compounds from Human Skin. Br. J. Dermatol. 2008, 159 (4), 780–791.

62. Sanford, J. A.; Gallo, R. L. Functions of the Skin Microbiota in Health and Disease. Semin. Immunol. 2013, 25 (5), 370–377.

63. Gajjar, R. M.; Miller, M. A.; Kasting, G. B. Evaporation of Volatile Organic Compounds from Human Skin In Vitro. The Annals of Occupational Hygiene, 2013, 57 (7), 853–865.

64. Boman, A.; Maibach, H.I. Percutaneous Absorption of Organic Solvents. International Journal of Occupational and Environmental Health. 2013, 6, 93-95.

65. Fenske, J. D.; Paulson, S. E. Human Breath Emissions of VOCs. J. Air Waste Manage. Assoc. 1999, 49 (5), 594–598.

66. Wang, Z.; Wang, C. Is Breath Acetone a Biomarker of Diabetes? A Historical Review on Breath Acetone Measurements. J. Breath Res. 2013, 7 (3), 37109.

67. Tangerman, A.; Meuwese-Arends, M. T.; van Tongeren, J. H. A New Sensitive Assay for Measuring Volatile Sulphur Compounds in Human Breath by Tenax Trapping and Gas Chromatography and Its Application in Liver Cirrhosis. Clin. Chim. Acta. 1983, 130 (1), 103–110.

68. Boots, A. W.; Smolinska, A.; van Berkel, J. J. B. N.; Fijten, R. R. R.; Stobberingh, E. E.; Boumans, M. L. L.; Moonen, E. J.; Wouters, E. F. M.; Dallinga, J. W.; Van Schooten, F. J. Identification of Microorganisms Based on Headspace Analysis of Volatile Organic Compounds by Gas Chromatography–mass Spectrometry. J. Breath Res. 2014, 8 (2), 27106.

69. Mazzatenta, A.; Pokorski, M.; Sartucci, F.; Domenici, L.; Di Giulio, C. Volatile Organic Compounds (VOCs) Fingerprint of Alzheimer's Disease. Respir. Physiol. Neurobiol. 2015, 209, 81–84.

70. Singh, S.; Arcaroli, J.; Thompson, D. C.; Messersmith, W.; Vasiliou, V. Acetaldehyde and Retinaldehyde-Metabolizing Enzymes in Colon and Pancreatic Cancers. Adv. Exp. Med. Biol. 2015, 815, 281–294.

71. Gubler, D.; Device and Method of Using Volatile Organic Compounds That Affect Mood, Emotion or a Physiologic State. Patent Application US 2017/0173047 A1, 2016.

72. Pellizzari, E. D.; Hartwell, T. D.; Harris, B. S.; Waddell, R. D.; Whitaker, D. A.; Erickson, M. D. Purgeable Organic Compounds in Mother's Milk. Bull. Environ. Contam. Toxicol. 1982, 28 (3), 322–328.

73. DeBruin, L. S.; Pawliszyn, J. B.; Josephy, P. D. Detection of Monocyclic Aromatic Amines, Possible Mammary Carcinogens, in Human Milk. Chem. Res. Toxicol. 1999, 12 (1), 78–82.

74. Zhu, J.; Phillips, S. P.; Feng, Y. ; Yang, X. Phthalate Esters in Human Milk: Concentration Variations over a 6-Month Postpartum Time. Environ. Sci. Technol. 2006, 40, 5276-5281.

75. Hung, C.; Hung, I.; Yen, J.; Hwang, B.; Soong, W. Determination of Benzene and Alkylbenzenes in Milk by Purge and Trap Gas Chromatography. Toxicol. Environ. Chem. 1998, 67 (1–2), 1–7.

76. Meyer, M. R.; Maurer, H. H. Absorption, Distribution, Metabolism and Excretion Pharmacogenomics of Drugs of Abuse. Pharmacogenomics 2011, 12 (2), 215–233.

77. Turrens, J. F. Mitochondrial Formation of Reactive Oxygen Species. J. Physiol. 2003, 552 (2), 335–344.

78. Deleidi, M.; JÃ¤ggle, M.; Rubino, G. Immune Aging, Dysmetabolism, and Inflammation in Neurological Diseases. Front. Neurosci. 2015, 9, 172.

79. Haick, H.; Broza, Y. Y.; Mochalski, P.; Ruzsanyi, V.; Amann, A. Assessment, Origin, and Implementation of Breath Volatile Cancer Markers. Chem. Soc. Rev. 2014, 43 (5), 1423–1449.

80. Zakhari, S. Overview: How Is Alcohol Metabolized by the Body? Alcohol Research & Health.2006, 29 (4), 245-254.

81. Krishnan, K.; White, P. Pharmacokinetics and Toxicokinetics. In Haschek and Rousseaux's Handbook of Toxicologic Pathology; Elsevier, 2013; pp 39–59.

82. Buerk, D. G.; Saidel, G. M. Local Kinetics of Oxygen Metabolism in Brain and Liver Tissues. Microvasc. Res. 1978, 16 (3), 391–405.

83. Stücker, M.; Struk A.;Altmeyer P.; Herde M.;Baumgärtl H.;Lübbers D. W. The Cutaneous Uptake of Atmospheric Oxygen Contributes Significantly to the Oxygen Supply of Human Dermis and Epidermis. Journal of Physiology.2002, 538(3),985–994.

84. Maren, T. H. Principles of Drug Action. The Basis of Pharmacology. Avram Goldstein, Lewis Aronow, and Sumner M. Kalman. Harper and Row, New York, 1968. Xii + 884 Pp., Illus. $18.50. Science (80-.). 1969, 166 (3907), 858–858.

85. Hlastala, M. P. Physiological Errors Associated With Alcohol Breath Testing. the Champion, 1985, 16–19.

86. Jones, A. W. Physiological Aspects of Breath Alcohol Measurement. Alcohol, drugs and driving, 1990, 6 (2), 1–25.

87. King, J.; Unterkofler, K.; Teschl, G.; Teschl, S.; Koc, H.; Hinterhuber, H.; Amann, A. A Mathematical Model for Breath Gas Analysis of Volatile Organic Compounds with Special Emphasis on Acetone. J Math Biol. 2011, 63 (5), 959-999.

88. Wang, J.; Nuñovero, N.; Lin, Z.; Nidetz, R.; Buggaveeti, S.; Zhan, C.; Kurabayashi, K.; Steinecker, W. H.; Zellers, E. T. A Wearable MEMS Gas Chromatograph for Multi-Vapor Determinations. Procedia Engineering, 2016, 168, 1398 – 1401.

89. Khan, I.; Saeed, K.; Khan, I. Nanoparticles: Properties, Applications and Toxicities. Arabian J. of Chemistry, 2017, 1-24.

90. Mirzaei, A.; Leonardi, S. G.; Neri G. Detection of Hazardous Volatile Organic Compounds (VOCs) by Metal Oxide Nanostructures-based Gas Sensors: A Review. Ceramics International. 2016, 42, 15119–15141.

91. Li, B.; Sauve, G.; Iovu, M. C.; Jeffries-EL, M.; Zhang, R.; Cooper, J.; Santhanam, S.; Schultz, L.; Revelli, J. C.; Kusne, A. G.; Kowalewski, T.; Snyder, J. L.; Weiss, L. E.; Fedder, G. K.; McCullough, R. D.; Lambeth, D. N. Volatile Organic Compound Detection Using Nanostructured Copolymers. Nano Letters, 2006, 6 (8), 1598-1602.

92. Alam, F.; Jalal, A. H.; Sinha, R.; Umasankar, Y.; Bhansali, S.; Pala, N. Sonochemically Synthesized ZnO Nanostructure-based L-lactate Enzymatic Sensors on Flexible Substrates, MRS Advances. 2018, 3 (5), 277-282.

93. Han, L.; Shi, X.; Wu, W.; Kirk, F. L.; Luo, J.; Wang, L.; Mott, D.; Cousineau, L.; Lim, S. I.; Lu, S.; Zhong, C. Nanoparticle-structured Sensing Array Materials and Pattern Recognition for VOC Detection, Sensors and Actuators B. 2005, 106, 431–441.

94. Leidinger, M.; Rieger, M.; Weishaupt, D.; Sauerwald, T.; Nägele, M.; Hürttlen, J.; Schütze, A. Trace Gas VOC Detection Using Metal-Organic Frameworks as Preconcentrators and Semiconductor Gas Sensors, Procedia Engineering. 2015. 120, 1042 – 1045.

95. Jalal, A. H.; Yu, J.; Agwu Nnanna, A. G. Fabrication and Calibration of Oxazine-Based Optic Fiber Sensor for Detection of Ammonia in Water. Appl. Opt. 2012, 51 (17), 3768 – 3775.

96. Mu, X. Wearable Gas Sensor Microsystem for Personal Healthcare and Environmental Monitoring. Thesis, Michigan State University, 2013, 1–134.

97. Pasha, S. K.; Jalal, A. H.; Singh, A.; Bhansali, S. Chapter 1: Nanobiotechnology: An Abrupt Merger. In Nanobiotechnology for Sensing Applications; Apple Academic Press Inc., 2016, pp 1–42.

98. RoyChoudhury, S.; Rawat, V.; Jalal, A. H.; Kale, S. N.; Bhansali, S. Recent Advances in Metamaterial Split-ring-resonator Circuits as Biosensors and Therapeutic Agents. Biosensors and Bioelectronics, 2016, 86, 595–608.

99. Bingham, J. M.; Anker, J. N.; Kreno, L. E.; Van Duyne R. P. Gas Sensing with High-Resolution Localized Surface Plasmon Resonance Spectroscopy. J. Am. Chem. Soc. 2010. 132 (49), 17358–17359.

100. Homola, J. Present and Future of Surface Plasmon Resonance Biosensor. Anal Bioanal Chem. 2003. 377, 528–539.

101. Homola, J. Surface Plasmon Resonance Sensors for Detection of Chemical and Biological Species. Chem. Rev. 2008. 108, 462−493.

102. Cheng, C.; Chen, Y.; Lu, C. Organic Vapour Sensing Using Localized Surface Plasmon Resonance Spectrum of Metallic Nanoparticles Self Assemble Monolayer. Talanta. 2007. 73, 358–365.

103. Chen, Y.; Lu, C. Surface Modification on Silver Nanoparticles for Enhancing Vapor Selectivity of Localized Surface Plasmon Resonance Sensors. Sensors and Actuators B, 2009. 135, 492–498.

104. Iitani, K.; Chien, P.; Suzuki, T.; Toma, K.; Arakawa, T.; Iwasaki, Y.; Mitsubayashi, K. Fiber-Optic Bio-sniffer (Biochemical Gas Sensor) Using Reverse Reaction of Alcohol Dehydrogenase for Exhaled Acetaldehyde. ACS Sens. 2018, 3, 425−431.

105. Brooks, P. J.; Enoch, M. A.; Goldman, D.; Li, T. K.; Yokoyama, A. The Alcohol Flushing Response: An Unrecognized Risk Factor for Esophageal Cancer from Alcohol Consumption. PLoS Med. 2009, 6, 0258−0263.

106. Reddy, K.; Guo, Y.; Liu, J.; Lee, W.; Khaing Oo, M. K.; Fan, X. Rapid, Sensitive, and Multiplexed on-Chip Optical Sensors for Micro-Gas Chromatography. Lab Chip 2012, 12 (5), 901.

107. Scholten, K.; Collin, W. R.; Fan, X.; Zellers, E. T. Nanoparticle-coated Micro-optofluidic Ring Resonator as a Detector for Microscale Gas Chromatographic Vapor Analysis. Nanoscale, 2015, 7, 9282–9289.

108. Mazzone, P. J.; Wang, X.; Xu, Y.; Mekhail, T.; Beukemann, M. C.; Na, J.; Kemling, J. W.; Suslick, K. S.; Sasidhar, M. Exhaled Breath Analysis with a Colorimetric Sensor Array for the Identification and Characterization of Lung Cancer. J Thorac Oncol. 2012, 7(1), 137–142.

109. Prabhakar, A.; Iglesias, R. A.; Shan, X.; Xian, X.; Zhang, L.; Tsow, F.; Forzani, E. S.; Tao, N. Online Sample Conditioning for Portable Breath Analyzers. Anal. Chem. 2012, 84 (16), 7172–7178.

110. Lakkis, S.; Younes, R.; Alayli, Y.; Sawan, M. Review of Recent Trends in Gas Sensing Technologies and Their Miniaturization Potential. Sens. Rev. 2014, 34 (1), 24–35.

111. Kanan, S. M.; El-Kadri, O. M.; Abu-Yousef, I. A.; Kanan, M. C. Semiconducting Metal Oxide Based Sensors for Selective Gas Pollutant Detection. Sensors 2009, 9 (10), 8158–8196.

112. Krivec, M.; Gunnigle, G.; Abram, A.; Maier, D.; Waldner, R.; Gostner, J.; Überall, F.; Leitner, R. Quantitative Ethylene Measurements with MOx Chemi-resistive Sensors at Different Relative Air Humidities. Sensors 2015, 15 (11), 28088–28098.

113. Itoh, T.; Matsubara, I.; Kadosaki, M.; Sakai, Y.; Shin, W.; Izu, N.; Nishibori, M. Effects of High-Humidity Aging on Platinum, Palladium, and Gold Loaded Tin Oxide--Volatile Organic Compound Sensors. Sensors (Basel). 2010, 10 (7), 6513–6521.

114. Xu, X.; Wang, J.; Long, Y. Zeolite-Based Materials for Gas Sensors. Sensors 2006, 6 (12), 1751–1764.

115. Rodríguez-González, L.; Franke, M. E.; Simon, U. Electrical Detection of Different Amines with Proton-Conductive H-ZSM-5. Stud. Surf. Sci. Catal. 2005, 158, 2049–2056.

116. Song, X.; Wang, Z.; Liu, Y.; Wang, C.; Li, L. A Highly Sensitive Ethanol Sensor Based on Mesoporous ZnO–SnO_2 Nanofibers. Nanotechnology 2009, 20 (7), 75501.

117. Choi, S.-J.; Lee, I.; Jang, B.-H.; Youn, D.-Y.; Ryu, W.-H.; Park, C. O.; Kim, I.-D. Selective Diagnosis of Diabetes Using Pt-Functionalized WO3 Hemitube Networks As a Sensing Layer of Acetone in Exhaled Breath. Anal. Chem. 2013, 85 (3), 1792–1796.

118. Righettoni, M.; Amann, A.; Pratsinis, S. E. Breath Analysis by Nanostructured Metal Oxides as Chemo-resistive Gas Sensors. Materials Today. 2015, 18 (3), 163–171.

119. Fioravanti, A.; Morandi, S.; Carotta, M. C. Chemoresistive Gas Sensors for Sub-ppm Acetone Detection. Procedia Eng. 2016, 168, 485–488.

120. Liu, J.; Wang, X.; Peng, Q.; Li, Y. Vanadium Pentoxide Nanobelts: Highly Selective and Stable Ethanol Sensor Materials. Adv. Mater. 2005, 17 (6), 764–767.

121. Wang, C.; Yin, L.; Zhang, L.; Xiang, D.; Gao, R. Metal Oxide Gas Sensors: Sensitivity and Influencing Factors. Sensors 2010, 10 (3), 2088–2106.

122. Cao, M.; Wang, Y.; Chen, T.; Antonietti, M.; Niederberger, M. A Highly Sensitive and Fast-Responding Ethanol Sensor Based on $CdIn_2O_4$ Nanocrystals Synthesized by a Nonaqueous Sol−Gel Route. Chem. Mater. 2008, 20 (18), 5781–5786.

123. Tayebi, N.; Su, X. Sensitive and Selective gas/VOC Detection Using MOS Sensor Array for Wearable and Mobile Applications. In 2017 ISOCS/IEEE International Symposium on Olfaction and Electronic Nose (ISOEN); IEEE, 2017; pp 1–3.

124. Yan, S.; Liu, X.; Skeete, Z.; He, N.; Xie, Z.-H.; Zhao, W.; Lombardi, J. P.; Liu, K.; Kang, N.; Luo, J.; Hsiao, B. S.; Poliks, M.; Gitsov, I.; Zhong, C.-J. Decoration of Nanofibrous Paper Chemiresistors with Dendronized Nanoparticles toward Structurally Tunable Negative-Going Response Characteristics to Human Breathing and Sweating. Adv. Mater. Interfaces 2017, 4 (22), 1700380.

125. Kim, I.-D.; Choi, S.-J.; Kim, S.-J.; Jang, J.-S. Exhaled Breath Sensors; In Smart Sensors for Health and Environment Monitoring, Springer Dordrecht, New York, 2015; pp 19–49.

126. Umasankar, Y.; Jalal, A. H.; Gonzalez, P. J.; Chowdhury, M.; Alfonso, A.; Bhansali, S. Wearable Alcohol Monitoring Device with Auto-Calibration Ability for High Chemical Specificity. In 2016 IEEE 13th International Conference on Wearable and Implantable Body Sensor Networks (BSN); IEEE, San Francisco, CA, 2016; pp 353–358.

127. Obermeier, J.; Trefz, P.; Wex, K.; Sabel, B.; Schubert, J. K.; Miekisch, W. Electrochemical Sensor System for Breath Analysis of Aldehydes, CO and NO. J. Breath Res. 2015, 9 (1), 16008.

128. Grossherr, M.; Hengstenberg, A.; Dibbelt, L.; Meier, T.; Gehring, H. Continuous Monitoring of Propofol Concentration in Expired Air During Artificial Ventilation in Patients: A Feasibility Study: 3AP3-8. European Journal of Anaesthesiology (EJA), 2008, 25, 33.

129. Swift, R. M.; Martin, C. S.; Swette, L.; LaConti, A.; Kackley, N. Studies on a Wearable, Electronic, Transdermal Alcohol Sensor. Alcohol. Clin. Exp. Res. 1992, 16 (4), 721–725.

130. Kim, J.; Jeerapan, I.; Imani, S.; Cho, T. N.; Bandodkar, A.; Cinti, S.; Mercier, P. P.; Wang, J. Noninvasive Alcohol Monitoring Using a Wearable

Tattoo-Based Iontophoretic-Biosensing System. ACS Sensors 2016, 1 (8), 1011–1019.

131. Mohan A. M. V., Windmiller J. R., Mishra R. K., Wang J. Continuous Minimally-invasive Alcohol Monitoring Using Microneedle Sensor Arrays. Biosens Bioelectron. 2017,91,574-579.

132. Tangerman, A.; Winkel, E. G. The Portable Gas Chromatograph OralChroma^{TM}: A Method of Choice to Detect Oral and Extra-Oral Halitosis. J. Breath Res. 2008, 2 (1), 17010.

133. Tanda, N.; Washio, J.; Ikawa, K.; Suzuki, K.; Koseki, T.; Iwakura, M. A New Portable Sulfide Monitor with a Zinc-Oxide Semiconductor Sensor for Daily Use and Field Study. J. Dent. 2007, 35 (7), 552–557.

134. Ponzoni, A.; Comini, E.; Sberveglieri, G.; Zhou, J.; Deng, S. Z.; Xu, N. S.; Ding, Y.; Wang, Z. L. Ultrasensitive and Highly Selective Gas Sensors Using Three-Dimensional Tungsten Oxide Nanowire Networks. Appl. Phys. Lett. 2006, 88 (20), 203101.

135. Kim, J. G.; Kim, Y. J.; Yoo, S. H.; Lee, S. J.; Chung, J. W.; Kim, M. H.; Park, D. K.; Hahm, K.-B. Halimeter ppb Levels as the Predictor of Erosive Gastroesophageal Reflux Disease. Gut Liver 2010, 4 (3), 320–325.

136. Choi, S.-J.; Kim, M. P.; Lee, S.-J.; Kim, B. J.; Kim, I.-D. Facile Au Catalyst Loading on the Inner Shell of Hollow SnO_2 Spheres Using Au-Decorated Block Copolymer Sphere Templates and Their Selective H_2S Sensing Characteristics. Nanoscale. 2014, 6 (20), 11898–11903.

137. Dong, K.-Y.; Choi, J.-K.; Hwang, I.-S.; Lee, J.-W.; Kang, B. H.; Ham, D.-J.; Lee, J.-H.; Ju, B.-K. Enhanced H_2S Sensing Characteristics of Pt Doped SnO_2 Nanofibers Sensors with Micro Heater. Sensors Actuators B Chem. 2011, 157 (1), 154–161.

138. Shin, J.; Choi, S.-J.; Youn, D.-Y.; Kim, I.-D. Exhaled VOCs Sensing Properties of WO3 Nanofibers Functionalized by Pt and IrO_2 Nanoparticles for Diagnosis of Diabetes and Halitosis. J. Electroceramics 2012, 29 (2), 106–116.

139. Choi, S.-J.; Fuchs, F.; Demadrille, R.; Grévin, B.; Jang, B.-H.; Lee, S.-J.; Lee, J.-H.; Tuller, H. L.; Kim, I.-D. Fast Responding Exhaled-Breath Sensors Using WO_3 Hemitubes Functionalized by Graphene-Based Electronic Sensitizers for Diagnosis of Diseases. ACS Appl. Mater. Interfaces. 2014, 6 (12), 9061–9070.

140. Choi, S.-J.; Jang, B.-H.; Lee, S.-J.; Min, B. K.; Rothschild, A.; Kim, I.-D. Selective Detection of Acetone and Hydrogen Sulfide for the Diagnosis of Diabetes

and Halitosis Using SnO 2 Nanofibers Functionalized with Reduced Graphene Oxide Nanosheets. ACS Appl. Mater. Interfaces. 2014, 6 (4), 2588–2597.

141. Choi, S.-J.; Lee, I.; Jang, B.-H.; Youn, D.-Y.; Ryu, W.-H.; Park, C. O.; Kim, I.-D. Selective Diagnosis of Diabetes Using Pt-Functionalized WO_3 Hemitube Networks As a Sensing Layer of Acetone in Exhaled Breath. Anal. Chem. 2013, 85 (3), 1792–1796.

142. Xiao, Y.; Lu, L.; Zhang, A.; Zhang, Y.; Sun, L.; Huo, L.; Li, F. Highly Enhanced Acetone Sensing Performances of Porous and Single Crystalline ZnO Nanosheets: High Percentage of Exposed (100) Facets Working Together with Surface Modification with Pd Nanoparticles. ACS Appl. Mater. Interfaces 2012, 4 (8), 3797–3804.

143. Gunawan, P.; Mei, L.; Teo, J.; Ma, J.; Highfield, J.; Li, Q.; Zhong, Z. Ultrahigh Sensitivity of Au/1D α-Fe_2O_3 to Acetone and the Sensing Mechanism. Langmuir. 2012, 28 (39), 14090–14099.

144. Righettoni, M.; Tricoli, A.; Pratsinis, S. E. Si:WO_3 Sensors for Highly Selective Detection of Acetone for Easy Diagnosis of Diabetes by Breath Analysis. Anal. Chem. 2010, 82 (9), 3581–3587.

145. Xiao, T.; Wang, X.-Y.; Zhao, Z.-H.; Li, L.; Zhang, L.; Yao, H.-C.; Wang, J.-S.; Li, Z.-J. Highly Sensitive and Selective Acetone Sensor Based on C-Doped WO3 for Potential Diagnosis of Diabetes Mellitus. Sensors Actuators B Chem. 2014, 199, 210–219.

146. Shin, J.; Choi, S.-J.; Lee, I.; Youn, D.-Y.; Park, C. O.; Lee, J.-H.; Tuller, H. L.; Kim, I.-D. Thin-Wall Assembled SnO 2 Fibers Functionalized by Catalytic Pt Nanoparticles and Their Superior Exhaled-Breath-Sensing Properties for the Diagnosis of Diabetes. Adv. Funct. Mater. 2013, 23 (19), 2357–2367.

147. Shi, J.; Hu, G.; Sun, Y.; Geng, M.; Wu, J.; Liu, Y.; Ge, M.; Tao, J.; Cao, M.; Dai, N. WO_3 Nanocrystals: Synthesis and Application in Highly Sensitive Detection of Acetone. Sensors Actuators B Chem. 2011, 156 (2), 820–824.

148. Jian, R.-S.; Sung, L.-Y.; Lu, C.-J. Measuring Real-Time Concentration Trends of Individual VOC in an Elementary School Using a Sub-ppb Detection μGC and a Single GC-MS Analysis. Chemosphere 2014, 99, 261–266.

149. Peng, F.; Luoa, T.; Yuan, Y.; Qiu, L. Performance of Optimized TVOCs Sensor. Procedia Eng. 2010, 7, 392–398.

150. Peng, F. M.; Xie, P. H.; Shi, Y. G.; Wang, J. D.; Liu, W. Q.; Li, H. Y. Photoionization Detector for Portable Rapid GC. Chromatographia. 2007, 65 (5–6), 331–336.

151. Phillips, M.; Sabas, M.; Greenberg, J. Increased Pentane and Carbon Disulfide in the Breath of Patients with Schizophrenia. J. Clin. Pathol. 1993, 46 (9), 861–864.

152. Phillips, M.; Cataneo, R. N.; Ditkoff, B. A.; Fisher, P.; Greenberg, J.; Gunawardena, R.; Kwon, C. S.; Tietje, O.; Wong, C. Prediction of Breast Cancer Using Volatile Biomarkers in the Breath. Prediction of Breast Cancer Using Volatile Biomarkers in the Breath. Breast Cancer Res. Treat. 2006, 99 (1), 19–21.

153. Roller, C.; Kosterev, A. A.; Tittel, F. K.; Uehara, K.; Gmachl, C.; Sivco, D. L. Carbonyl Sulfide Detection with a Thermoelectrically Cooled Midinfrared Quantum Cascade Laser. Opt. Lett. 2003, 28 (21), 2052–2054.

154. Van Hieu, N.; Kim, H.-R.; Ju, B.-K.; Lee, J.-H. Enhanced Performance of SnO_2 Nanowires Ethanol Sensor by Functionalizing with La_2O_3. Sensors Actuators B Chem. 2008, 133 (1), 228–234.

155. Gouma, P.-I.; Wang, L.; Simon, S.; Stanacevic, M. Novel Isoprene Sensor for a Flu Virus Breath Monitor. Sensors 2017, 17 (1), 199.

156. Grossherr, M.; Hengstenberg, A.; Meier, T.; Dibbelt, L.; Igl, B. W.; Ziegler, A.; Schmucker, P.; Gehring, H. Propofol Concentration in Exhaled Air and Arterial Plasma in Mechanically Ventilated Patients Undergoing Cardiac Surgery. Br. J. Anaesth. 2009, 102 (5), 608–613.

157. Kim, S.-S.; Young, C.; Vidakovic, B.; Gabram-Mendola, S. G. A.; Bayer, C. W.; Mizaikoff, B. Potential and Challenges for Mid-Infrared Sensors in Breath Diagnostics. IEEE Sens. J. 2010, 10 (1), 145–158.

158. Jian, R.-S.; Sung, L.-Y.; Lu, C.-J. Measuring Real-Time Concentration Trends of Individual VOC in an Elementary School Using a Sub-Ppb Detection μGC and a Single GC–MS Analysis. Chemosphere 2014, 99, 261–266.

159. Bur, C.; Andersson, M. E.; Lloyd Spetz, A.; Schutze, A. Detecting Volatile Organic Compounds in the Ppb Range With Gas Sensitive Platinum Gate SiC-Field Effect Transistors. IEEE Sens. J. 2014, 14 (9), 3221–3228.

160. Barsan, N.; Weimar, U. Conduction Model of Metal Oxide Gas Sensors. J. Electroceramics 2001, 7 (3), 143–167.

161. Kida, T.; Suematsu, K.; Hara, K.; Kanie, K.; Muramatsu, A. Ultrasensitive Detection of Volatile Organic Compounds by a Pore Tuning Approach Using Anisotropically Shaped SnO2 Nanocrystals. ACS Appl. Mater. Interfaces 2016, 8 (51), 35485–35495.

162. Marques, P. R.; McKnight, A. S. Field and Laboratory Alcohol Detection With 2 Types of Transdermal Devices. Alcohol. Clin. Exp. Res. 2009, 33 (4), 703–711.

163. Vaddiraju, S.; Gleason, K. K. Selective Sensing of Volatile Organic Compounds Using Novel Conducting Polymer–metal Nanoparticle Hybrids. Nanotechnology 2010, 21 (12), 125503.

164. Huang, G. G; Wang, C.; Tang, H.; Huang, Y.; Yang, J. ZnO Nanoparticle-Modified Infrared Internal Reflection Elements for Selective Detection of Volatile Organic Compounds. Anal. Chem., 2006, 78 (7), 2397–2404.

165. Segev-Bar, M.; Haick, H. Flexible Sensors Based on Nanoparticles. ACS Nano 2013, 7 (10), 8366–8378.

166. Zhang, Y.; Zheng, Z.; Yang, F. Highly Sensitive and Selective Alcohol Sensors Based on Ag-Doped In_2O_3 Coating. Ind. Eng. Chem. Res. 2010, 49 (8), 3539–3543.

167. Zhao, S.; Sin, J. K. O.; Xu, B.; Zhao, M.; Peng, Z.; Cai, H. A High Performance Ethanol Sensor Based on Field-Effect Transistor Using a $LaFeO_3$ Nano-Crystalline Thin-Film as a Gate Electrode. Sensors Actuators B Chem. 2000, 64 (1–3), 83–87.

168. Paska, Y.; Stelzner, T.; Christiansen, S.; Haick, H. Enhanced Sensing of Nonpolar Volatile Organic Compounds by Silicon Nanowire Field Effect Transistors. ACS Nano 2011, 5 (7), 5620–5626.

169. Leidinger, M.; Huotari, J.; Sauerwald, T.; Lappalainen, J.; Schütze, A. Selective Detection of Naphthalene with Nanostructured WO3 Gas Sensors Prepared by Pulsed Laser Deposition. J. Sensors Sens. Syst. 2016, 5 (1), 147–156.

170. Reimann, P.; Dausend, A.; Darsch, S.; Schüler, M.; Schütze; A. Improving MOS Virtual Multisensor Systems by Combining Temperature Cycled Operation with Impedance Spectroscopy. AIP Conference Proceedings 1362, 249, 2011.

171. Kim, E.; Lee, S.; Kim, J.; Kim, C.; Byun, Y.; Kim, H.; Lee, T. Pattern Recognition for Selective Odor Detection with Gas Sensor Arrays. Sensors 2012, 12 (12), 16262–16273.

172. Parvez, Imtiaz; Jamei, Mahdi; Sundararajan, Aditya; Sarwat, A. I.. RSS based loop-free compass routing protocol for data communication in advanced metering infrastructure (AMI) of Smart Grid. In Computational Intelligence Applications in Smart Grid (CIASG), 2014 IEEE Symposium on, pp. 1-6. IEEE, 2014.

173. Sriyananda, M. G. S.; Parvez, Imtiaz; Güvenç, Ismail; Bennis, Mehdi; Sarwat, A. I. Multi-armed bandit for LTE-U and WiFi coexistence in unlicensed bands." In WCNC, pp. 1-6. 2016.

174. Parvez, Imtiaz; Sarwat, A. I.; Wei, L.; Sundararajan; A. Securing metering infrastructure of smart grid: A machine learning and localization based key management approach.Energies. 2016. 9 (9), 691.

175. Parvez, Imtiaz; Sriyananda, M. G. S.; Guvenc, Ismail; Bennis, Mehdi; Sarwat, A. I. CBRS Spectrum Sharing between LTE-U and WiFi: A Multiarmed Bandit Approach. 2016.

176. Jalal, A. H.; Umasankar, Y.; Christopher, F.; Pretto, E. A.; Bhansali , S. A Model for Safe Transport of Critical Patients in Unmanned Drones with a 'Watch' Style Continuous Anesthesia Sensor, J. of Electrochem. Soc. 2018, 165 (8), B3071 – B3077.

177. Machado, R. F.; Laskowski, D.; Deffenderfer, O. Burch, T.; Zheng, S.; Mazzone, P. J.; Mekhail, T.; Jennings, C.; Stoller, J. K.; Pyle, J.; Duncan, J.; Dweik, R. A.; Erzurum, S. C. Detection of Lung Cancer by Sensor Array Analyses of Exhaled Breath. Am. J. Respir. Crit. Care Med. 2005, 171, 1286–1291.

178. Phillips, M.; Cataneo, R. N.; Ditkoff, B. A.; Fisher, P.; Greenberg, J.; Gunawardena, R.; Kwon, C. S.; Tietje, O.; Wong, C. Prediction of Breast Cancer Using Volatile Biomarkers in the Breath. Breast Cancer Res. Treat. 2006, 99 (1), 19–21.

179. Potyrailo, R. A. Bio-Inspired Device Offers New Model for Vapor Sensing. SPIE Newsroom, 2011, 1-2.

180. Korotcenkov, G.; Cho, B. K. Instability of Metal Oxide-Based Conductometric Gas Sensors and Approaches to Stability Improvement (Short Survey). Sensors Actuators B. 2011, 156 (2), 527–538.

181. Heikenfeld, J.; Jajack, A.; Rogers, J.; Gutruf, P; Tian, L.; Pan, T.; Li, R.; Khine, M.; Kim, J.; Wang, J.; Kim, J. Wearable Sensors: Modalities, Challenges, and Prospects. Lab Chip. 2018, 18, 217-248.

182. Deng,Y.; Liu, N. Y.; Tsow,F.; Xian, X.; Forzani, E. S. Adsorption Thermodynamic Analysis of a Quartz Tuning Fork Based Sensor for Volatile Organic Compounds Detection. ACS Sens. 2017, 2, 1662-1668.

183. Nguyen, S. T.; Lee, J-M.; Yang, Y. and Wang, X. Excellent Durability of Substoichiometric Titanium Oxide as a Catalyst Support for Pd in Alkaline Direct Ethanol Fuel Cells. Ind. Eng. Chem. Res., 2012, 51 (30), 9966–9972.

184. Hong, S.; Hou, M.; Zhang, H.; Jiang, Y.; Shao, Z.; Yi, B. A High-Performance PEM Fuel Cell with Ultralow Platinum Electrode via Electrospinning and Underpotential Deposition. Electrochimica Acta, 2017, 245, 403-409.

185. Parvez, Imtiaz; Khan, Tanwir; Sarwat, A. I.; Parvez Z. Laa-lte and wifi based smart grid metering infrastructure in 3.5 ghz band." In Humanitarian Technology Conference (R10-HTC), 2017 IEEE Region 10, pp. 151-155. IEEE, 2017.

186. Parvez, Imtiaz; Sarwat, A. I.; Pinto, J.; Parvez, Z.; Khandaker, M. A. A gossip algorithm based clock synchronization scheme for smart grid applications. In Power Symposium (NAPS), 2017 North American, pp. 1-6. IEEE, 2017.

187. Parvez, Imtiaz; Islam, N.; Rupasinghe, N.; Sarwat, A. I.; Güvenç; I. LAA-based LTE and ZigBee coexistence for unlicensed-band smart grid communications." In SoutheastCon, 2016, pp. 1-6. IEEE, 2016.

188. Parvez, Imtiaz; Rahmati, A.; Guvenc, I.; Sarwat, A. I.; Dai, H. A survey on low latency towards 5G: RAN, core network and caching solutions. IEEE Communications Surveys & Tutorials, 2018.

189. Sarwat, A. I.; Sundararajan, A.; Parvez, I.; Moghaddami, M.; Moghadasi, A. Toward a Smart City of Interdependent Critical Infrastructure Networks. In Sustainable Interdependent Networks, pp. 21-45. Springer, Cham, 2018.

190. Zhang, L.; Tian, F.; Kadri, C.; Xiao, B.; Li, H.; Pan, L.; Zhou, H. On-line Sensor Calibration Transfer Among Electronic Nose Instruments for Monitoring Volatile Organic Chemicals in Indoor Air quality. Sensors and Actuators B, 2011, 160, 899–909.

191. Simpson, G. Accuracy and Precision of Breath-Alcohol Measurements for a Random Subject in the Post absorptive State. Clin. Chem. 1987, 33 (2), 261-268.

192. Feroldi, D.; Basualdo, M. Description of PEM Fuel Cells System. 2012, 49 – 72.

193. Kuo, C.; Lin, C.; Lai, G.; Chen, Y.; Chang, Y.; Wu, W. Mat. Trans., 2007, 48(9), 2319.

194. Dini, J. W. Plating on Invar, VascoMax C-200, and 440C stainless steel. Surface and Coatings Tech.. 1996, 78, 14-18.

195. Watts, O. P. Rapid Nickel Plating. Am. Electrochem. Soc., Trans. 1916, 29, 395-400.

196. Geng, J.; Jefferson D. A.; Johnson, F. G. The unusual nanostructure of nickel–boron catalyst, *Chem. Comm.*, 2007**,** (9), 969.

197. Theivasanthi, T.; Alagar M. Nano sized copper particles by electrolytic synthesis and characterizations, *Int. J. of the Phy. Sci.*, 2011, 6(15), 3662.

198. Kulikovsky, A. A.; Berg, P. Positioning of a reference electrode in a PEM fuel cell. J. of The Electrochem. Soc., 2015, 162 (8), F843–F848.

199. Jalal, A. H.; Roy, S.; Alam, F. Thermal cycling layer by layer dip coating method for oxazine formation on clad modified optical fiber core, *2014 IEEE Int.conf. on advances in elec. Engg. (ICAEE)*, Vellore, India, January 9-11, pp. 1 – 4.

200. Nnanna, A. G. A.; Jalal, A. H. Oxazine-based sensor for contaminants detection, fabrication method therefor, and uses thereof., Patent No. US 8,735,165 B2. 2014.

201. Sedesheva, Y. S., Ivanov, V. S., Wozniak, A. I., and Yegorov, A. S., Proton-Exchange membranes based on sulfonated polymers, Oriental J. of Chem., 2016, 32, 2283-2296.

202. Spiege, C., Mathematical modeling of polymer exchange membrane fuel cells, PhD dissertation, University of South Florida, 2008.

203. Cheah, M. J., Kevrekidis, I. G., and Benziger, J., Effect of interfacial water transport resistance on coupled proton and water transport across Nafion, J. Phys. Chem. B, 115, 10239–10250, 2011.

204. Choi, P., Jalani, N. H., and Datta, R., Thermodynamics and proton transport in Nafion, J. of The Electrochem. Soc., 152, 123-130, 2005.

205. Robertson, R.; Vanlaar, W.; Simpson, H. Continuous Transdermal Alcohol Monitoring: A Primer for Criminal Justice Professionals. The Traffic Injury Research Foundation. 2007, pp. 1 – 29.

206. Antolini, E., Catalysts for direct ethanol fuel cells. J. Power Sources 170, 1–12, 2007.

207. Friedl, J., Stimming, U., Model catalyst studies on hydrogen and ethanol oxidation for fuel cells. Electrochim. Acta 101, 41–58, 2013.

208. Goodman, R. A.; Mercy, J. A.; Loya, F.; Rosenberg, M. L.; Smith, J. C.; Allen, N. H.; Vargas, L.; Kolts, R. Alcohol use and interpersonal violence: alcohol detected in homicide victims. Am. J. Public Health, 1986, 76, 144–9.

209. Room, R.; Babor, T.; Rehm, J. Alcohol and public health. Lancet, 2005, 365, 519–530.

210.

211. Dubowski, K. M. Quality Assurance in Breath-Alcohol Analysis. J. Anal. Toxicol. 1994, 18, 306–311.

212. Polissar, N. L.; Suwanvijit, W.; Gullberg, R. G. The Accuracy of Handheld Pre-Arrest Breath Test Instruments as a Predictor of the Evidential Breath Alcohol Test Results. J. Forensic Sci. 2015, 60, 482–487.

213. Zuba, D. Accuracy and reliability of breath alcohol testing by handheld electrochemical analysers. Forensic Science International. 2008, 178 (2–3), e29-e33.

214. Sakai, J. T.; Mikulich-Gilbertson, S.K., Long, R.J., Crowley, T.J., 2006. Validity of transdermal alcohol monitoring: fixed and self-regulated dosing. Alcohol. Clin. Exp. Res. 30, 26–33.

215. Alam, F.; Sinha, R.; Jalal, A. H.; Manickam, P.; Vabbina, P. K.; Bhansali, S.; Pala, N. Sonochemically synthesized zinc oxide nanoflakes based electrochemical immunosensor for ethyl glucuronide (EtG) detection, ECS Transactions. 2017, 80 (10), 1287-1294.

216. Alam, F.; Jalal, A. H.; Sinha, R.; Umasankar, Y.; Bhansali, S.; Pala, N. ZnO nanoflakes-based mediator free flexible biosensors for the selective detection of ethyl glucuronide (EtG) and lactate, SPIE Defense + Commercial Sensing. 2018, 10639, 106392O-1 – 106392O-6.

217. Jadoon, S., Karim, S., Akram, M.R., Kalsoom Khan, A., Zia, M.A., Siddiqi, A.R., Murtaza, G., Recent Developments in Sweat Analysis and Its Applications. Int. J. Anal. Chem. 2015, 2015, 1–7.

218. Zhang, J., Tang, Y., Song, C., Xia, Z., Li, H., Wang, H., Zhang, J., 2008. PEM fuel cell relative humidity (RH) and its effect on performance at high temperatures. Electrochim. Acta 53, 5315–5321.

219. Lee, P.H., Hwang, S.S., 2009. Performance Characteristics of a PEM Fuel Cell with Parallel Flow Channels at Different Cathode Relative Humidity Levels. Sensors (Basel). 9, 9104–21. doi:10.3390/s91109104

220. Mochalski, P., King, J., Unterkofler, K., Hinterhuber, H., Amann, A., 2014. Emission rates of selected volatile organic compounds from skin of healthy volunteers. J. Chromatogr. B 959, 62–70.

221. Acevedo, C. A.; Sánchez, E. Y.; Reyes, J. G.; Young, M. E. Volatile Organic Compounds Produced by Human Skin Cells. Biol. Res. 2007, 40, 347–355.

222. Antolini, E., 2007. Catalysts for direct ethanol fuel cells. J. Power Sources 170, 1–12.

223. Junming, H.; Liangfei, X.; Jianqiu, L.; Ouyang, M.; Siliang, C.; Fang Chuan, F., Water management in a self-humidifying PEM fuel cell system by exhaust gas recirculation, in: 2014 IEEE Conference and Expo Transportation Electrification Asia-Pacific (ITEC Asia-Pacific). IEEE, pp. 1–6. 2014.

224. Mihajlovic, Z.; Milosavljevic, V.; Rajs, V.; Milivojcevic, F.; Zivanov, M.; Miniature low cost electrochemical sensor module for measurement of gas concentration, in: 2014 22nd Telecommunications Forum Telfor (TELFOR). IEEE, pp. 702–705, 2014.

225. Hruska, L. W. Smart batteries and lithium ion voltage profiles, in: The Twelfth Annual Battery Conference on Applications and Advances. IEEE, pp. 205–210, 1997.

226. Kim, S. S.; Young, C.; Vidakovic, B. Gabram-Mendola, S. G. A.; Bayer, C. W.; Mizaikoff, B. Potential and Challenges for Mid-Infrared Sensors in Breath Diagnostics. IEEE Sens. J., 2010, 10 (1), 145–158.

227. Kose, M. E.; Omar, A.; Virgin, C. A.; Carroll B. F.; Schanze, K. S. Principal Component Analysis Calibration Method for Dual-Luminophore Oxygen and Temperature Sensor Films: Application to Luminescence Imaging, Langmuir, 2005, 21, 9110−9120.

228. Delpha, C.; Lumbreras M.; Siadat, M. An intelligent gas sensor application for the discrimination of forane 134a and carbon dioxide gas concentrations: the effect of relative humidity. In ETFA 2001 8th International Conference on Emerging Technologies and Factory Automation. Proceedings, Antibes-Juan les Pins, France, 393-399, 2001.

229. K. M. Dubowski. Breath-alcohol simulators: scientific basis and actual performance. J. of analytical toxicology. 1979, 3, 177-182.

230. Honemann, W.; Washington, J.; Honemann, M. C.; Nietgen G. W.; Durieux, M. E. Partition Coefficients of Volatile Anesthetics in Aqueous Electrolyte Solutions at Various Temperatures. Anesthesiology, 1998, 89, 1032-1035.

231. William, R. H.; Leikin, J. B. Medicolegal issues and specimen collection for ethanol testing. Laboratory medicine. 1999, 30 (8), 531-537.

232. Modell, J. G.; Taylor, J. P.; Lee, J. Y. Breath alcohol values following mouthwash use. JAMA. 1993, 270, 2955–2956.

233. Labianca, D. A. The chemical basis of the Breathalyzer: A critical analysis. J. Chem. Educ. 1990, 67, 259–261.

234. Anderson, J. C.; Hlastala, M. P. The kinetics of transdermal ethanol exchange. J. Appl. Physiol. 2006, 100, pp. 649–655.

235. Lockhart, S. H.; Yasuda, N.; Peterson, N.; Laster, M.; Taheri, S.; Weiskopf, R. B.; Eger, E. I. Comparison of percutaneous losses of sevoflurane and isoflurane in humans. Anesthesia & Analgesia. 1991, 72 (2),212–215.

236. Lu, C.-C.; Tsai, C.-S.; Hu, O. Y.-P.; Chen, R.-M.; Chen, T.-L.; Ho, S. T. Pharmacokinetics of isoflurane in human blood, Pharmacology. 2008, 81, 344–349.

237. Alam, F.; RoyChoudhury, S.; Jalal, A. H.; Umasankar, Y.; Forouzanfar, S.; Akter, N.; Bhansali, S.; Pala, N. Lactate biosensing: the emerging point-of-care and personal health monitoring, Biosensors and Bioelectronics, 2018, 117, 818-829.

238. Jalal, A. H.; Roy, S.; Ahad, M. A. Comparative analysis of the performance of polymer based opto-chemical sensor in detecting ammonia in diverse mediums, 2013 Proceedings of IEEE Southeastcon, Jacksonville, FL, 2013, pp. 1-4.

239. Jalal, A. H.; Roy, S.; Ahad, M. A. Evanescent-based clad-modified polymer optical fiber sensor for ammonia gas detection, International conference on engineering research, innovation and education, Sylhet, Bangladesh, , 2013, pp. 536 – 541.

240. Jalal, A. H. Reversible evanescent-based opto-chemical sensor for in-situ detection of contaminants in static and dynamic fluid system, Thesis, Purdue University, 2010, 1 – 96.

241. Siddiquee, M. R.; Marquez, J. S.; Atri, R.; Ramon, R.; Mayrand, R. P.; Bai, O. Movement artefact removal from NIRS signal using multi-channel IMU data, BioMedical Engineering OnLine, 2018, 17(1), pp.120.

VITA

AHMED HASNAIN JALAL

Doctor of Philosophy (2014 – 2018)
Department : Electrical and Computer Engineering (ECE)
University : Florida International University (FIU), Miami, FL

M.S. in Engineering (2008 – 2010)
Department : Electrical and Computer Engineering (ECE)
University : Purdue University Northwest, Hammond, IN

B.S. in Engineering (2001 – 2007)
Department : Electrical and Electronic Engineering (EEE)
University : Chittagong University of Engineering and Technology (CUET)

PUBLICATIONS

1. Fahmida Alam, Sohini RoyChoudhury, Ahmed Hasnain Jalal, Yogeswaran Umasankar, Shahrzad Forouzanfar, Naznin Akter, Shekhar Bhansali, Nezih Pala. Lactate biosensing: the emerging point-of-care and personal health monitoring, Biosensors and Bioelectronics, vol. 117, pp. 818-829, October 15, 2018.
2. Ahmed Hasnain Jalal, Fahmida Alam, Sohini RoyChoudhury, Yogeswaran Umasankar, Nezih Pala, Shekhar Bhansali. Prospects and challenges of volatile organic compound sensors in human healthcare, ACS Sensors, Vol. 3 (7), pp. 1246-1263, June 8, 2018.
3. Ahmed Hasnain Jalal, Yogeswaran Umasankar, Fraker Christopher, Ernesto A. Pretto, Shekhar Bhansali. A model for safe transport of critical patients in unmanned drones with a 'watch' style continuous anesthesia sensor, J. of Electrochemical Society (Focus Issue on Ubiquitous Sensors and Systems for IoT), vol. 165, Issue 8, pp. B3071 – B3077, April 6, 2018.
4. Ahmed Hasnain Jalal, Yogeswaran Umasankar, Pablo J. Gonzalez, Alejandro Alfonso, Shekhar Bhansali. Multimodal technique to eliminate humidity interference for specific detection of ethanol, Biosensors and Bioelectronics, vol. 87, pp. 595-608, January 15, 2017.
5. Sohini RoyChoudhury, Vaishali Rawat, Ahmed Hasnain Jalal, Sangeeta N. Kale, Shekhar Bhansali. Recent advances in metamaterial split-ring-resonator circuits as biosensors and therapeutic agents, Biosensors and Bioelectronics, vol. 86, pp. 522–530, December 15, 2016.
6. Syed Khalid Pasha, Ahmed Hasnain Jalal, Aparajita Singh, Shekhar Bhansali. “Chapter 1: Nanobiotechnology: An Abrupt Merger”, Nanobiotechnology for Sensing Applications: From Lab to Field, Apple Academic Press - CRC Press, ISBN 978-1-77-188328-3, pp. 1-42, August 23, 2016.
7. A. G. Agwu Nnanna, Ahmed Hasnain Jalal. Patent No. US 8,735,165 B2. Oxazine-based sensor for contaminants detection, fabrication method therefor, and uses thereof. May 27, 2014.

8. Ahmed Hasnain Jalal, Jinsong Yu, A. G. Agwu Nnanna. Fabrication and calibration of oxazine-based optic fiber sensor for detection of ammonia in water, J. of Applied Optics, Vol. 51, Issue 17, pp. 3768 – 3775, June 10, 2012. (I.F.: 1.65)
9. Ahmed Hasnain Jalal, Fahmida Alam, Ashfaq Ahmed, Mohammad A. Ahad. Precise calibration of optical fiber sensor for ammonia sensing using multivariate analysis, SPIE Defense + Commercial Sensing, vol. 10654, 106540W-1 – 106540W-7, 2018.
10. Fahmida Alam, Ahmed Hasnain Jalal, Raju Sinha, Yogeswaran Umasankar, Shekhar Bhansali, Nezih Pala. ZnO nanoflakes-based mediator free flexible biosensors for the selective detection of ethyl glucuronide (EtG) and lactate, SPIE Defense + Commercial Sensing, vol. 10639, pp. 106392O-1 – 106392O-6, 2018.
11. Fahmida Alam, Ahmed Hasnain Jalal, Raju Sinha, Yogeswaran Umasankar, Shekhar Bhansali, Nezih Pala. Sonochemically synthesized ZnO nanostructure-based L-lactate enzymatic sensors on flexible substrates, MRS Advances, vol. 3 (5), pp. 277-282, 2018.
12. Ahmed Hasnain Jalal, Yogeswaran Umasankar, Mustahsin Chowdhury, Shekhar Bhansali. A fuel cell sensing platform for selective detection of acetone in hyperglycemic patients, ECS Transactions, vol. 80 (10), pp. 1369 – 1378, 2017.
13. Fahmida Alam, Raju Sinha, Ahmed Hasnain Jalal, Pandiaraj Manickam, Phani Kiran Vabbina, Shekhar Bhansali, Nezih Pala. Sonochemically synthesized zinc oxide nanoflakes based electrochemical immunosensor for ethyl glucuronide (EtG) detection, ECS Transactions, vol. 80 (10), pp. 1287-1294, 2017.
14. Ahmed Hasnain Jalal, Yogeswaran Umasankar, Shekhar Bhansali. Development and characterization of fuel cell sensor for potential transdermal ethanol sensing, ECS Transections, vol. 72 (31), pp. 25-31, 2016.
15. Yogeswaran Umasankar, Ahmed Hasnain Jalal, Pablo J. Gonzalez, Mustahsin Chowdhury, Alejandro Alfonso, Shekhar Bhansali. Wearable alcohol monitoring device with auto-calibration ability for high chemical specificity, IEEE 13th International conference on wearable and implantable body sensor networks (BSN), San Francisco, California, June 14 – 17, 2016.
16. Ahmed Hasnain Jalal, Sajib Roy, Fahmida Alam. Thermal cycling layer by layer dip coating method for oxazine formation on clad modified optical fiber core, IEEE International conference on advances in electrical engineering, Vellore, India, January 9-11, 2014.
17. Ahmed Hasnain Jalal, Sajib Roy, Mohammad A. Ahad. Comparative analysis of the performance of polymer based opto-chemical sensor in detecting ammonia in diverse mediums, IEEE Southeast conference, Jacksonville, Florida, April 4-7, 2013.
18. Ahmed Hasnain Jalal, Sajib Roy, Mohammad A. Ahad. Evanescent-based clad-modified polymer optical fiber sensor for ammonia gas detection, International conference on engineering research, innovation and education, Sylhet, Bangladesh, January 11-13, 2013.